Investigation of fretting behaviour in pressure armour layers of flexible pipes.

DON RASIKA PERERA, Solangarachchige.

REFERENCE

Investigation of Fretting Behaviour in Pressure Armour Layers of Flexible Pipes

Solangarachchige Don Rasika Perera

A thesis submitted in partial fulfilment of the requirements of

Sheffield Hallam University

for the Degree of Doctor of Philosophy

Faculty of Arts Computing and Engineering Studies

Materials and Engineering Institute

October 2007

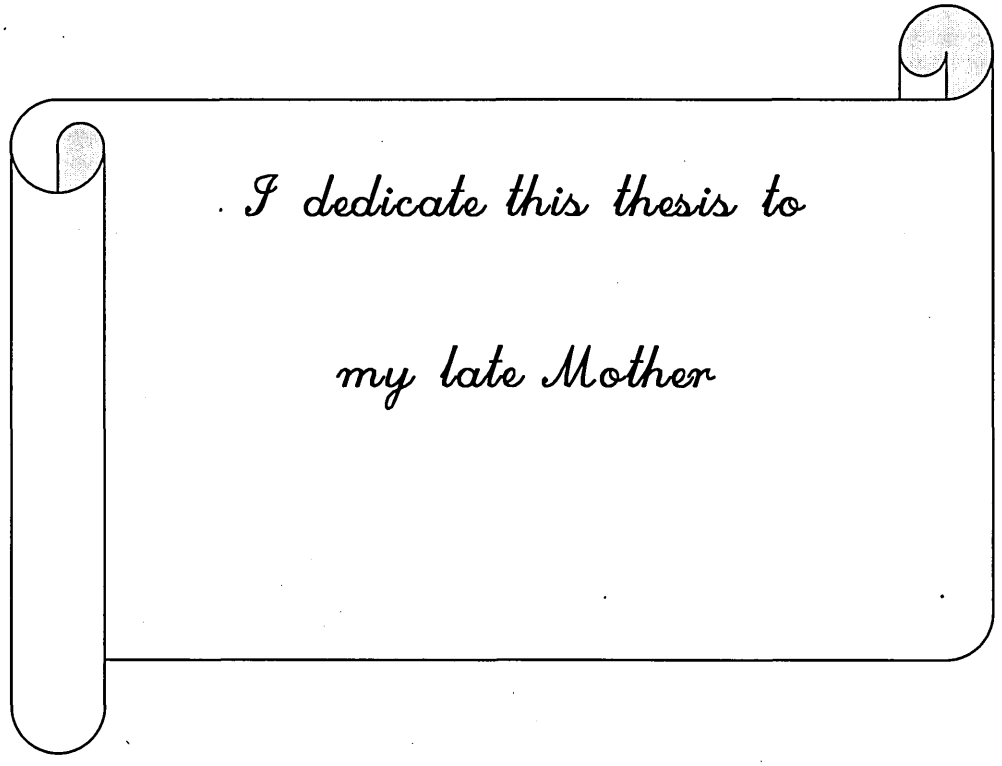
I dedicate this thesis to
my late Mother

Preface

I declare that this thesis is based on the findings of research carried out in the Materials and Research Institute of the Sheffield Hallam University.

The content of the thesis is original except where specific references are made to other work

No part of this thesis has been submitted to any other University.

S D Rasika Perera

Acknowledgements

First I would like to thank my Director of studies, Dr Upul Fernando for his guidance and help. I would also like to thank my second supervisor Professor Robert Akid.

I would like to thank my advisors Dr Terry Sheldrek and Mr. Richard Clements for providing me with vital information and guidance.

I would also like to thank Mr. Tim O Hara, Mr. John Bickers, Mr. Brian Didsbury, Mr. Roger Tingle, Mr. John Bradshaw, Mr. Stephen Magowan and Mr. Malcolm Jackson for their assistance with laboratory apparatus and manufacture of machine components for my experimental setup.

I would also like to thank the Sheffield Hallam University and the Wellstream International for their support.

I would like to thank my dearest Wife, Thushara for standing beside me like a shadow all the time.

Finally, I would like to thank the Asian Development Bank funded "Distance Education Modernization Project" of the Open University of Sri Lanka for funding this project.

Table of contents

List of figures

CHAPTER 3

CHAPTER 4

Abstract.

The incidence of fretting damage in the pressure armour wires of flexible pipes used in offshore oil explorations has been investigated. A novel experimental facility which is capable of simulating nub and valley contact conditions of interlocking wire winding with dynamic slip, representative of actual pipe loading, has been developed. The test set-up is equipped with a state of the art data acquisition system and a controller with transducers to measure and control the normal load, slip amplitude and friction force at the contact, in addition to the hoop stress in the wire. Tests were performed with selected loading and the fretted regions were examined using optical microscopy techniques.

Results show that the magnitude of contact loading and the slip amplitude have a distinct influence on surface damage. Surface cracks originated from a fretting scar were observed at high contact loads in mixed slip sliding while surface damage predominantly due to wear was observed under gross slip. The position of surface cracks and the wear profile have been related to the contact pressure distribution. The evolution of friction force and surface damage under different slip and normal pressure conditions has been analysed.

A fracture mechanics based numerical procedure has been developed to analyse the fretting damage behaviour. A severity parameter is proposed in order to ascertain whether the crack growth is in mode I or mode II cracking. The analysis show the influence of mode II cracking in the early stages of crack growth following which the crack deviates in the mode I direction making mode I the dominant crack propagation mechanism. The crack path determined by the numerical procedure correlates well with the experimental results.

A numerical analysis was carried out for the fretting fatigue condition where a cyclic bulk stress superimposes with the friction force. The analysis correlates well with short crack growth behaviour. The analysis confirms that fretting is a significant factor that should be taken into account in design and operation of the pressure armour wires of flexible pipes at high contact pressure if the bulk cyclic load superimposes with the friction force. As predicted by the numerical procedure and further by experimental investigations, the surface cracks initiating on the wire in this condition are self arresting after propagating into a certain depth.

CHAPTER 1: INTRODUCTION

1.1 Introduction

Fretting is a process of material damage, which results from microscopically small-amplitude oscillatory movements (slip) between contacting components. *Fretting fatigue* is a phenomenon where a component is subjected to fretting damage in conjunction with a bulk cyclic stress mainly in the mixed slip sliding (the mixed slip condition is explained in Chapter 2) condition. This normally leads to reduced fatigue life of the component. Under fretting, shallow cracks are originated on the surface of mating components and these cracks may propagate due to cyclic bulk stress. Fretting can severely reduce the fatigue strength of a component.

Key parameters affecting fretting fatigue are known to be normal load, slip amplitude, contact geometry, surface roughness and number of cycles, bulk cyclic stress and material properties. However, their contribution and how they influence the fretting fatigue process is still the subject of intensive research [1-6].

Fretting usually results in two forms of damage: surface wear in the gross slip condition (this condition is explained in Chapter 2) and surface cracks under the mixed slip condition, resulting in accelerated deterioration of fatigue life of a mechanical component. Fretting fatigue remains an important factor contributing to premature failure of load-bearing components stress level below the fatigue limit.

Referring to data published from the "United States Air Force", Ciavarella et al [4] states that "Fretting fatigue is responsible for one out of six in-service mishaps in gas turbine engines".

Therefore, accounting for the effect of fretting damage is more important in designing of mechanical components that are in contact and subjected to small oscillatory movements.

1.2 Fretting damage in flexible pipes

The work presented in this thesis is on the fretting damage behaviour of un-bonded flexible pipes. Un-bonded flexible pipes are widely used in the off-shore oil industry to transport gas and oil from the sea bed to floating storage and production facilities. These pipes are manufactured as a composite structure comprising of several metallic and polymer layers, as shown in Figure 1.

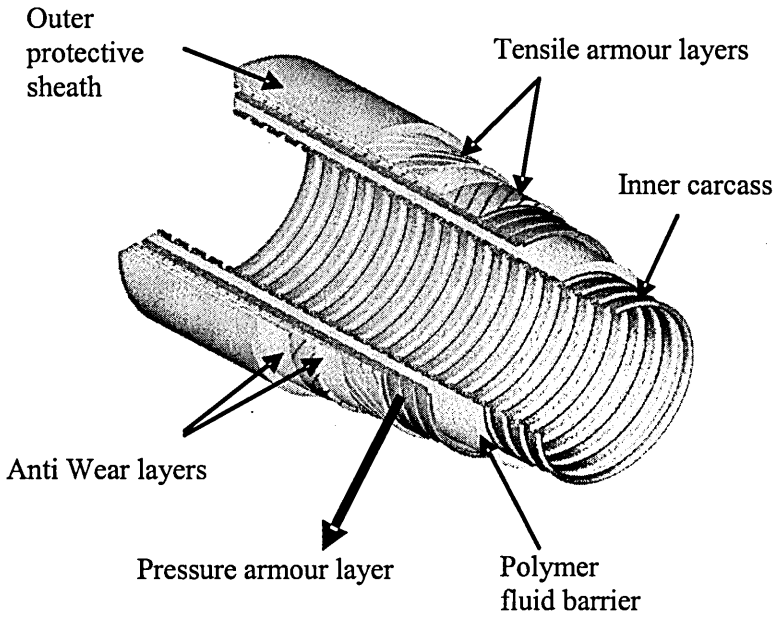

Figure 1.1 - Sectional view of the flexible pipe structure

The pipe structure comprises a composite of layered materials that form a pressure containing conduit. Each layer has a specific role, preventing either collapse, burst, or leak while allowing some degree of freedom between one another. Two types of metallic layers, pressure armour layers and tensile armour layers (Figure 1.1) are specifically designed to provide the hoop and axial strength of the pipe, respectively. The pressure armour layer is made up of profiled steel wires wound in helical shape as depicted in the Figure 1.2.

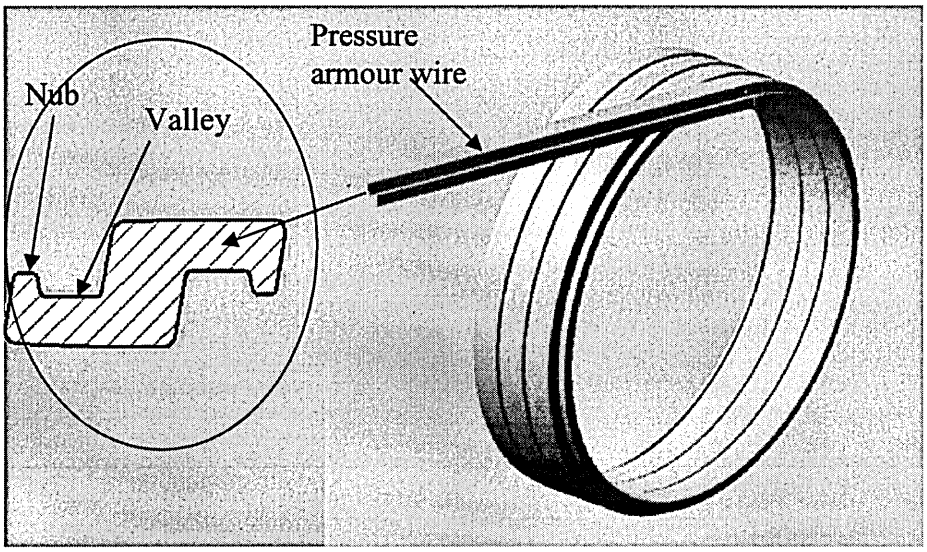

Figure 1.2 – The pressure armour layer made up of profiled wires.

The profile of the pressure armour wire is such that it interlocks in a nub and a valley contact (the nub and valley contact is illustrated in Figure 3.2). This nub and valley contact provides limited freedom for the pressure armour layer to move along with other layers when the pipe is flexing under service conditions.

During service, the pipe structure is subjected to pressure from the external sea water and the internal pumping fluid. The pressure difference between the outer sea water and the internal pumping fluid in conjunction with the interaction of other metallic and polymer layers creates a contact pressure on the nub and valley contact of the pressure armour layer. This difference of pressure also creates a hoop stress in the pressure armour layer. The movement of the pipe due to sea waves, displacements of the floating production facility and other dynamic forces create small oscillatory movements between contact points, creating ideal conditions for fretting damage to occur. This condition may reduce the fatigue life of the pressure armour wire and it is therefore necessary to study and estimate the extent of fretting damage that might occur on the pressure armour wires of flexible pipes.

1.3 Aims and objectives of the research.

As the offshore exploration and production is developing in deeper fields, flexible risers have become a very important component in floating offshore production facilities. Consequently, the number of flexible risers in operation has tremendously increased in recent years. Predicting their fatigue life is very complex, especially when considering the possible interactions of additional degradation mechanisms such as fretting.

Whilst the presence of fretting cracks itself may be detrimental to the fatigue strength of the pressure armour wires, their influence on fatigue durability of the wires can be a potential risk.

An understanding of the effects of loading and design parameters that control fretting damage in pressure armour wires is thus considered to be highly desirable in order to optimize pipe design and eliminate the risk of premature fatigue failure.

This study involved a comprehensive systematic investigation of the relative effects of local and global mechanistic parameters that determine fretting fatigue life of the pressure armour wires in flexible pipes. The aims and objectives of this research are as follows.

1. Develop a new testing facility to investigate the fretting damage behaviour in pressure armour wires of flexible pipes.
2. Perform experimental investigations to identify the influence of contact pressure, slip amplitude, bulk stress, wire profile, on the growth of fretting damage in pressure armour.
3. Investigate the damage process, crack growth and the damage rate of fretting fatigue.
4. Develop a predictive method to determine the fretting damage process and the rate and type of damage evolution.

This thesis comprises eight chapters. In the second chapter, a comprehensive literature review is presented. The literature review covers basic definitions and the current understanding of fretting damage reported in the literature. The parameters affecting fretting damage and their individual contributions, the experimental techniques in fretting damage analysis and numerical predictive methods used for fretting damage, are reviewed.

One of the main objectives of the project was to design and build a new experimental facility to investigate the fretting damage behaviour of the pressure armour wires of flexible pipes. The experimental facility has been designed and developed including a digital controller which was used to control the experiments and to log data. The design and development of the experimental set-up are described in the Chapter 3.

The experimental investigation which has been performed using the new facility, consisted of three series of experiments and in total of 33 tests have been performed and the details of these tests are given in Chapter 4. The first series of experiments (preliminary experiments) were carried out in order to gain an understanding of how the contact pressure, the slip amplitude and the friction force interact and how these parameters would affect the fretting damage process. The second series, "interrupted tests" were performed in order to establish the boundaries between damage and non-damage. Further cyclic tests were carried out on pre-fretted specimens, to estimate the reduction in fatigue strength due to fretting damage of pressure armour wires.

A fracture mechanics based fretting damage analysis procedure has been developed and is described in Chapter 5. The methodology is capable of predicting the crack path and the crack propagation rate and the size of non propagating cracks resulted from fretting. The experimental results and observations have been discussed and compared with the numerical predictions in Chapter 6. Conclusions derived from this study and future work proposed to further the knowledge of the subject are given in Chapter 7 and 8 respectively.

CHAPTER 2: LITERATURE REVIEW

The first specific citation of fretting damage according to the literature is by Eden et al. in 1911 [7]. They found that brown oxide debris was formed in the grips of their fatigue machine, when in contact with a steel specimen. In 1927 Tomlinson [8] designed two testing machines to create small oscillatory amplitude motion and conducted the first controlled investigations on fretting damage. He used the term 'Fretting Corrosion' to explain the damage process, since he saw red iron oxide debris during the process. Further, he established that small oscillatory movements were necessary for the damage to occur (which he termed as slip) and he observed that the damage was caused by movements with amplitudes as small as few micrometres.

2.1 Examples of Fretting Damage.

Fretting damage can be observed in almost all mechanical contacts involving two parts that are "nominally" fixed or held together. These include components such as interference fits, flexible couplings, roller bearings, riveted joints, pipe lines and turbine dovetail joints. The first clue to suspect that fretting damage is happening between two or more machine components is appearance of loose debris from the contact. On steel contacts, the debris is more red coloured than ordinary rust; for aluminium contacts, the debris is black where as the aluminium oxide is white in colour **[9].** Due to this reason, early researchers [10] have used terms such as "friction oxidation, wear oxidation, bleeding, cocoa etc." to describe the surface damage due to fretting in metals.

Such damage is common in interference fits of railway wheels where the wheel is press-fitted onto a steel axle **[9-13]**. The shaft is subjected to bending, when it is loaded. The rotation of the wheel and axle causes cyclic loading in the contact area of the wheel and the shaft causing fretting damage.

Assemblies of plates held together by rivets and bolts, such as aircraft fuselages are susceptible to fretting damage when subjected to vibrations or cyclic loading [9,14,15]. In a simple riveted or bolted joint there are three possible points where the fretting damage can occur. (a) between the riveted panels, (b) between the under side of rivet head and the joint panel (c) Between the shank of rivet and the rivet hole of the joint.

Flexible couplings are another mechanical component where the fretting damage can occur. Couplings are used to connect two rotating shafts in machines. Generally, there are two design types of couplings; rigid and flexible couplings. In both designs, slight misalignments may lead to small oscillatory movements between two joining components [1, 9, 10 ,16, 17]. Under operational conditions, when two shafts are rotating, cyclic loads are imposed on the coupling. This may cause fretting damage with small oscillatory movements.

Steel ropes which are made of many small diameter wires wound together, are widely used for cable cars, cranes, mooring of ships and electric conductors (cables). When the rope is under tension, a high contact pressure is imposing between individual steel wires in contact. Under operational conditions when the wire is

flexed small oscillatory movements occur between these individual wires creating most favourable conditions for fretting damage **[1, 7, 17]**.

Severe fretting damage can occur in ball or roller bearings that are subjected to vibration. This condition is predominant if the bearings are stationary for long period of time and are seldom used in rotary movements. In this case, damage occurs at the points of contact between the bearing and the races **[7, 18]**. This type of damage can happen in roller bearings of gun mountings in tanks and ships and was a serious problem at one time in automobile bearings when, new vehicles were transported by rail **[9]**.

In turbine rotors, the turbine blade is fixed by means of a dovetail joint. When in operation, due to centrifugal forces, the dovetail fixing of the blade to the disc is subjected to high contact pressure and variations of temperature and rotating speeds may create small slip movements within the contact creating fretting damage **[4, 22, 23]**.

2.2 Main parameters affecting fretting damage.

The main parameters affecting fretting damage are known to be the contact pressure, slip amplitude, frequency, local bulk stress and friction force. In addition to these, there can be many more parameters that have been observed to influence the fretting damage process **[62]**.

2.2.1 Slip regimes in fretting.

The slip is the relative displacement between two contacting points on two bodies (specimen and the pad). In real engineering components the relative displacement can vary from a few micrometres to a few metres. However, fretting is prominent when the relative slip is small, approximately 0.1 μm to about 300 μm[25] . There can be (a) stick, (b) mixed slip (stick-slip) and (c) gross slip zones of sliding in fretting fatigue [**27**].

In the stick zone, there is no movement between the fretting specimen and the pad, it occurs at very small amplitudes **[2, 27, 29]**. There is observed to be very little fretting wear and there is negligible fretting crack growth in this regime **[2, 27, 29]**.

In the gross slip regime, the whole contacting area of the fretting pad moves relative to the specimen. In this condition, severe surface wear may occur **[2, 27, 30]** . For a contact pair (specimen and a pad), at constant normal load, for a given system in the stick condition, if the displacement amplitude is increased, a transition from stick to gross slip through mixed slip will occur.

In the mixed slip regime despite the increase of global displacement, the region with high contact pressure will remain in a stick condition while the regions with low local pressure distribution start sliding. In this regime, the wear rate is moderate compared to the stick regime **[2, 24, 27,29]**.

These three regimes can be identified from the shape of friction loops, when the slip amplitude is plotted against the friction force **[2]**. The typical shape of friction loops for the above three regimes is graphically illustrated in Figure .2.1.

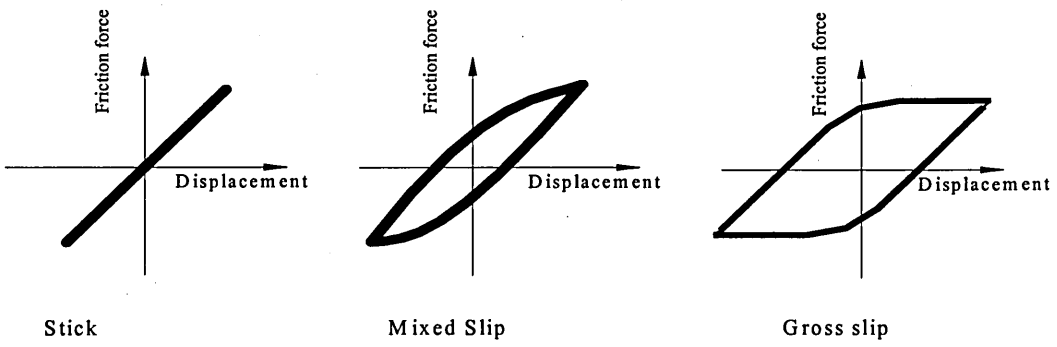

Figure 2.1 Transition from stick, stick-slip to gross slip

The Figure 2.1 clearly shows that the friction force varies between a maximum positive and a minimum negative value through zero with slip amplitude during a cycle and the friction force within a cycle is not fixed. A constant value for friction coefficient (the ratio of normal force to the traction force) cannot be obtained for fretting conditions. The coefficient of friction, (μ) in the traditional sense, can only be defined for the case of gross slip where the friction force is constant throughout the sliding process. However, to describe the variation of frictional force with different slip conditions, the ratio of global friction range, ΔF_{max}, to twice the applied normal load 2N has been used in the literature [3]. Hence to avoid ambiguity between Coulomb friction coefficients and friction under fretting conditions, the term '*traction coefficient*' is used in this thesis as the ratio of the global friction range, ΔF_{max}, and twice of the applied normal load 2N.

2.2.1.1 Quantification of sliding condition.

As discussed above, the sliding condition is classically distinguished from the friction loop shape. Fouvry et al [30] introduced the ratio (Eqation 2.1) between the dissipated energy (area of the hysterisis loop) and the equivalent total energy as shown in Figure 2.2.

$$A = \frac{E_d}{E_t} = \frac{E_d}{4Q_*\delta_*} \qquad \text{-(2.1)}$$

Where,

δ_* -Displacement amplitude

Q_* - Tangential force amplitude

E_d - Dissipated energy (Area of the friction loop)

E_t - Total energy given by $E_t = 4Q_*\delta_*$

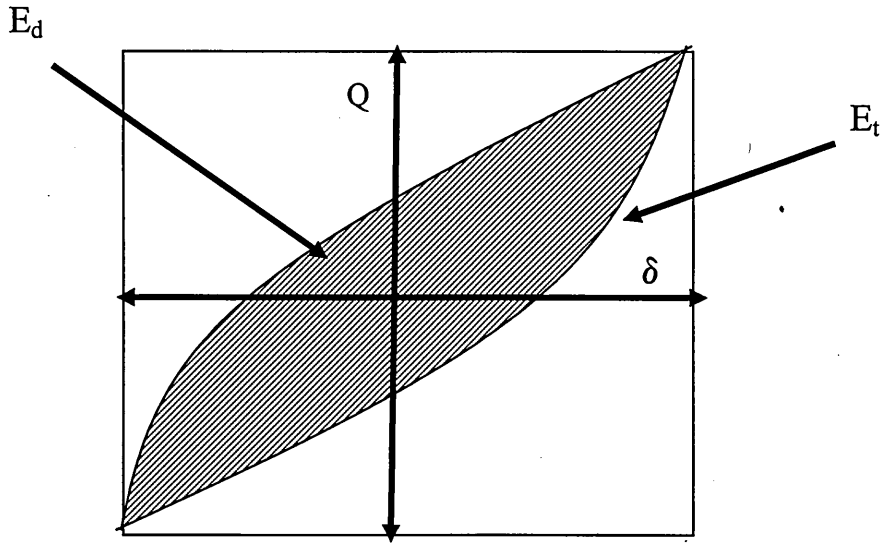

Figure 2.2. Sliding regime quantification parameters [30]

It has been demonstrated that for an elastic sphere on flat contact configuration that this variable reaches a constant value (A_t=0.2) at the sliding transition. When $A< A_t$ the sliding condition is mixed-slip and when $A>A_t$ the sliding condition is gross slip [30].

2.2.1 Effect of slip amplitude

Vingsbo and Soderberg **[31]** illustrated the effect of slip amplitude in terms of stick, mixed sip and gross slip regimes on the wear process and fatigue life as shown in Figure 2.3.

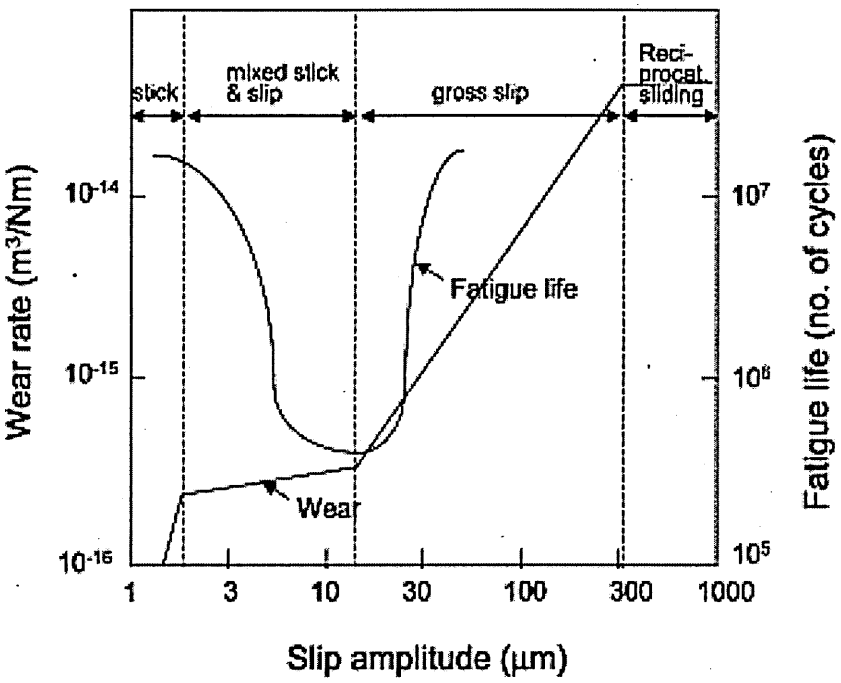

Figure 2.3 –The effect of slip amplitude on wear and fretting fatigue life [29]

According to the Figure 2.3 the wear rate increases with increase of slip amplitude. The wear rate is minimum in the stick region. It reaches a constant value in mixed slip region and increases gradually with increase of slip and reaches a maximum in the gross slip region or reciprocating sliding.

On the other hand, the minimum fatigue life is observed in the mixed slip boundary and higher values are observed in the stick and gross slip regions.

Ding et al [17] carried out a finite element based analysis for slip regime on fretting wear and stress evolution. In their study they predicted that the gross slip condition is more wear dominant and the partial slip condition is more detrimental with regard to the fretting stress evolution.

2.2.2 Variation of Friction force during fretting damage.

During experimental investigations, a large variation of friction force can be observed in first few thousand cycles [3, 21, 32]. Starting from a low value, the friction force stabilises at a certain level after a few thousand cycles. The maximum raction coefficient under fretting conditions can go up to about 1.5 for steel-on-steel contacts, which is considerably higher than the conventional pure sliding coefficient of friction at large slip amplitudes [3]. If the slip condition changes from stick-slip to gross slip during the experiment, a significant increase of friction force can be observed for steel [29,30].

2.2.3 Effect of normal load

The normal load between the contacting surfaces is essential for fretting to happen. For an experiment carried out with steel contacts on aluminium alloy, a sharp decrease in fretting fatigue life when the contact pressure is increased from zero to 30 MPa was reported by Waterhouse [9] and beyond 30 MPa the increase of the contact pressure had very little effect on the fretting fatigue life.

Nakazawa et al **[33]** reported a reduction in fretting fatigue life and increase of fretting wear with the increase of contact pressure for austenitic stainless steel.

Under fretting conditions, Ramesh and Gnanamoorthy **[32]** reported a reduction of the friction force with increasing normal loads for bearing steel, EN31, and structural steel, EN24.

Fernando et al **[21]** have observed a reduction of fretting fatigue life with an increase of contact pressure up to about 80 MPa and an increase of the fretting fatigue life when the contact pressure was increased beyond 80 MPa. Further, they have observed that this behaviour is predominant at low axial stress amplitudes. Fernando et al have attributed this variation to the crack closure due to high compressive normal load.

Naidu and Raman **[34]** reported an increase of the traction coefficient with an increase of the contact pressure. The reduction of fretting fatigue strength due to contact pressure was variable. They have observed **[34]** that when the contact pressure increased from 100 MPa to 150 MPa, the fretting fatigue life was increased. Minimum fretting fatigue life was observed at 100 MPa contact pressure and the fretting fatigue life was decreased as the contact pressure was increased up to 100 MPa. They have also attributed this effect to the crack closure at high contact pressure.

Iyre and Mall **[35]** derived a direct relationship between the contact pressure and decrease of fretting fatigue life. They observed in their numerical analysis that the local stress range increases with an increase of normal contact pressure.

2.2.4 Atmospheric pressure and oxygen concentration

Some researchers **[37- 40]** have reported that the coefficient of traction is high in vacuum. The value gradually drops with increase of pressure until atmospheric pressure and remains constant when the pressure is further increased. Iwabuchi **[40]** has reported that although the coefficient of traction was reduced with increase of temperature, the coefficient of traction did not significantly change with temperature in vacuum, at pressures below 10 Pa. Iwabuchi **[40]** also reported a low wear rate in vacuum, compared to the wear rate at atmospheric pressure.

2.2.5 - Effect of temperature

Researchers **[2, 39]** have reported that a glaze oxide is formed for nickel and ferrous based alloys resulting in reduction of coefficient of friction at high temperatures. On the effect of temperature on fretting wear, Kazuhisha et al **[20]** reported a lower rate of wear for Ti-48Al-2Cr-2Nb material, at 473K as compared to that at room temperature. The drop in wear rate was related to the increased rate of oxidation. However, the wear rate was increased with increasing temperature from 473K to 823K. This behaviour was explained by oxide film disruption with crack generation, debris and pitting of the wear surface. Crack generation at high temperature (above 473K) was attributed **[20]** to the reduction in yield strength of the material at high temperatures.

2.2.6 Effect of lubricants

Lubrication is considered to be an important method of reducing fretting damage. The objective of the lubrication is to reduce the traction coefficient and thus reduce the fretting damage. McColl et al **[41]** reported a delay of fretting wear when the interface is lubricated with grease, in eutectoid steel ropes. A low coefficient of traction (below 0.2) was observed in the early stages of fretting wear, (up to 1000 cycles), and was gradually increased to about 0.8-1.0 at 100000 cycles. When the same test was carried out with oil bath lubrication, a significant reduction in traction coefficient (0.2) was reported throughout the experiment **[41]**.

Shima et al **[42]** have reported with oil lubrication, the coefficient of traction increased at low strokes of slip amplitude (below 5 μm) but a decrease of traction coefficient was observed at high slip amplitudes.

Zhou and Vincent **[44]** in a review have noted that solid lubricants are effective in the partial slip condition while grease and oil are more suitable in the gross slip condition. Further, they have noted that the understanding on the effect of lubricants on fretting is still limited and further investigations are needed to understand the mechanisms.

2.3 Contact mechanics and fretting damage predictive methods.

Fretting damage can be characterised as a crack initiation process in the early stage of fretting fatigue and subsequently these cracks propagate under dynamic loading. For safe design of mechanical components against fretting fatigue failure, it is necessary to estimate crack initiation and propagation life in relation to bulk and local loading conditions.

The majority of work on fretting damage was carried out with idealised contact geometries based on Hertzian contacts. These geometries are sphere on flat contact or cylinder on flat. Generation of analytical descriptions to obtain the pressure and subsurface stress distributions for this type of contact is well established. In addition to the simplicity in numerical analysis for this type of contact, the alignments are less critical compared to contacts involving flat with straight edges or flats rounded edges.

Hertzian contacts

The subject of contact mechanics was introduced in 1882 by Heinrich Hertz with his classic paper 'On the contact of elastic solids' (according to Johnson **[45]**). This was the first satisfactory analysis of the stresses at the contact of two elastic solids. Hertz theory was obtained for two parallel infinitely long cylinders or spheres in contact and is restricted to frictionless surfaces and perfectly elastic solids. A typical Hertzian contact is shown in Figure 2.4.

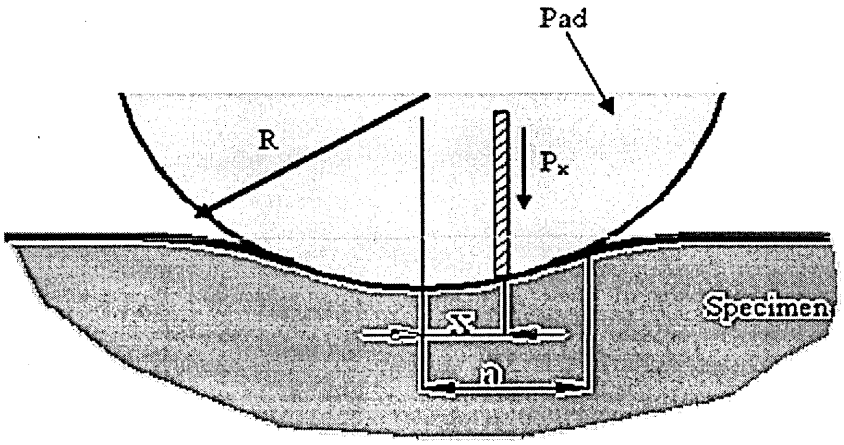

Figure.2.4 – Typical Hertzian contact

According to the Hertz theory, the pressure distribution of an elemental area at a distance **x** from the centre of contact is given by **[45]**,

$$p(x) = p_0\sqrt{1-\left(\frac{x}{a}\right)^2} \qquad \text{-(2.2)}$$

Where,

p_0 - is the maximum Hertzian contact pressure

a – is the contact half width

x- any point along the contact at x distance from the centre line.

The contact half width is given by **[45]**,

$$a = \sqrt{\left(\frac{4PR}{\pi E}\right)} \qquad \text{-(2.3)}$$

The maximum Hertzian contact pressure is given by **[45]**,

$$p_0 = \sqrt{\left(\frac{PE}{\pi R}\right)} \qquad \text{-(2.4)}$$

Where,

R – Radius of the contact

E – Young's modulus

P = Load per unit length [MN/mm]

Note that if the mating materials are different, the E is defined differently taking into account the Young's modulus of both mating materials and the reader is referred to reference **[45]** for further details.

The pressure distribution given by equation 2.2 is elliptical as shown in Figure 2.5.

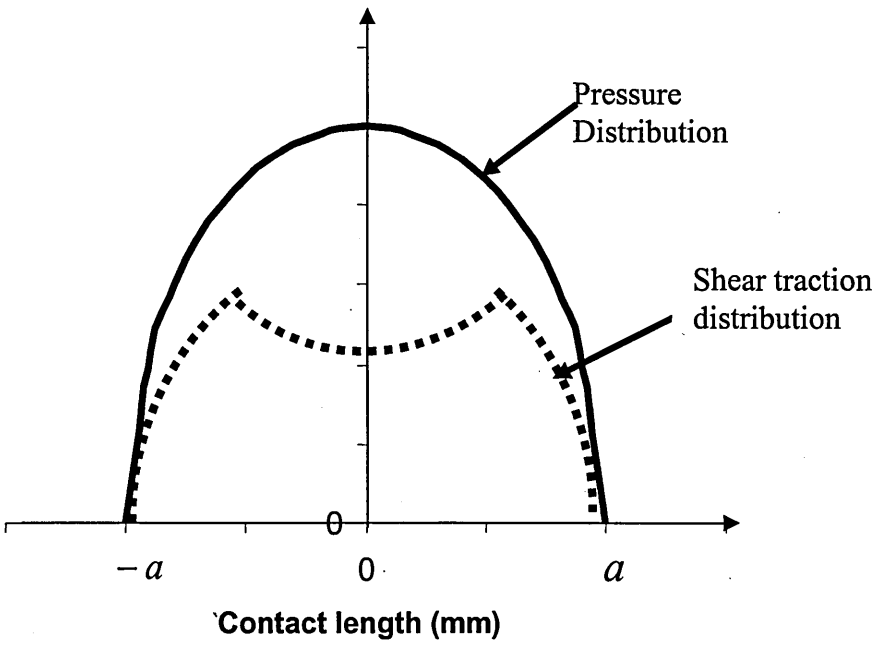

Figure 2.5 – Typical pressure and shear traction distribution for a Hertzian contact [43].

Contact of flat rounded contacts

A closed form elastic analytical solution for the contact pressure distribution for a flat with rounded edges was given by Ciavarella. et al **[46]** .

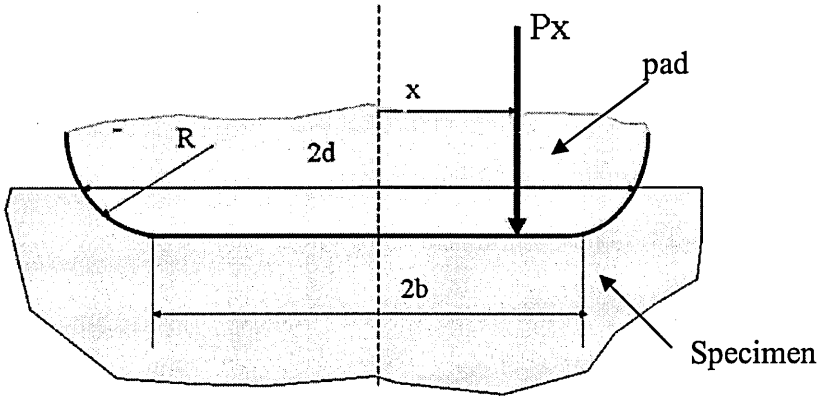

Figure 2.6 –Contact geometry with flat rounded edges

Considering the geometry, as schematically illustrated in Figure 2.6 the contact pressure distribution for the half flat length of b and corner radius of R, is given by

$$\frac{p(\phi).d}{P} = -\frac{2/\pi}{\pi - 2\phi_0 - \sin 2\phi_0} \times \left\{ (\pi - 2\phi_0)\cos\phi + \ln\left[\left| \frac{\sin(\phi+\phi_0)}{\sin(\phi-\phi_0)} \right|^{\sin\phi_0} x \left| \tan\left(\frac{\phi+\phi_0}{2}\right) \tan\left(\frac{\phi-\phi_0}{2}\right) \right|^{\sin\phi_0} \right] \right\} \quad \text{-(2.5)}$$

P is the nominal (average) contact pressure and p(ϕ) is the contact pressure at a distance x from the centre of the contact. The distance d is the actual contact length.

The value of ϕ_0 is determined from the overall equilibrium for the contact and is given as:

$$\frac{4PR(1-\upsilon^2)}{b^2E} = \frac{\pi - 2\phi_0}{4\sin^2\phi_0} + \frac{\cot\phi_0}{2} \qquad \text{-(2.6)}$$

where E and υ are Young's modulus and Poisson's ratio of the material.

The angle of ϕ is related to the distance along the contact using the equation

$$x = b\frac{\sin\phi}{\sin\phi_0}; \qquad -d \le x \le d \qquad \text{-(2.7)}$$

$$d = \frac{b}{\sin\phi_0} \qquad \text{-(2.8)}$$

The pressure distribution calculated based on equation 2.5 for the current application for 260 MPa average contact pressure is shown in Figure 5.4 in Chapter 5.

2.3.1 Fretting damage prediction

Fretting damage prediction methodologies can be grouped into three categories. They are:

(1) Empirical equations specifically determined for fretting situations,

(2) Multiaxial based criteria and

(3) Fracture mechanics approaches.

All these methodologies are based on the accurate determination of local stress/strain distributions.

2.3.1.1 Empirical equations

Nishioka and Hirakawa **[47]** argued that under fretting conditions, the fatigue strength is mainly characterised by the stress state in the fretted area and the stress state is mainly influenced by the alternating shear in the surface which arises from the frictional force. For a Hertzian type contact they derived the equation 2.6.

$$\sigma_{fw1} = \sigma_{w1} - 2\mu p_0[1 - \exp\left(-\frac{\delta}{K}\right) \qquad \text{-(2.9)}$$

Where,

σ_{w1} - Fatigue strength in the absence of fretting

δ - Slip amplitude

μ - Coefficient of traction

K - Material constant determined experimentally

σ_{fw1} - Stress to initiate a fretting crack

They have observed that the theoretical results agree well with the experimental observations with slip amplitude below $20\,\mu m$. They have attributed the non agreement above 20 μm slip region to the domination of wear process under gross slip condition. Analysing the equation 2.9, they further suggested conditions to mitigate fretting damage as: raise the fatigue strength, reduce the slip amplitude and contact pressure.

Ruiz et al **[23]** studied the effect of fretting three different materials commonly used in gas turbine engines. Explaining the crack initiation behaviour at dovetail joints of turbine blade and the disk, they proposed a "Fretting Damage Parameter" (FDP)

specific to the fretting. The FDP was defined as the product of contact shear stress at the contact surface and the slip amplitude and is given as

$$FDP = \tau_{xy}\delta \qquad \text{-(2.10)}$$

They argued that the combination of the slip amplitude and the interface shear stress is more appropriate to describe fretting damage. The FDP gives a measure of amount of fretting damage per cycle. Further, assuming that the further crack growth is governed by the bulk tangential stress (σ_{xx}), the combined Fretting Fatigue Damage Parameter (FFDP) was defined as

$$FFDP = \left(\sigma_{xx}\tau_{xy}\delta\right)_{\max} \qquad \text{-(2.11)}$$

2.3.1.2 Application of multiaxial fatigue parameters

Similarities between the features of cracking and observations of multiaxial fatigue and observations of the formation of cracks in fretting fatigue leads to application of multiaxial fatigue and damage concepts to the analysis of fretting problem **[14, 48]**.

Dang Van's Criteria

Dang Van et al **[49]** has proposed a method for predicting fatigue life under high cycle fatigue conditions. This model was based on the observation that fatigue crack nucleation is a local process and begins within grains that have undergone plastic deformation.

The analysis is carried out by sub dividing a structure into sub divisions (similar to a mesh in finite element analysis). Analysis for fatigue failure can be carried out for any of the sub divisions to analyse the possibility of cracking at that point. First, the point concerned is confined to a macroscopic elementary volume and further that

volume is sub divided into mesoscopic volumes. According to Dang Van et al **[49]**, the stress tensor at this scale results from the macroscopic one and the local residual stresses.

The Dang Van's Criteria is given as an inequality related to the mesoscopic stresses at all instants (t) of a loading cycle as follows.

$$\max\{\tau(t) + ap_{h(}(t) - b\} \leq b \qquad \text{-(2.12)}$$

Where, p_h is the Hydrostatic stress, $\tau(t)$ is Instantaneous mesoscopic shear stress and m, n are material constants evaluated experimentally.

The fatigue resistance is checked point by point analysing the quantity $DV = \frac{\max\{\tau(t) + ap_{h(}(t) - n\}}{b}$ The positive value of the DV means occurrence of fatigue cracking. Dang Van and Maitournam **[50]** have applied this criterion to the fretting problem and have obtained satisfactory predictions.

Application of the SWT parameter

Smith, Watson and Topper **[28]** have proposed a model to describe the fatigue life in push pull tensile compression. It was expressed as

$$\sigma_{n,\max}\left(\frac{\Delta\varepsilon}{2}\right) = \frac{\sigma_f^2}{E}(2N_f)^{2b} + \sigma_f\varepsilon_f(2N_f)^{b+c} \qquad \text{-(2.13)}$$

Where,

σ_f .Fatigue strength coefficient

b - Fatigue strength exponent

ϵ_f - Fatigue ductility coefficient

c- Fatigue ductility exponent

E - Young's modulus

N_f - Number of cycles to initiate a crack of a given length

$\Delta\epsilon$ - Strain range in the principal plane

$\sigma_{n,Max}$ - Maximum normal stress on the principal strain range plane

Szolwinski and Farris [14] applied a modified SWT parameter based on critical plane orientations successfully to predict the fretting crack initiation. They assumed that the crack nucleation occurs on a plane where the combination of strain amplitude and the maximum normal stress is maximum and not necessarily the maximum principal strain amplitude or the maximum normal stress at a given point. The SWT parameter has been successfully applied to the fretting problem by several researchers assuming that the fretting damage process is a mode I cracking problem. **[4, 14, 58, 61, 64, 65, 66, 67, 68, 69, 70].**

Stress gradient effect considerations

Araujo and Nowell **[61]** applying the SWT parameter point out that the stress concentration is extremely localised and fretting cracks nucleate at points of high

localised stresses similar to a notch situation. But the multiaxial crack initiation parameters do not account for the stress gradients. In fretting situations a high stress field exists in the vicinity of the contact and rapidly decays when moving into the material. For more rapidly varying stress fields, the high localised (surface) maximum is not sufficient to fully describe the crack initiation and growth unless the parameter concerned is sustained over a considerable length or volume. Therefore, they proposed an averaging methodology over a length or a volume.

The averaging methodology is basically based on the fact that the high stress must be sustained over a critical volume in order for a crack to rupture through the strongest micro-structural barrier.

Fouvry et al **[71]** have introduced a methodology of averaging parameters over a volume in order to take into account the high stress gradient exist in vicinity of the contact surface. Proudhon et al **[67]** have adopted this technique and analysed for 2024-T-351 alloy and found a good correlation for the average grain size of the material with the process volume. Further, Munoz et al **[69]** compared the process volume for 2024-T-351 and 7075-T651 alloys and found that the process volume cannot correlate with the grain size for 7075-T651 alloy. During the same period, Proudhon et al **[68]** proposed a variable process volume approach.

New advancements were made by the application of the SWT parameter for the fretting wear damage process by McColl [3], Ding et. al. [17], Ratsimba et al [72] and Madge et al [73].

A modified version of the SWT parameter was proposed by Ding et al **[74]** in order to capture the type of damage in the mixed slip regime and the damage in the gross slip regime separately. A modified Ruiz parameter in conjunction with the SWT parameter was also proposed by Vidner and Leidich **[75].**

Fatemi and Socie (FS) parameter

Fatemi and Socie **[16]** proposed a model based on the shear strain amplitude in a critical plane, for mode II cracking. Their model was expressed as;

$$\frac{\Delta\gamma_{Max}}{2}\left(1+\alpha\frac{\sigma_{n,\max}}{\sigma_y}\right)=\frac{\tau_f^1}{G}(2N_f)^{b_\gamma}+\gamma_f(2N_f)^{c_\gamma} \qquad \text{-(2.14)}$$

Where,

$\Delta\gamma_{Max}$ – Maximum shear strain range

σ_y - yield strength

$\sigma_{n,Max}$ - Maximum stress acting normal to the plane with maximum shear strain range

τ_f^1 - Shear fatigue strength coefficient

G - shear modulus

b_γ – Shear fatigue strength exponent

c_γ- Shear fatigue ductility exponent

N_f - Number of cycles to initiate a crack of a given length

α - is a constant

2.3.1.3 Fracture mechanics approach

Fracture mechanics is an approach which can be used to estimate and predict fretting fatigue life **[1, 2, 14, 23, 47, 51-60, 76-80].**

Such methods are based on establishing the stress intensity factor ΔK for cracks initiated in the contact zone. Calculation of the number of loading cycles, from an initial crack to failure was integrated using a Paris type crack propagation law.

$$N = \frac{1}{C}\int_{a_i}^{a_f} \frac{da}{\Delta K(a)^m} \qquad \text{-(2.15)}$$

where,

a_f - is the crack size at failure

a_i - the initial crack size,

ΔK - is the range of the stress intensity factor (that depends on the crack size c)

C, m - are material parameters.

In early work of Nix and Lindley **[11, 60]** a fracture mechanics based procedure was used to predict fretting fatigue damage. However, in their analyses they assumed that the cracks propagates normal to the contact surface although in practice the actual cracks are typically generated oblique to the surface an angle at about 15^0 – 45^0. Furthermore they only used mode I stress intensity factors in the analysis.

Faanes and Fernando **[52]** also have used LEFM approach to predict fretting crack growth. Crack propagation was evaluated by assuming a growth law of modified Paris type:

$$\frac{da}{dN} = C\left[\Delta K_{eff} - \Delta K_{th}(a)\right]^m \qquad \text{-(2.16)}$$

Here, ΔK_{eff} was calculated taking into the multiaxial stress state incorporating the bulk stress, normal and friction, and $\Delta K_{th}(a)$ is the threshold stress intensity factor, modified to account for small cracks through the relationship proposed by El Haddad **[93].** They have correlated the threshold stress intensity factor range for a short crack through an intrinsic crack length a_0, as follows.

$$\Delta K_{th}(a) = \frac{\Delta K_{th}(\infty)}{\sqrt{1 + a_0 / a}} \qquad \text{-(2.17)}$$

Where,

a - is the crack size

ΔK_{th} - is the threshold stress intensity for a long crack.

The a_0 was evaluated from

$$a_0 = \frac{1}{\pi}\left[\frac{\Delta K_{th}(\infty)}{\Delta \sigma_{FL}}\right] - a_i \qquad \text{-(2.18)}$$

Here,

a_i is an "initial crack length" normally assumed to be the surface roughness

$\Delta \sigma_{FL}$ is the uniaxial fatigue limit.

Mutoh and Xu **[36]** introduced a new concept based on the stress field near the contact. Based on experimental observations that fretting cracks initiate at very

shallow angles to the surface and follows the direction of the maximum shear stress, they assumed that the fretting crack initiation is in the direction of the maximum shear stress, and the crack changes direction to the direction of maximum normal stress, after propagating for a few micrometres.

In this method it is very important to ascertain the crack initiation location and the location is assumed to be the point where, the most severe stress concentrated point on the contact surface. The crack path is predicted in steps assuming that the crack will initiate in the maximum shear stress direction and propagate in the maximum normal stress direction.

2.4 Experimental Techniques in fretting fatigue.

Generally, experimental investigations are focused on unveiling the influence of certain parameters which influence fretting damage processes. One objective of fretting damage experiments is to monitor fretting crack initiation and propagation under different loading conditions.

Hills and Nowell **[62, 63]** categorise fretting experiments into three groups depending on the objective of the experiment

1. Simulation of real engineering problems - The objective of these tests are to reproduce as accurately as possible, either full size or possibly on a reduced scale, the contact problem. This type of experiment is of great advantage to designers, as the results obtained from tests, could be applied without modification to real engineering problems.

2. Material ranking tests – The objective of this type of tests is to assess a materials resistance to fretting damage.

3. Idealised fretting fatigue tests - These tests are carried out in certain conditions to understand the influence and contributions of individual parameters to fretting fatigue. The objective of these tests is to understand the mechanics and underlying processes of fretting fatigue phenomena.

Out of the above three categories, simulation of a real engineering problem is more difficult since in most of the cases new experimental rigs need to be designed. In some cases, it might be extremely difficult to simulate the real contact conditions and associated stress fields under laboratory conditions.

2.4.1 Idealised fretting experiments

Generally, the design of idealised fretting experimental set-ups can be broadly classified into two categories, (i) bridge pad contact arrangement and (ii) single contact arrangement.

2.4.1.1 Bridge pad type contact arrangement.

This is a simple arrangement to carry out fretting experiments. A schematic diagram and a pictorial view of a bridge type test set-up is shown in Figure2.7.(a) and Figure 2.7(b) respectively.

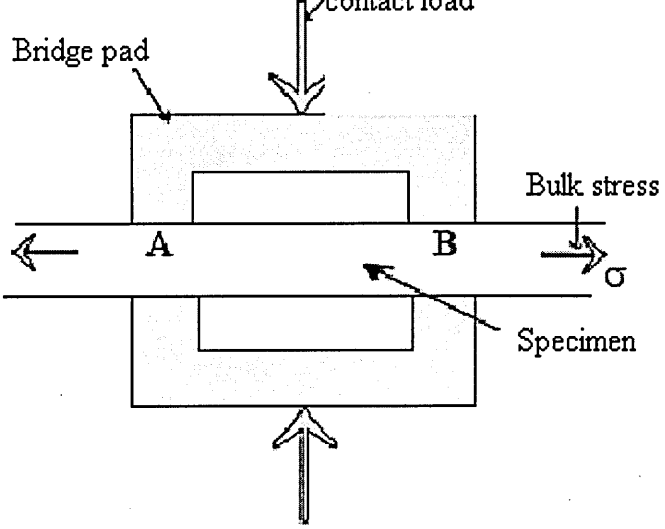

Figure 2.7 – Bridge pad type contact arrangement

In this arrangement, a cyclic bulk stress (tensile or bending) is applied to the specimen and a contact pressure is applied to the contact pad by means of a proving ring. This simple design provides the advantage of creating stick or slip sliding conditions by varying the distance between the two contacts of the bridge or the bulk cyclic stress. The slip amplitude is calculated knowing the distance between the bridges and the cyclic stress amplitude.

The contact pressure is varied by adjusting the screws of the proving ring and is measured by measuring the strain on the ring by means of strain gauges.

Although this is a simple arrangement to carry out fretting experiments its limitations are.

- The slip amplitude can not be calculated without knowing the bulk stress, bridge length and material parameters.

- If this arrangement is used with a rotating bending test set-up, it is difficult to continuously monitor the contact load and the friction force.

2.4.1.2 Single contact arrangements

In contrast to the bridge pad type experimental rigs, the single contact experimental arrangements use only one pad and the contact can be of rounded, flat- rounded or flat geometry. Two different designs are described in the literature. They are explained as Design type A and Design type B below.

Design type A

A schematic diagram of the design is shown in Figure 2.8. A hydraulic test machine is used to grip a specimen and apply a cyclic stress load. Due to the elasticity of the material, the specimen expands and contracts under the cyclic bulk load. But at the same time, the pads are held in a fixed position, by a fretting fixture. The two bodies, the pad and the specimen, rub against each other as shown in Figure 2.8. The slip amplitude is related to the bulk stress range.

Although this experimental set-up is simpler, it has the following disadvantages

- Slip amplitude needs to be calculated from the material properties and cyclic loading of the specimen.
- The dominant feature of the slip generating method is that always a slip-stick condition prevails and only the stick-slip condition can be investigated

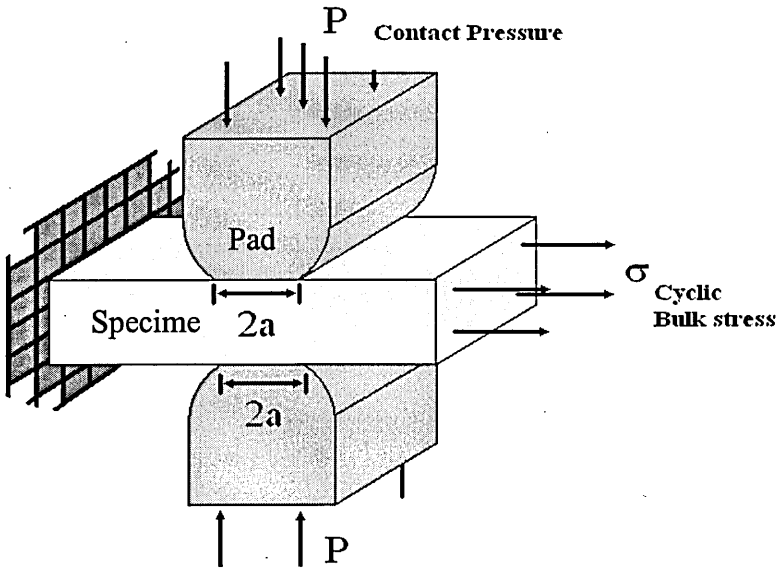

Figure.2.8. – Test set-up with axial cyclic stress only

Design type B

This set-up is capable of generating independent cyclic movement with respect to the specimen while the specimen is subjected to cyclic loading independently. A schematic diagram of the design is shown in Figure.2.9.

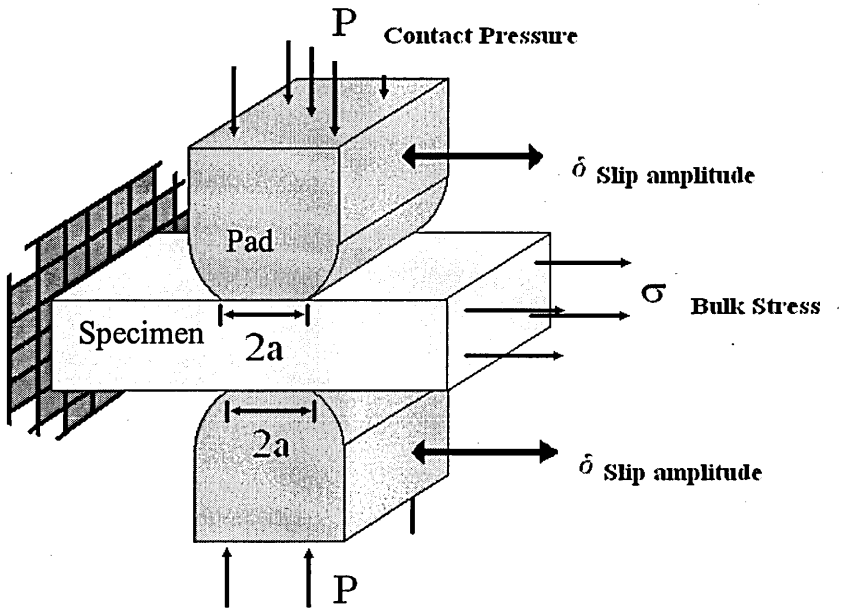

Figure.2.9. – Test set-up with axial stress and independent movement of pads

A hydraulic test machine is used to grip a specimen and apply a bulk cyclic load to the specimen. One end of the specimen is fixed and a cyclic load is applied to the other end. Fretting pads are pressed by a static load in a direction perpendicular to the length of the specimen. Independent cyclic movement of the fretting pad in a direction parallel to the length of the specimen is applied by means of either mechanical or hydraulic devices.

The main features of this design are:

- The movement of the fretting pad is parallel to the direction of bulk stress and the fretting pads can move independently, in-phase or out-of-phase to the bulk stress.
- Capable of simulating all slip regimes (stick, stick-slip, gross slip).

Jin and Mall [36] have used this configuration and observed different slip regimes with change of the slip amplitude.

It should be noted at this point that the stress field of the current investigation is entirely different from Design type A and Design type B. While the bulk cyclic stress is parallel to the slip direction in the design type A and B, the slip direction in the current investigation is in perpendicular direction to the bulk stress. The design and development of the new experimental set-up is described in the next chapter.

2.5 Crack nucleation site and Crack path.

Experimental observations on crack nucleation site and the crack path are of importance for numerical analysis procedures. Researchers have observed that cracks are nucleated within the contact zone and fretting cracks originate oblique to the contact surface [56, 78, 66, 79] .

Vallelano et al [56] have reported that the cracks were nucleated within the contact zone and cracks were formed at small angles to the surface and soon kinked at 60^0-90^0 angle with the horizontal.

Further they have observed that the crack path turned at around 20 μm depth. They have carried out the tests with a spherical contact on a Al7075-T6 material where the average grain size was measured to be 30 μm.

Munoz et al. [60] analyzing two different aluminium alloys 2024-T351 and 7075-T651, reported that cracks start from the contact surface at an angle closer to 55^0 and when the crack further grow, very close to the surface, the crack changes to form an angle of 70^0 - 75^0. Further they have observed that the initial crack angle changed at around 50 μm depth for 2024-T351 material and around 100 μm depth for 7075-T651 material.

CHAPTER 3: DEVELOPMENT OF A NEW EXPERIMENTAL SET-UP

A novel experimental set-up has been designed and developed specifically to investigate the fretting damage behaviour of the pressure armour wires of flexible pipes. One of the main objectives of this investigation was to use the real engineering component under study, in experimental investigations and to simulate as far as possible the real operating conditions of the pressure armour wire nub and valley contact for fretting damage. In this chapter the approach and the design considerations which led to the development of the test rig are discussed.

3.1 Samples

The pressure armour is made of inter-locked steel wire wound in a helical shape as shown in Figure 1.2 (chapter 1), to form a metallic layer which will take mainly the hoop stress of the pipe. A sectional view of the pressure armour wire used by Wellstream International is shown in Figure3.1

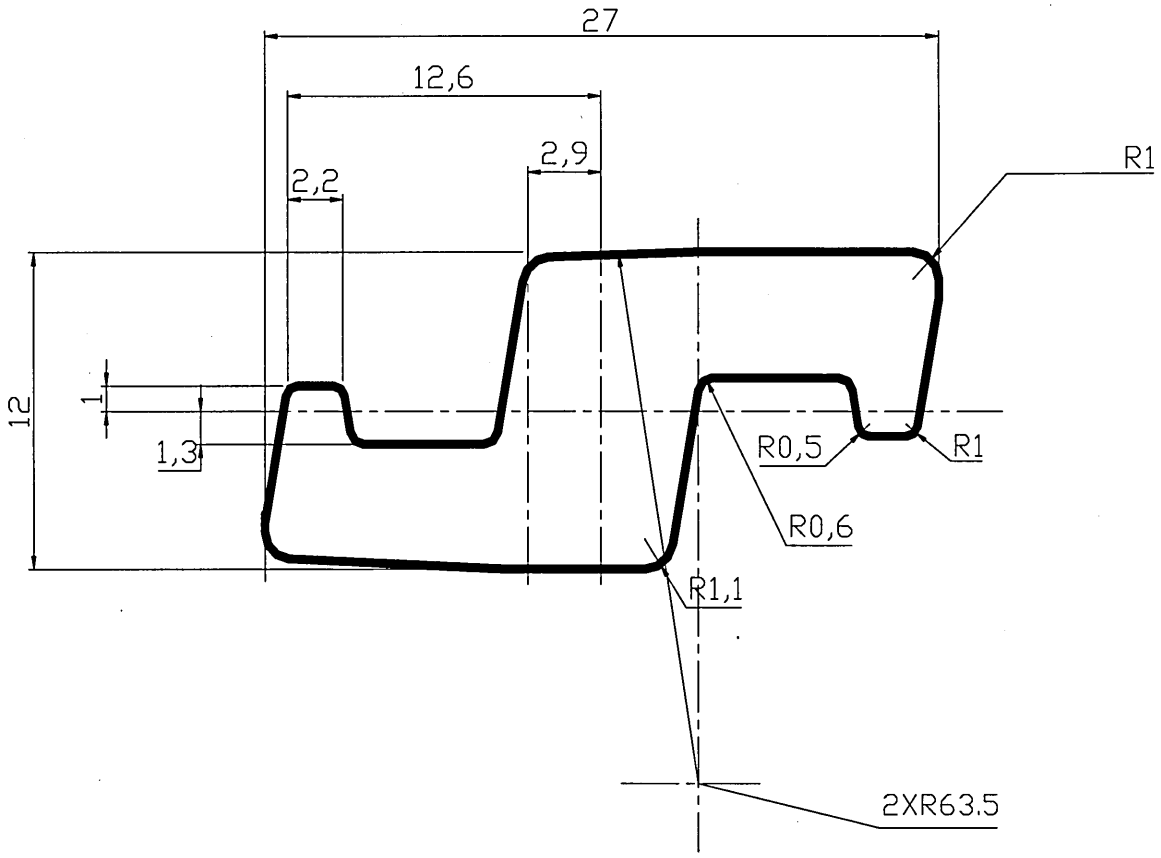

Figure.3.1 – sectional view of the pressure armour wire

12 mm size wire was selected for the experiments and all specimens and pads were made from this wire size.

3.2 – Requirements of the experimental set-up

The low angle helix winding of the wire creates an interlocked nub and valley contact arrangement. The kinetics and kinematics of the pressure armour wire under operational conditions are shown in the Figure 3.2.

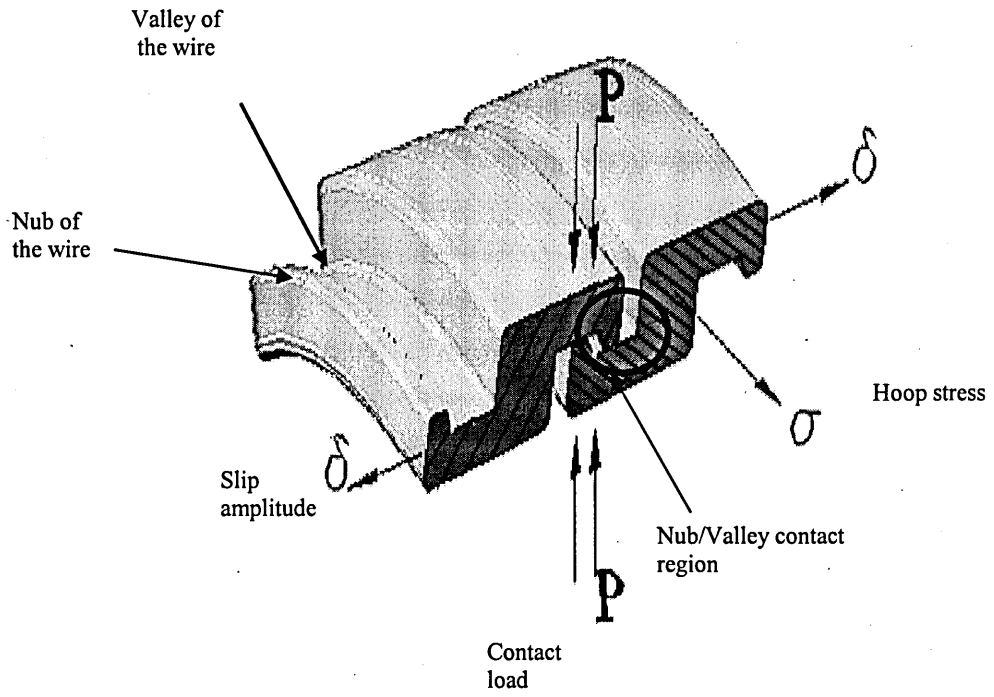

Figure 3.2 – Pressure armour layer contact details

Complex contact conditions exists in the nub and valley region of the pressure armour wire due to the contact pressure, slip and pipe hoop stress. In order to simulate these conditions, the test set-up should be able to reproduce the following

- Apply a bulk stress to the specimen, which is equivalent to the hoop stress in the real pressure armour wire under operational conditions.
- Apply a contact pressure between the specimen and the pad, which is representative of the equivalent pressure acting on the pressure armour wire resulting from the pressure of sea water and the pumping fluid and interaction of other metallic and polymer layers of the pipe.

- Produce small amplitude oscillatory movements in the nub and valley contact of the specimen-pad pair to simulate the relative movement in the pressure armour wire interlocking contact. This movement is generated in actual operational conditions from sea roughness and relative displacements of the floating production or storage system.

A schematic representation of an experimental configuration that would fulfil the above requirements is shown in Figure 3.3.

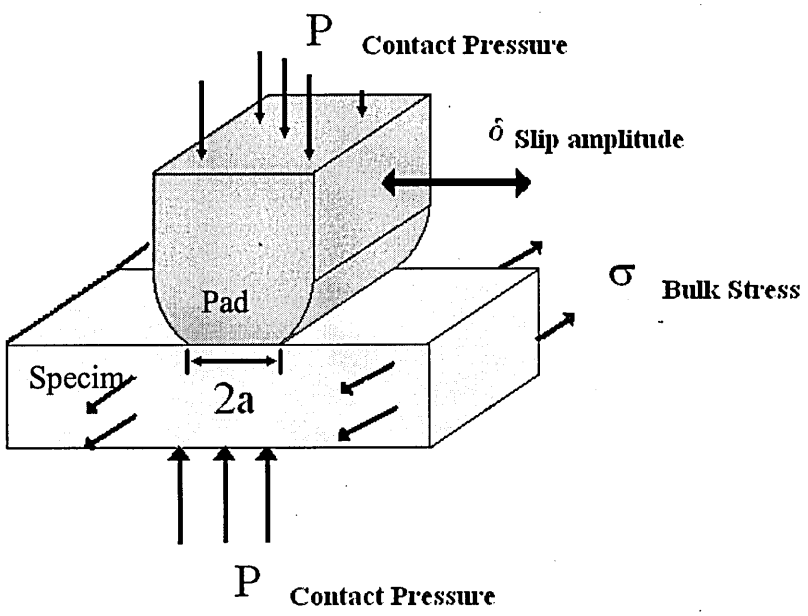

Figure 3.3 – Contact configuration in the experimental set-up

In contrast to the design type (A) and (B) discussed in chapter 2, in the new experimental set-up, the bulk stress to the specimen is applied perpendicular to the direction of pad movement.

The loading conditions that need to be simulated in the experimental set-up for the specimen and the pad made out of pressure armour profile are shown in Figure 3.4.

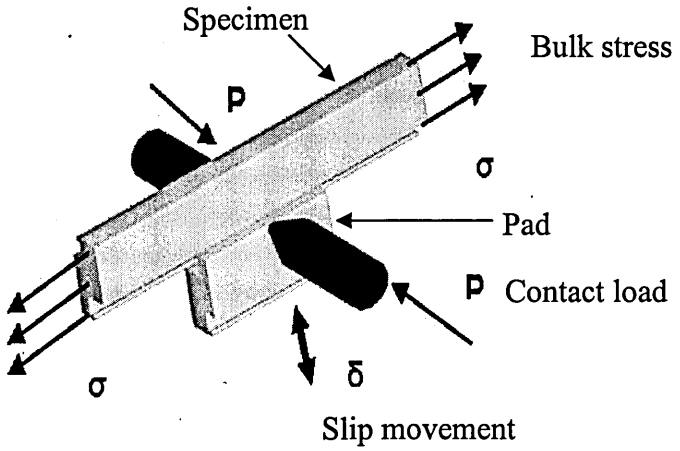

Figure 3.4 - Loading arrangement in the experimental set-up

3.3 The Design

In this set-up, two straight pieces of pressure armour wire, referred to as "specimen" and fretting "pad", are rubbed against each other. The specimen is subjected to an axial stress (σ) which represents the hoop stress in the pressure armour layer. The nub of the pad is pressed on to the valley of the specimen with a controlled contact load (P). The pad is oscillated lateral to the specimen with a controlled displacement (δ) to create the sliding action which ultimately results in fretting damage.

The ends of the specimen were modified by pasting grip plates as shown in Figure.3.5 using special epoxy glue to provide robust end gripping conditions.

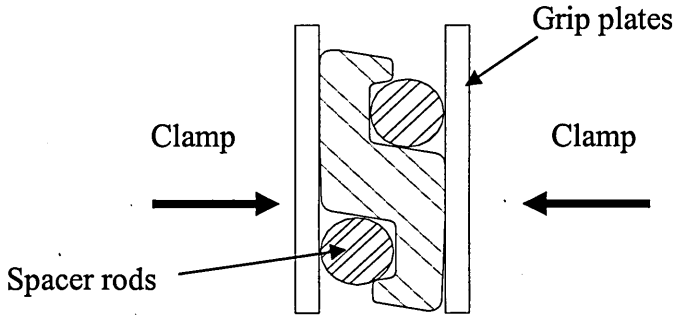

Figure 3.5– Modified ends of specimens for gripping.

After pasting and curing the glue, the ends were ground parallel to obtain greater accuracy in alignment when mounting for testing.

A schematic diagram of the test rig is shown in Figure 3.6 and a pictorial view of the test machine is shown in Figure 3.7.

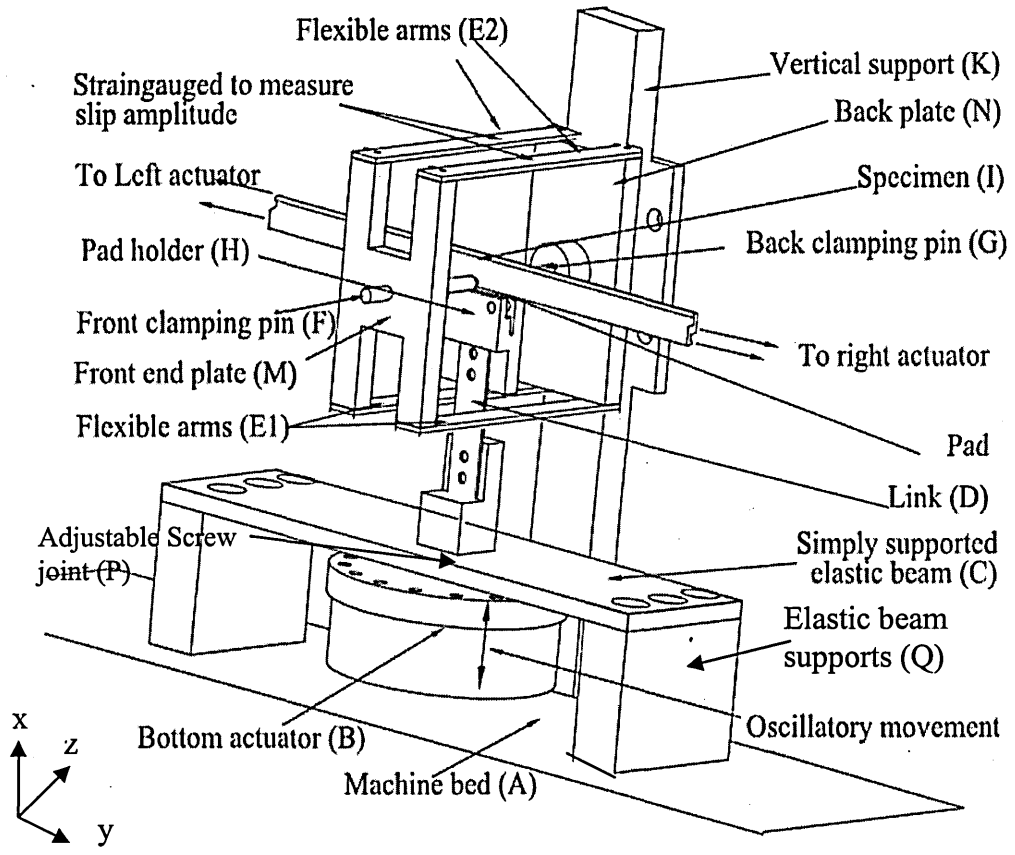

Figure 3.6 Schematic diagram of the test arrangement

A close-up view of the specimen loading arrangement is shown in Figure 3.8. The test set-up is equipped with a multiaxial digital servo-controller and a data acquisition system to collect transient and periodic data of bulk stress, slip amplitude, contact pressure, friction force and number of cycles.

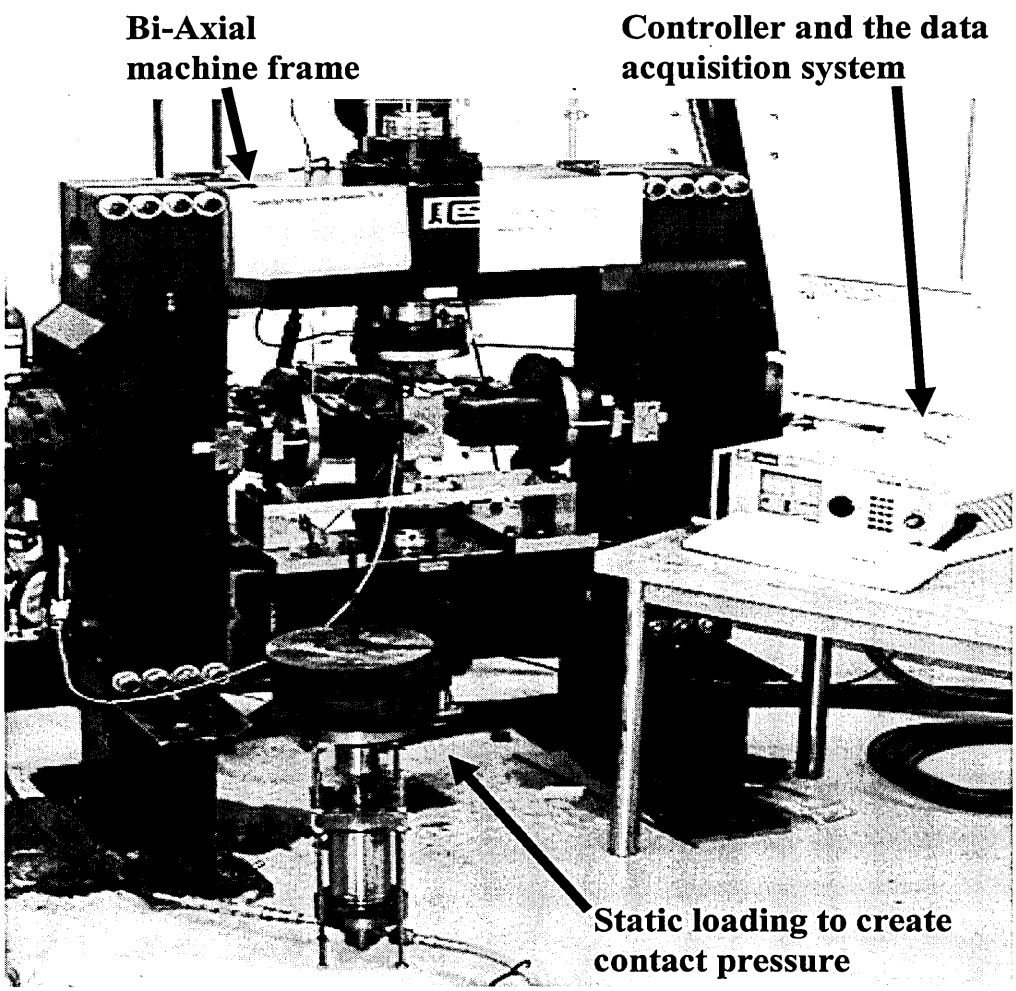

Figure 3.7 A pictorial view of the test set-up.

The test rig was built up on a multiaxial testing machine composed of four servo-controlled hydraulic actuators. The two horizontal actuators (left and right) were used to apply the bulk stress (σ) on the gripped specimen. The right actuator was controlled in position control mode to keep the centre position of the specimen fixed whilst controlling the left actuator in load control to apply the bulk stress to the specimen.

The specimen is rigidly attached to the actuators and loaded using mechanical wedge grips as shown in Figure 3.8. The fretting pad is mounted in a holder and the holder is supported to eliminate undue rotation of the pad during loading. The pad holder is connected to the bottom actuator which generates a low amplitude slip

between the specimen and the pad. The top actuator is connected to the centre of the specimen to avoid lateral bending of the wire during loading.

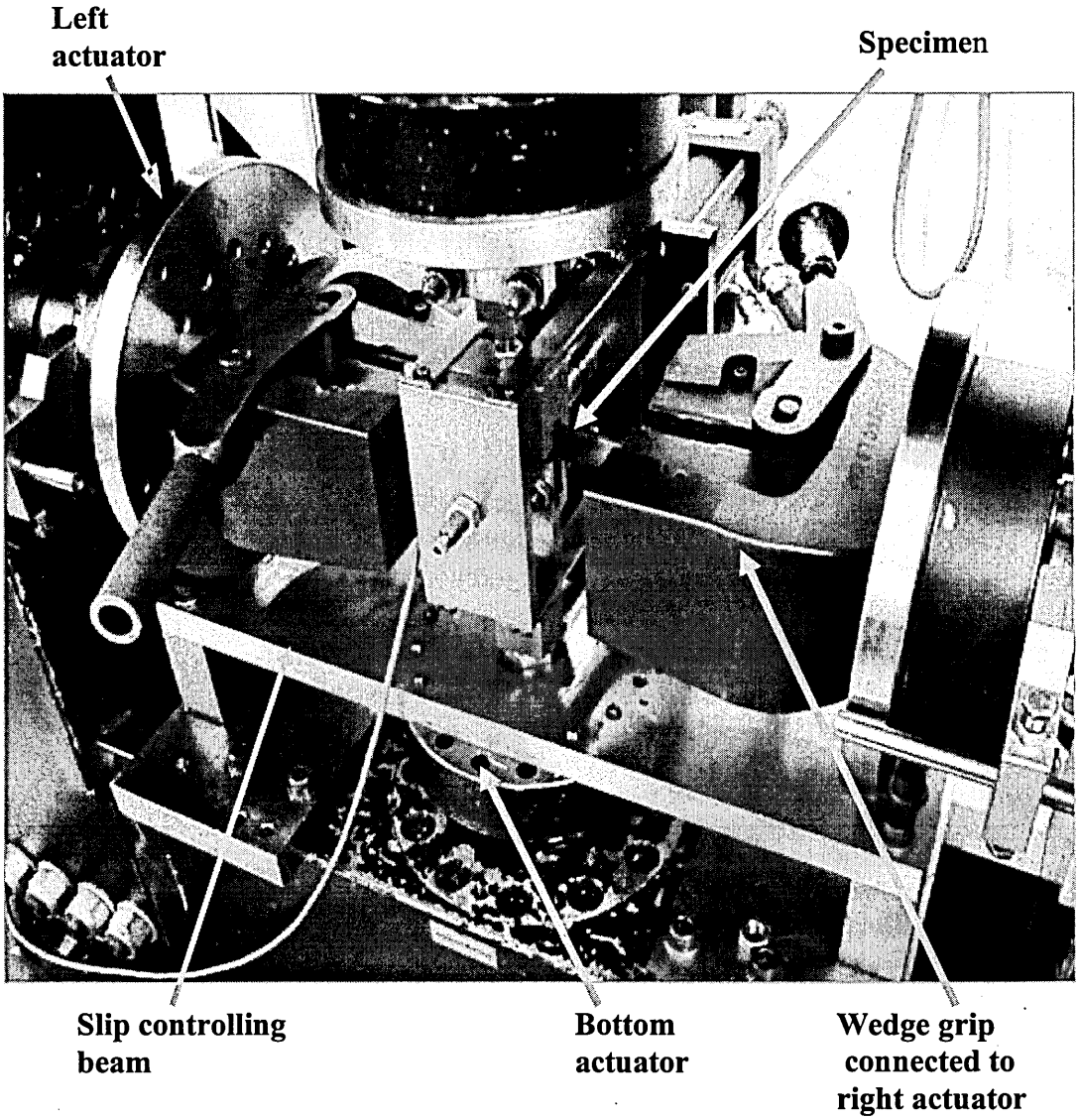

Figure 3.8 Close-up view of the specimen loading.

3.3.1 Control and measurement of contact load

It was necessary to develop a mechanism to apply contact load between the specimen and the pad so that the pressure on the pad can be controlled independent of the vertical movement (slip) of the pad. This was achieved by means of a flexible frame. The back plate of the frame N (Figure 3.6) is connected to the machine bed through the vertical support K. The front clamping pin F on the front end plate M is free to move vertically through the set of flexible arms E1 and E2. The back clamping pin G, located on the back plate N, is pressed onto the specimen. The front clamping pin is pressed onto the pad. This arrangement allows the pad and the front clamping pin F to move relative to the back clamping pin and the specimen without significant resistance. The front clamping pin F in contact with the pad is shown in Figure 3.9.

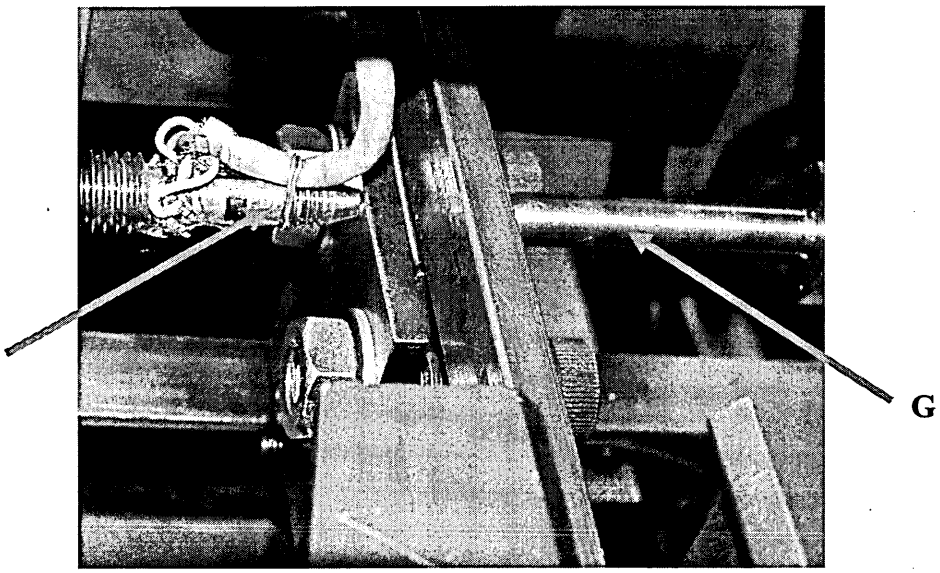

Figure 3.9 Front clamping pin F and back clamping pin G, in contact with the pad.

Strain-gauges attached to the front clamping pin are calibrated to measure contact load. The contact pressure is controlled by adjusting the position of the front clamping pin and applying a static load to the back clamping pin by means of a hydraulic actuator.

3.3.2 Measurement of friction.

The friction was measured as shown in Figure 3.10 by a strain gauged arm (link D), fixed in between the fretting pad holding clamp and the flexible vibrating plate. The link D was calibrated previously using static loads to measure the friction force of the contact.

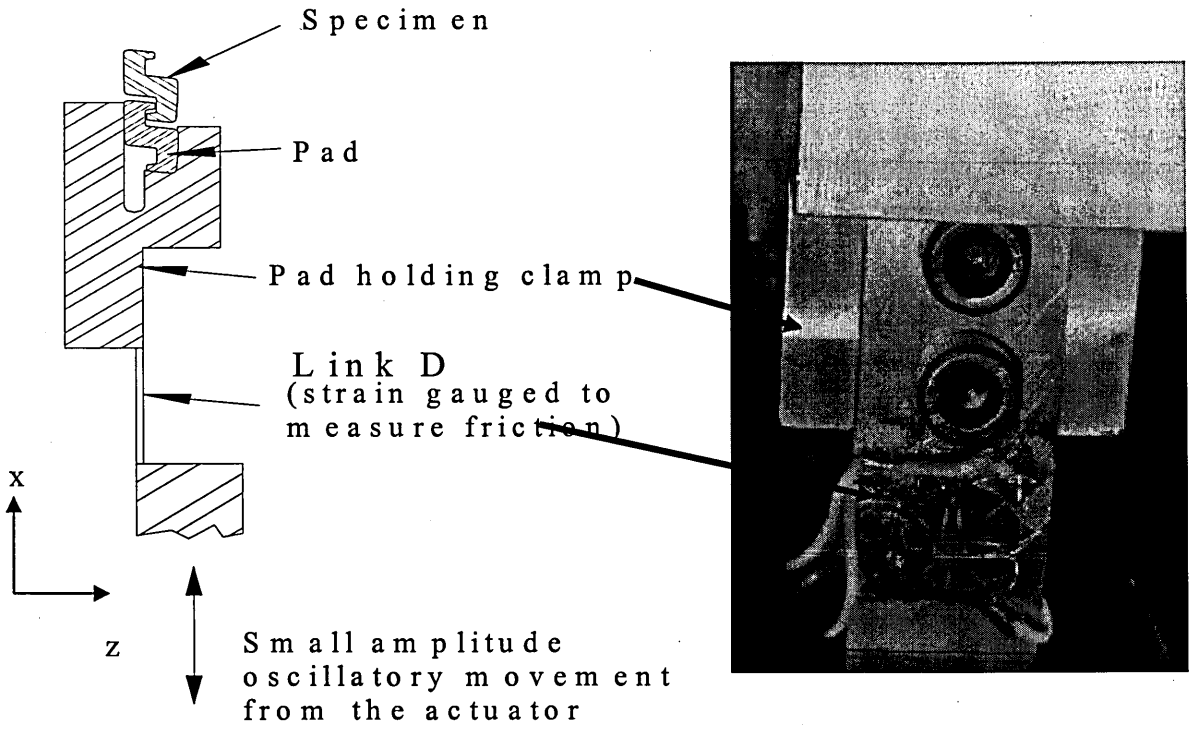

Figure.3.10(a) schematic **Figure.3.10(b) Pictorial**

Figure 3.10 - Arrangement to measure friction force

3.3.3 Low slip amplitude generation.

Due to the level of precision required in controlling slip between the specimen and the (fretting) pad, it was necessary to design an arrangement that allows accurate control of the slip amplitude in the range from 5μm to 500μm. The control of the pad displacement was accomplished by means of the simply-supported elastic beam as shown in Figure 3.11(C in Figure 3.6). The centre of the beam C was directly connected to the bottom actuator. The pad holder H was connected to the beam C through an adjustable link system D. In this arrangement, the movement of the pad holder was controlled by controlling load applied from the bottom actuator. This arrangement has been shown to work successfully **[83]**, generating very small amplitudes of slip using frequencies of up to 20 Hz with high precision.

The slip amplitude was measured by strain gauging the flexible arms (E2), which flex proportionately to the slip between the specimen and the fretting pad.

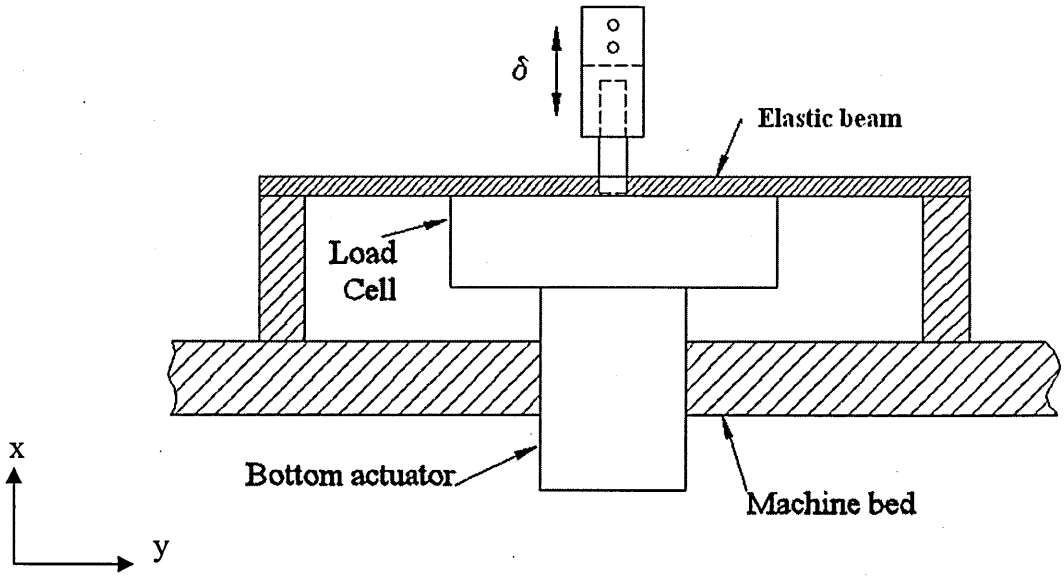

Figure 3.11- Low amplitude slip, generating arrangement.

3.4 Alignments.

Two critical alignments were taken into account at the design stage of the machine. One is the parallelism of the pad and specimen when in contact (along the contact length). The other is the alignment of the friction measuring arm in order to prevent the arm from bending when in operation. These issues are briefly discussed as follows.

(1) The parallelism of the specimen and the pad is a critical issue as it is necessary to make sure that the contact load is equally distributed along the contact area. In order to make adjustments, an adjustable screw joint (P in Figure 3.6) was designed in between the vibrating plate and the friction measuring arm. The adjustable screw is shown in Figure.3.12.

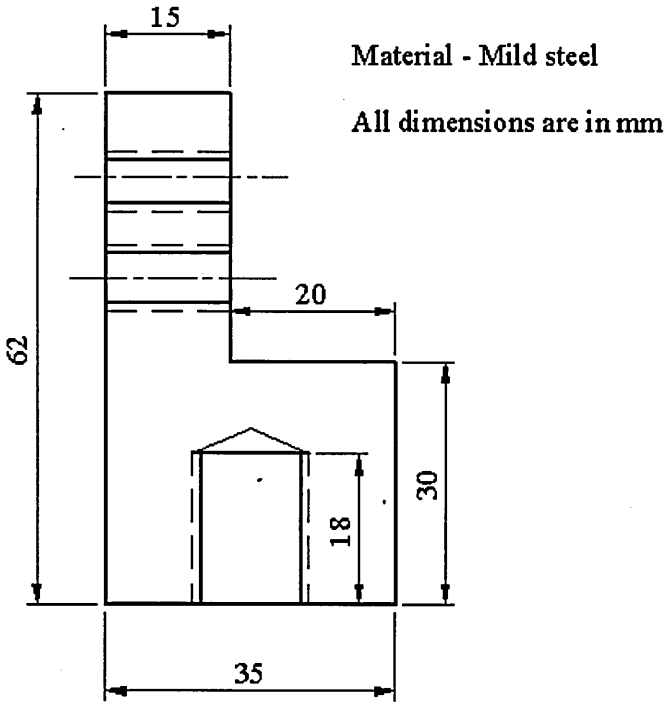

Figure 3.12 Adjustable screw joint

The pressure distribution was measured by "pressurex®" strips for each test and adjustments were made if necessary. The post test specimens were measured along the contact in order to confirm the equal wear or damage profile along the contact, and this data is given in experimental results section (Chapter 4).

(2) The other critical alignment is to prevent bending of the friction measuring arm when applying the contact pressure. This was achieved by proper design of jaws, their location and location of the load measuring arm in the flexible vibrating plate. Figure. 3.13 (a) shows the proper design to prevent bending and Figure.3.13(b) shows how the arm is bending when specimen is away from the pad.

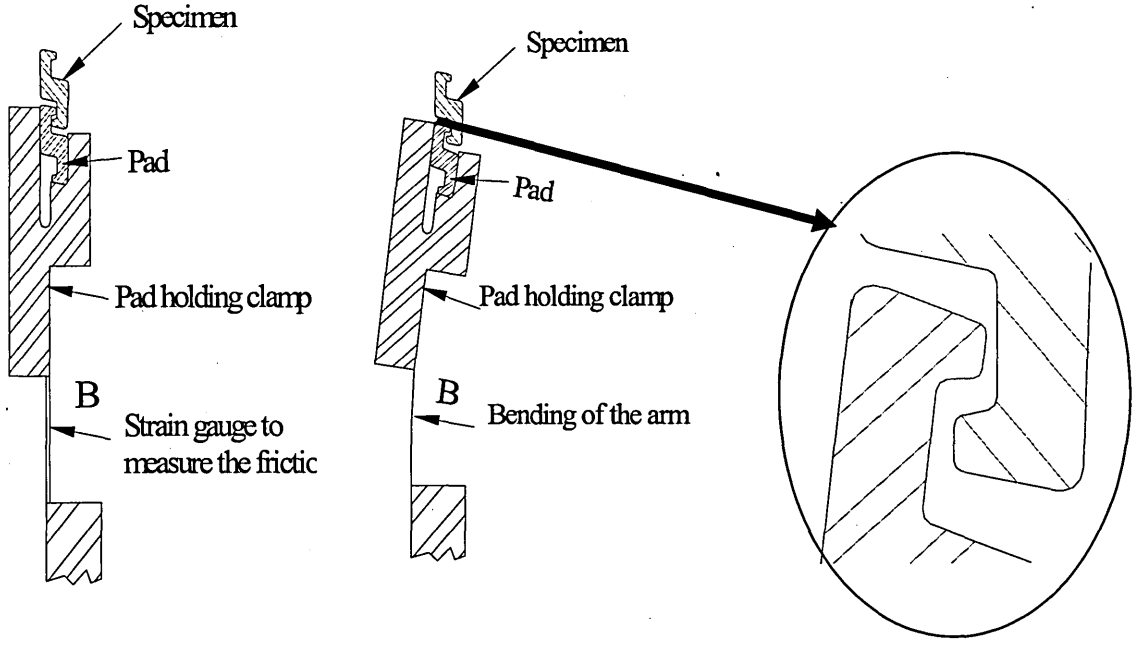

Fig.3.13 - Effect of incorrect alignment

Further, this misalignment can cause incorrect geometry of contact in the valley of the specimen which could invalidate the whole experimental investigation.

Load measuring transducers were calibrated and suitable trips were set in order to confirm safe operation of the machine. A series of calibration tests have been carried out prior to the experimental investigations in order to confirm the satisfactory operation of the experimental set-up. A pictorial view of the displacement calibration is shown is Figure 3.14 and the calibration data is given in Table 3.1

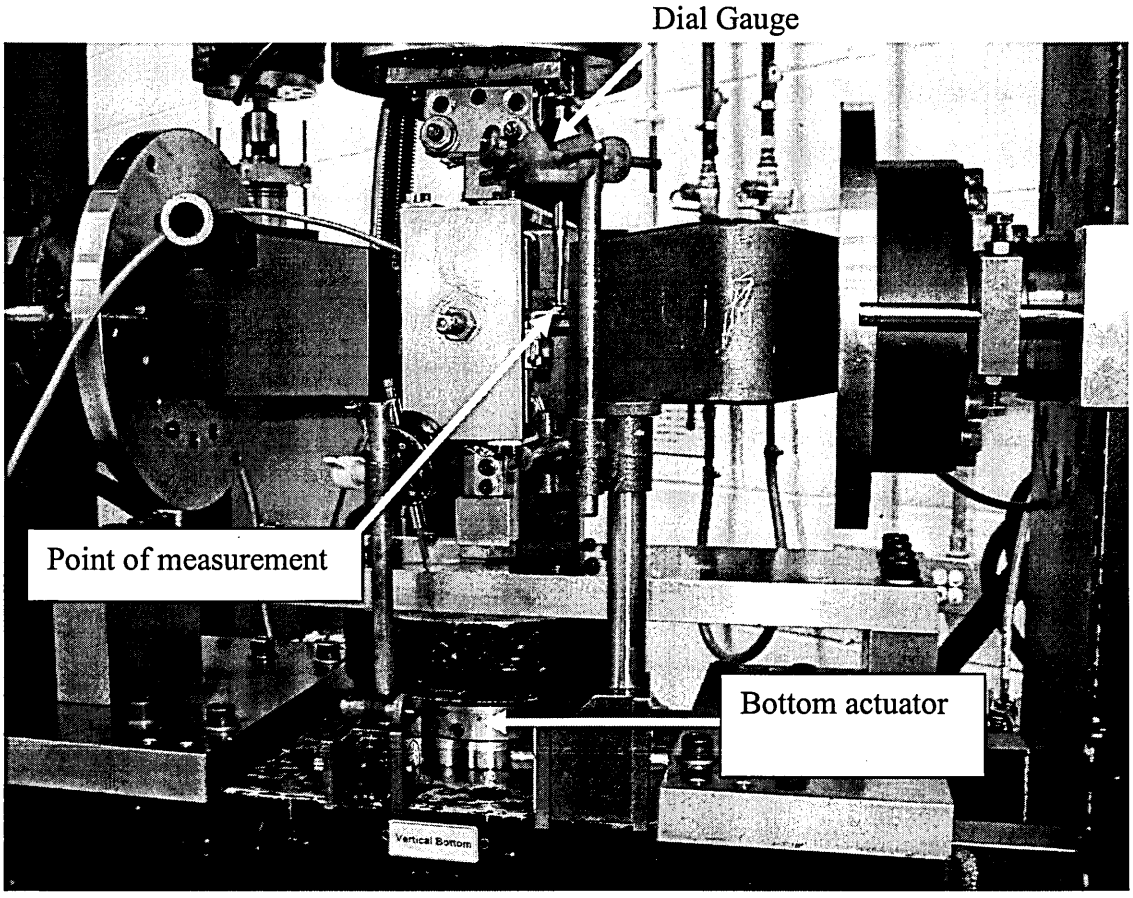

Figure 3.14 - Calibration of the displacement transducer

Table 3.1 - Calibration data for the displacement transducer

No	Strain gauge reading (μm)		Dial gauge reading (μm)	
	Loading	**Un-loading**	**Loading**	**Un-loading**
1	0	0	0	0
2	50	50	55	55
3	100	100	110	105
4	150	150	160	165
5	200	200	215	210

CHAPTER 4 – EXPERIMENTAL RESULTS

A comprehensive test programme was carried out using the novel experimental facility described in Chapter 3. The schedule of experiments was chosen to cover a wide range of parameters known to have a significant influence on the fretting damage process and to enable a systematic study of the associated phenomena.

The 12 mm size pressure armour wires supplied by Wellstream International Ltd, was chosen for the experimental investigation. Tests were carried out using the novel experimental facility described in Chapter 3. Prior to the testing, all specimens were cleaned and degreased with acetone and were inspected under optical microscopy to ensure that the specimens are defect free. Experiments were carried out to cover a wider range of parameters in order to gain an understanding of how each parameter affects the fretting damage process.

4.1 Material and specimens

The mechanical properties and chemical composition of the alloy steel of the pressure armour wire samples are given in Table 4.1 and Table 4.2 respectively. A sectional view of the specimen was given in chapter 3 (Figure 3.1).

Table 4.1 – Mechanical properties of the pressure armour wire material

Parameter	Value
UTS	1068 (MPa)
Hardness	350 (Hv 10, Max)
0.2 % Proof stress	999 (MPa)
Endurance limit (10^7) cycles	400 MPa

Table 4.2 – Chemical composition of the pressure armour wire material

Element	Heat analysis (%)	Product analysis (%)
Carbon	0.60-0.65	0.58-0.67
Manganese	0.55-0.80	0.53-0.82
Silicon	0.15-0.35	0.13-0.37
Sulphur	0.015 Max	0.015 Max
Phosphorous	0.015 Max	0.015 Max
Aluminium	0.06 Max	0.06 Max
Calcium	0.005 Max	0.005 Max
Cu+Ni+Mo+Cr	0.30 Max	0.30 Max

The Microstructure of the material is shown in Figure 4.1 and a typical surface roughness profile measurement is shown in Figure 4.2.

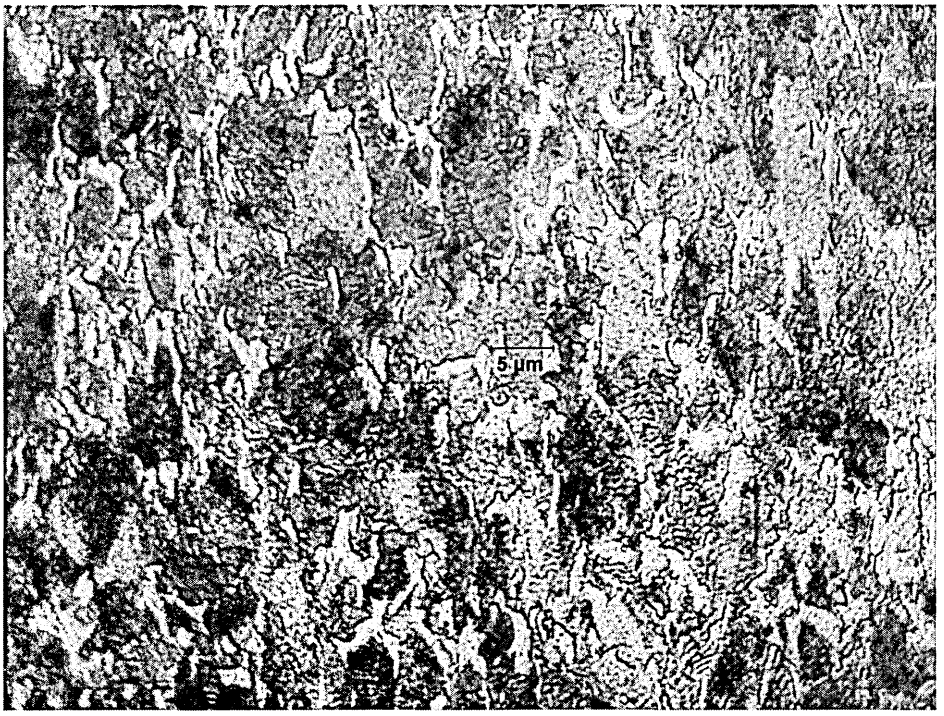

Figure 4.1 Microstructure of the pressure armour wire material

The measured average grain size of the material is 8 μm and the peak surface roughness measured in the valley of the specimen was 3 μm.

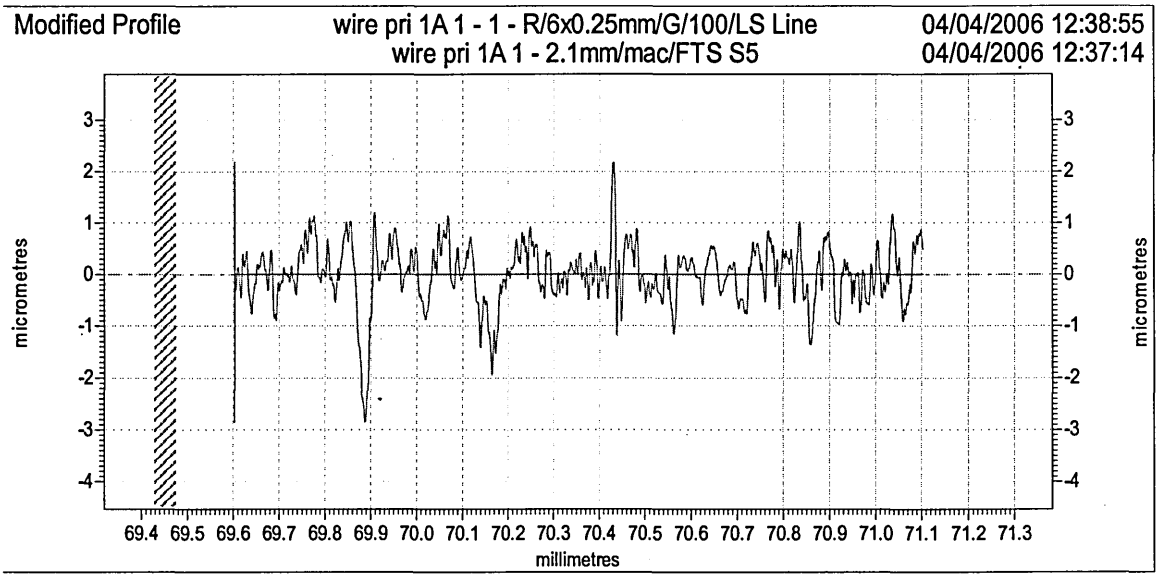

Figure 4.2 – A typical surface roughness profile of the specimen material.

4.2 – Test procedure

The salient features of the test machine were described in Chapter 3. The experimental set-up was capable of measuring the slip amplitude and the friction force. These two parameters provide vital information with regard to the fretting experiments. The plot of slip amplitude vs friction force gives the information with regard to the sliding conditions. Representative friction loops corresponding to stick, mixed slip and gross slip were presented in the literature review (2.2.1). The experimental set-up was equipped with a digital controller and a data acquisition system. The friction data was logged to the data acquisition system periodically for post processing. The built-in oscilloscope of the controller was used to display the friction loop while in operation for each fretting cycle. This facility enabled sliding condition to be monitored and controlled during operation.

The wear rate was quantified by Talysurf analysis of the surface after fretting damage. Measurements were made at three different locations along the damage scar. The depth of wear and wear profile of the scar in wire valley regions were analyzed using a Taylor Hobson Laser Form Talysurf MK1 profile-meter with ± 0.01 μm accuracy.

The damage scar on the post-test samples was examined using an optical microscope to identify scar features. The pressure armour wires were sectioned in the damage zone perpendicular to the scar (section A-A) as shown in Figure 4.3, to investigate the presence of fretting generated cracks.

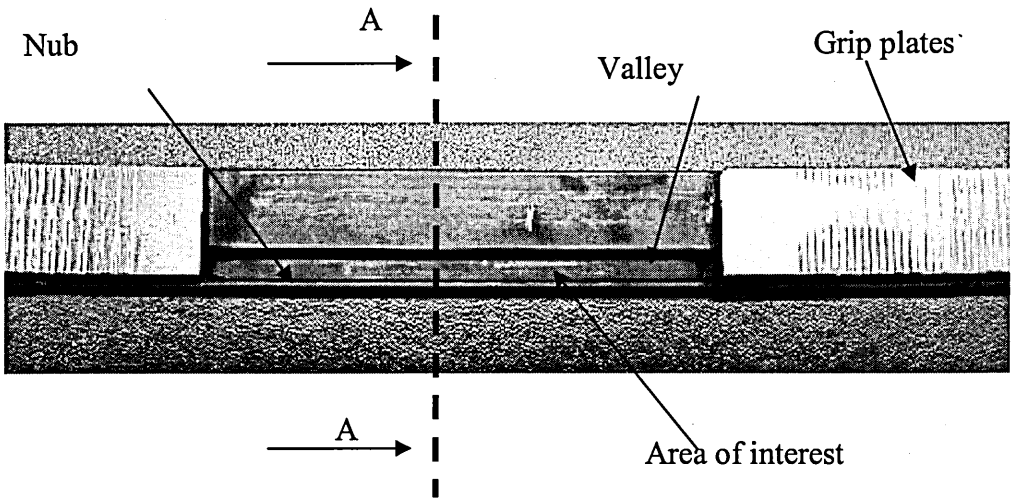

Figure 4.3 – pressure Armour Wire Specimen: Area of interest in the analysis

The sectioned samples were mounted on epoxy blocks as shown in figure 4.4, and examined using an optical microscope.

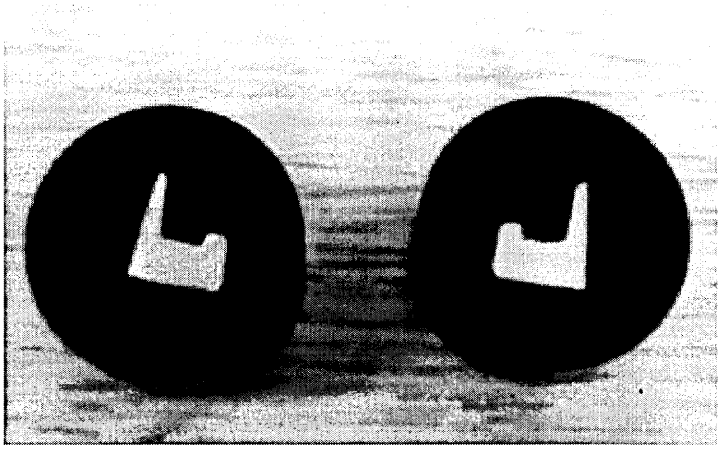

Figure 4.4 – preparation of specimens for optical microscopy analysis

4.3 Experimental programme

Three series of experiments were carried out in order to gain an understanding of individual parameters that affect the fretting damage process and to quantify the damage. A typical loading history in a test programme is shown in Figure 4.5.

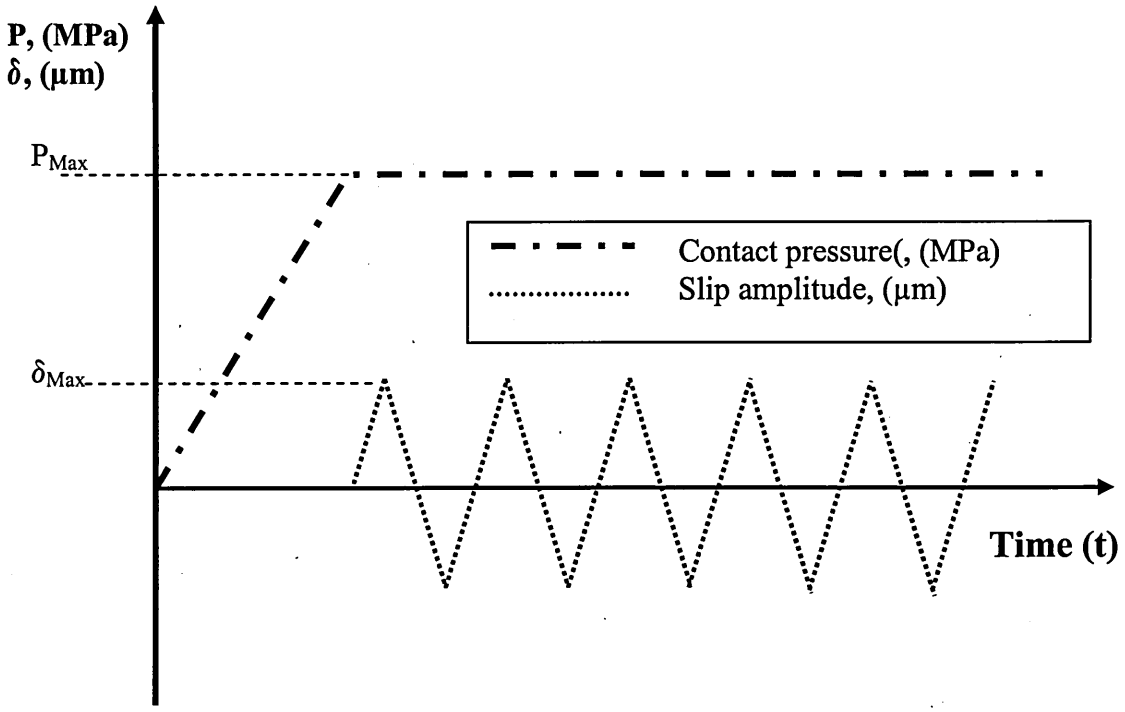

Figure 4.5 – Typical loading history in a test programme

1. Preliminary tests: (P series)

First, a series of preliminary tests were carried out for a range of nominal contact pressure and a range of slip amplitudes. A constant 145 MPa static bulk stress was applied to the specimen in all preliminary tests. The objective of this test series was to:

- understand the friction behaviour,
- determine the slip condition
- quantify the wear rate,
- analyse the type of surface damage

2. Interrupted tests (I series)

A series of interrupted tests were carried out in order to quantify the crack initiation and growth behaviour, in the mixed slip sliding region. Tests were interrupted at pre-determined number of cycles in order to ascertain the crack growth behaviour at particular nominal contact pressure.

3. Cyclic tests (C series)

A series of tests with cyclic bulk loading were carried out in order to determine the effect of bulk cyclic stress at particular nominal contact pressure. Two different damage conditions; one in mixed slip regime and the other in gross slip regime were created on a single specimen and then the specimen was subjected to cyclic loading in order to determine the reduction of fatigue strength.

4.4 Preliminary test series

A total of 15 tests were carried out in the preliminary test series: The preliminary test programme schedule is given in Table 4.3

Table 4.3 – The preliminary test programme schedule

Experiment	Nominal contact pressure (MPa), P_{Max}	Number of cycles	Slip amplitude (μm), δ_{Max}
Test P1	260	200,000	± 20
Test P2	260	190,000	± 40
Test P3	260	190,000	± 80
Test P4	200	300,000	± 27
Test P5	200	250,000	± 50
Test P6	200	300,000	± 60
Test P7	160	250,000	± 25
Test P8	160	250,000	± 30
Test P9	160	250,000	± 60
Test P10	90	250,000	± 25
Test P11	90	250,000	± 55
Test P12	90	250,000	± 80
Test P13	60	200,000	± 25
Test P14	60	250,000	± 62
Test P15	60	250,000	± 70

In the preliminary test series the nominal contact pressure ranged from 60 MPa to 260 MPa and the slip amplitude varied from 20μm to 80μm. Tests were terminated approximately after 250,000 loading cycles to investigate the surface damage. All tests were conducted at a static bulk stress of 145 MPa. For each test, the loops of friction versus slip were recorded with the number of cycles at regular intervals of time

4.41 Wear rate

The surface wear profile measurements for the preliminary test programme are shown in Figure 4.6 through Figure 4.20.

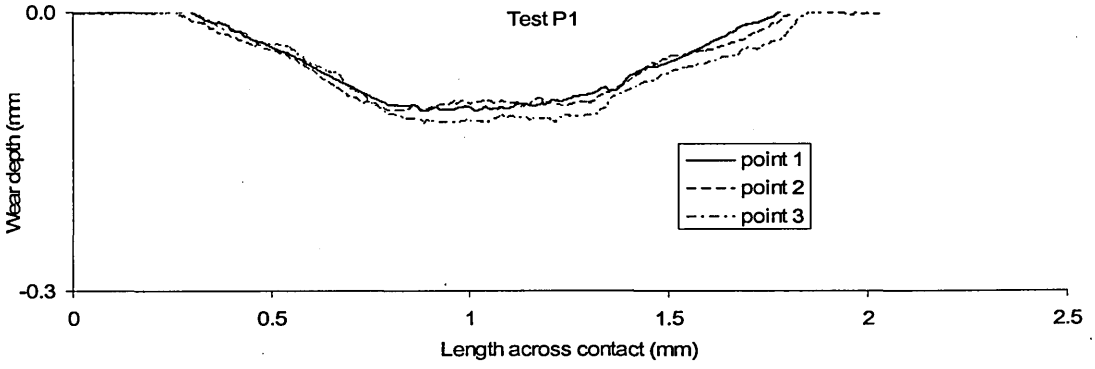

Figure 4.6 – Surface wear profile: Test P1; Nominal contact pressure – 260 MPa, Stroke – 20 μm, No of\cycles 200,000.

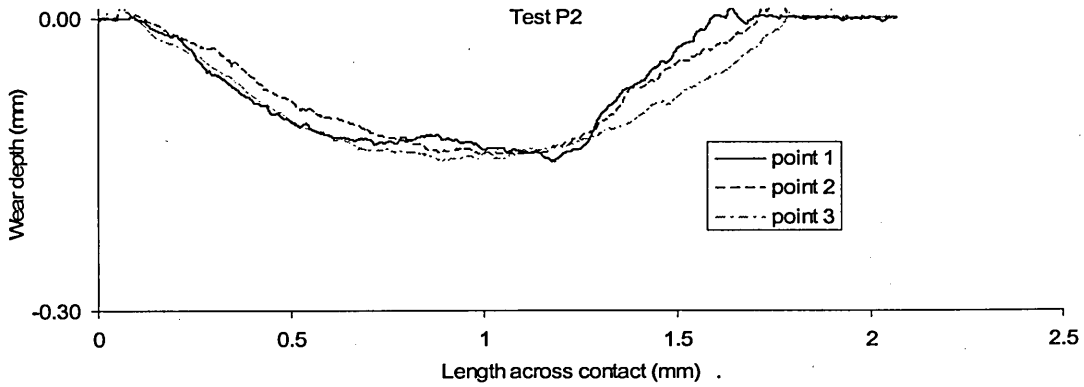

Figure 4.7 – Surface wear profile: Test P2: Nominal contact pressure – 260 MPa, Stroke – 40 μm, No of cycles 190,000.

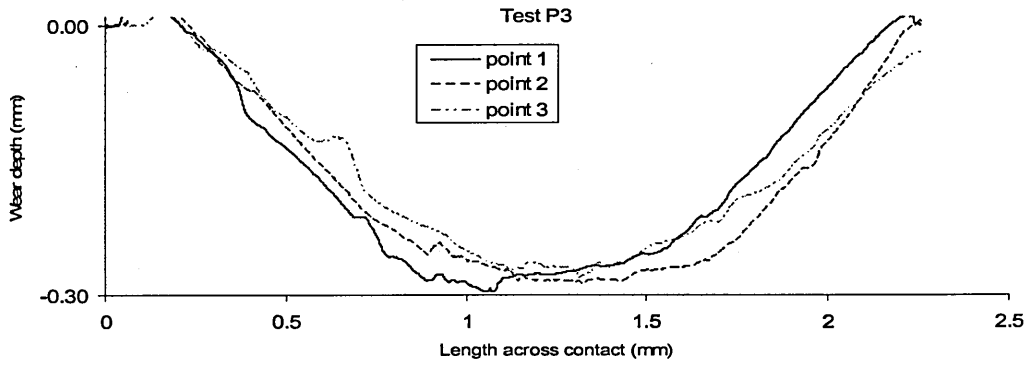

Figure 4.8 – Surface wear profile: Test P3: Nominal contact pressure – 260 MPa, Stroke – 80 μm, No of cycles 190,000.

The surface wear scars at 260 MPa nominal contact pressure for three different slip amplitudes, are shown in Figure 4.6 -Figure 4.8. Each wear scar was measured at three different places (point 1 - point 3 on graph) and a uniform wear pattern across the contact could be observed. The wear depth increased with the increase of slip amplitude. The maximum depth observed at 260 MPa contact pressure was 0.3 mm.

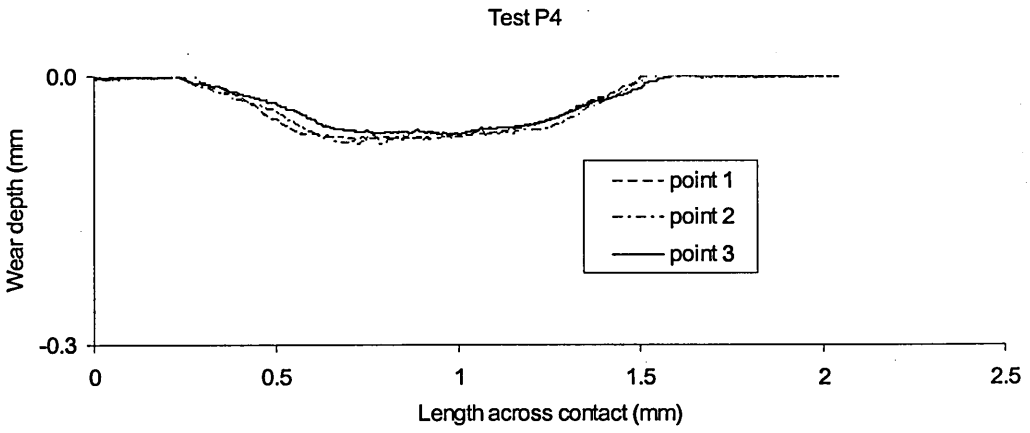

Figure 4.9 – Surface wears profile: Test P4 : Nominal contact pressure – 200 MPa, Stroke – 27 μm, No of cycles 300,000.

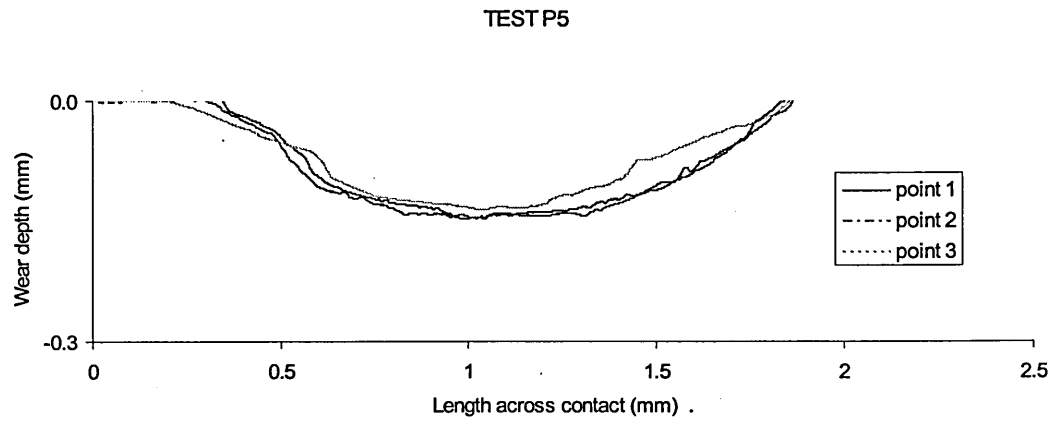

Figure 4.10 – Surface wear profile: Test P5; Nominal contact pressure – 200 MPa, Stroke – 50 μm, No of cycles 250,000.

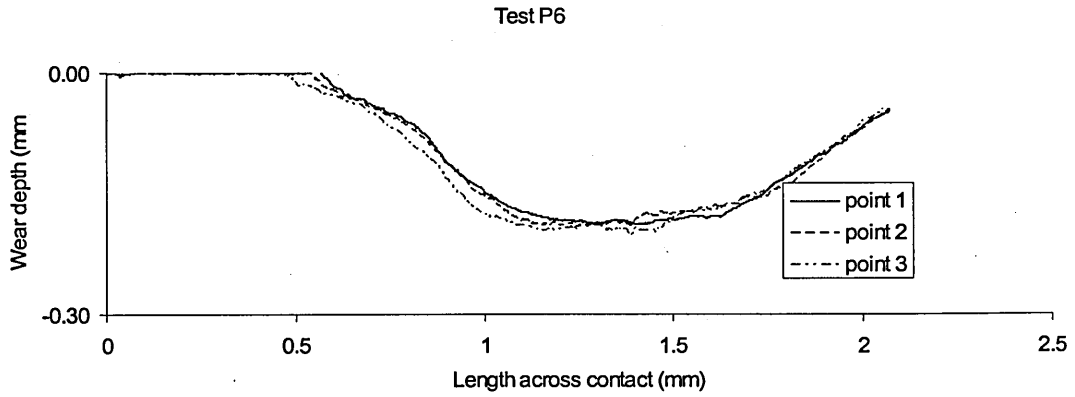

Figure 4.11 – Surface wear profile: Test P6; Nominal contact pressure – 200 MPa, Stroke – 60 μm, No of cycles 300,000.

The surface wear scars at 200 MPa nominal contact pressure for three different slip amplitudes, are shown in Figure 4.9 -Figure 4.11. The wear scars measured in three points confirm a uniform wear pattern across the contact. The wear depth increased with the increase of slip amplitude. A decrease of wear rate could be observed compared to that observed at 260 MPa nominal contact pressure. The maximum depth observed at 200 MPa contact pressure was 0.17 mm.

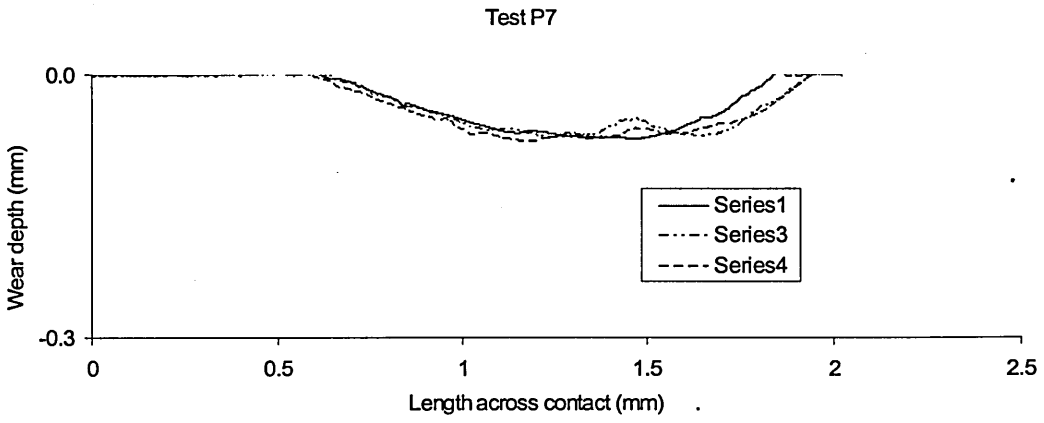

Figure 4.12 – Surface wear profile: Test P7; Nominal contact pressure –160 MPa, Stroke – 25 μm, No of cycles 250,000.

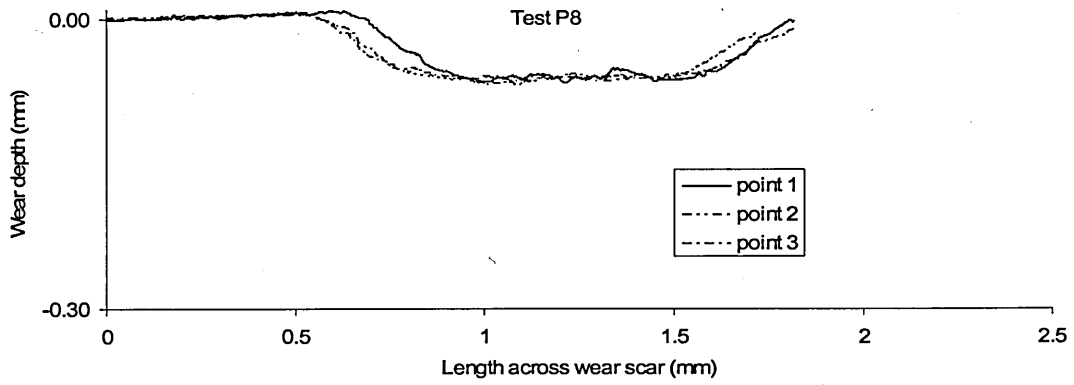

Figure 4.13 – Surface wear profile: Test P8; Nominal contact pressure –160 MPa, Stroke – 30 μm, No of cycles 250,000.

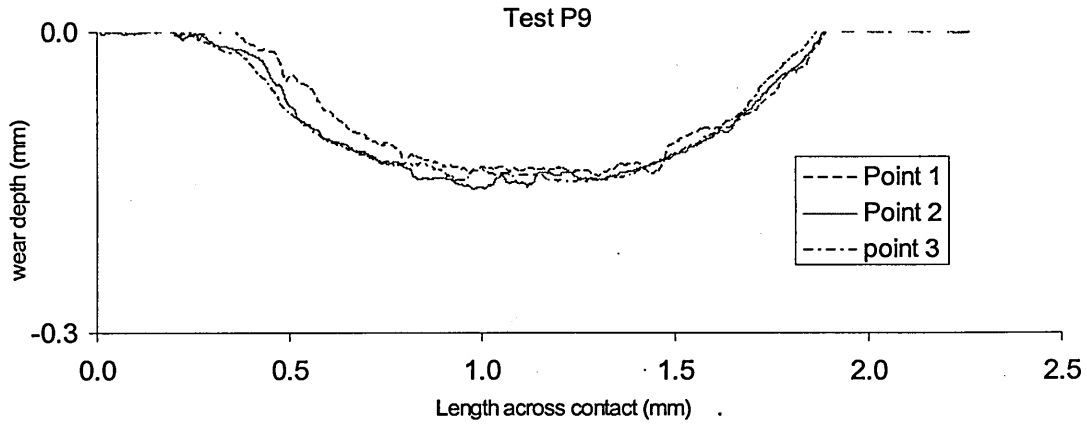

Figure 4.14 – Surface wear profile: Test P9; Nominal contact pressure –160 MPa, Stroke – 60 μm, No of cycles 250,000.

The surface wear scars at 160 MPa nominal contact pressure for three different slip amplitudes are shown in Figure 4.12 -Figure 4.14. The wear scar measured at three points again confirms a uniform wear pattern across the contact. The wear depth increased with the increase of slip amplitude.

A decrease of wear rate could be observed compared to that observed at 200 MPa nominal contact pressure. The maximum depth observed at 160 MPa contact pressure was 0.15 mm.

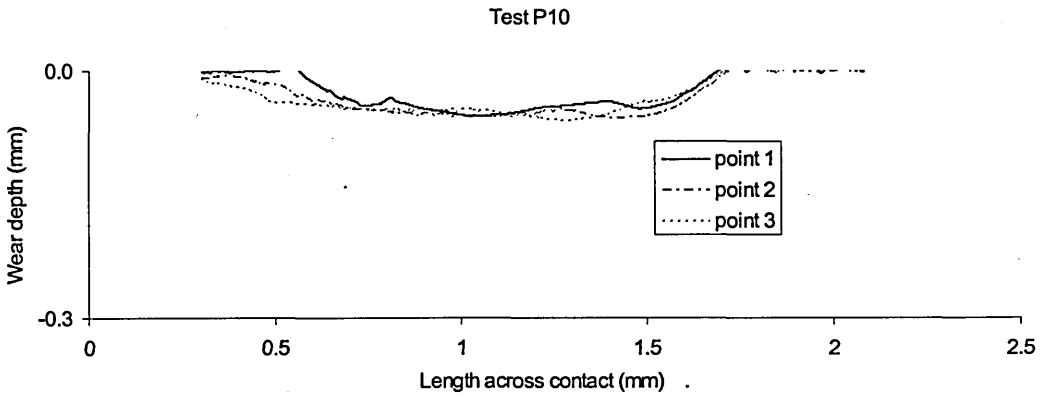

Figure 4.15 – Surface wear profile: Test P10; Nominal contact pressure –90 MPa, Stroke – 25 μm, No of cycles 250,000.

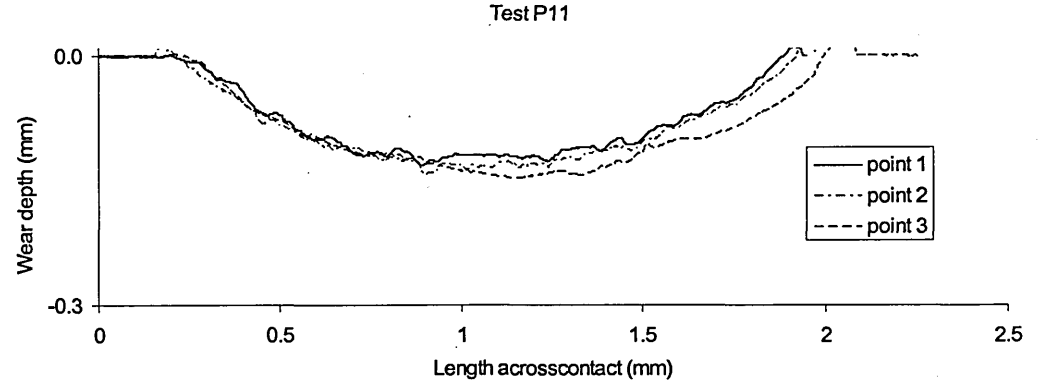

Figure 4.16 – Surface wear profile: Test P11 ; Nominal contact pressure –90 MPa, Stroke – 55 μm, No of cycles 250,000.

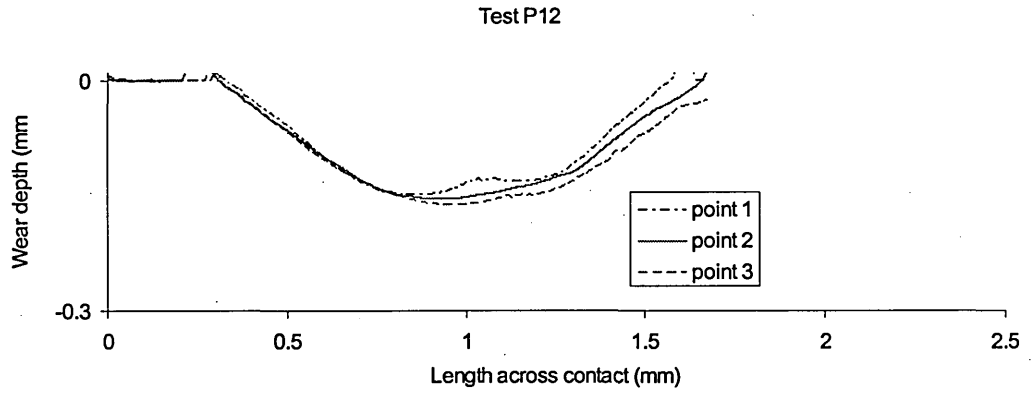

Figure 4.17 – Surface wear profile: Test P12; Nominal contact pressure –90 MPa, Stroke – 80 μm, No of cycles 250,000.

The surface wear scar at 90 MPa nominal contact pressure for three different slip amplitudes, is shown in Figure 4.15 -Figure 4.17. As before, the wear scar measured at three points confirms a uniform wear pattern across the contact. The wear depth increased with the increase of slip amplitude. A decrease of wear rate could be observed compared to that observed at 100 MPa nominal contact pressure. The maximum depth observed at 90 MPa contact pressure was 0.18 mm.

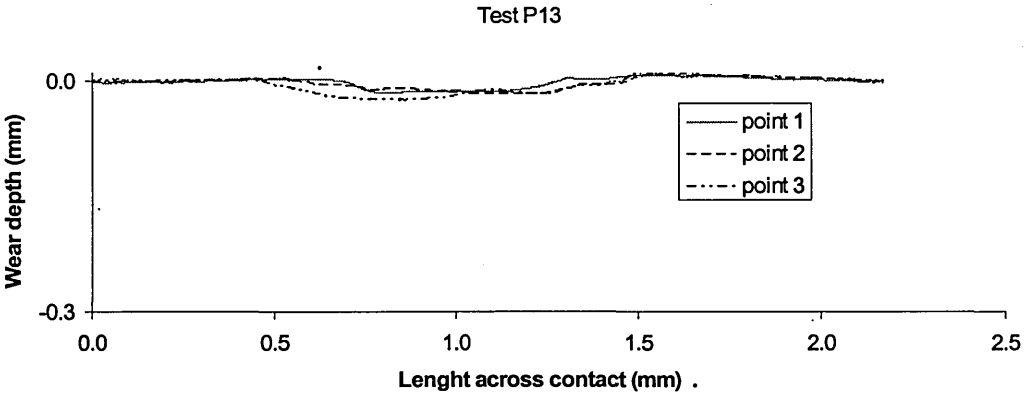

Figure 4.18 – Surface wear profile: Test P13; Nominal contact pressure –60 MPa, Stroke – 25 μm, No of cycles 200,000.

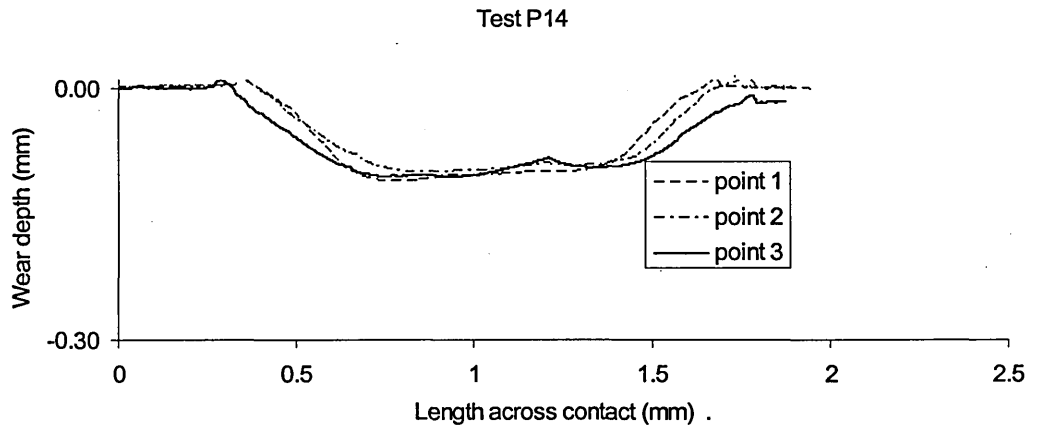

Figure 4.19 – Surface wear profile: Test P14; Nominal contact pressure – 60 MPa, Stroke – 62 μm, No of cycles 250,000.

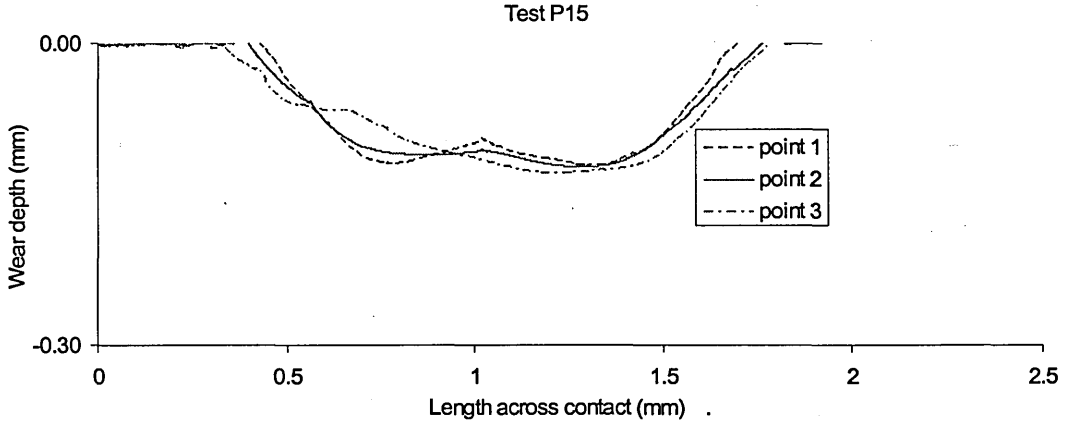

Figure 4.20 – Surface wear profile: Test P15; Nominal contact pressure – 60 MPa, Stroke – 25 μm, No of cycles 250,000.

Table 4. 4 - Summary of wear depth results for preliminary test series

Experiment	Nominal contact pressure (MPa)	Slip amplitude (Mm)	Maximum wear depth (Mm)	Number of cycles
Test PI	260	20	110	200,000
Test P2	260	40	150	190,000
Test P3	260	80	300	190,000
Test P4	200	27	80	300,000
Test P5	200	50	140	250,000
Test P6	200	60	170	300,000
Test P7	160	25	70	250,000
Test P8	160	30	80	250,000
Test P9	160	60	150	250,000
Test P10	90	25	60	250,000
Test PI 1	90	55	130	250,000
Test P 12	90	80	180	250,000
Test P I3	60	25	30	200,000
Test P14	60	62	120	250,000
Test P I5	60	70	140	250,000

The surface wear scars at 60 MPa nominal contact pressure for three different slip amplitudes, are shown in Figure 4.18 -Figure 4.20. Similar trends in wear pattern and wear depths were observed.

The lowest wear rate was observed in this series of experiments at 60 MPa. The preliminary series of tests clearly indicate that a direct relationship exists between the wear rate and contact pressure and the slip amplitude. The observations are summarised in Table.4.4. Details of these results have been discussed in chapter 6.

4.4.2 Friction data and slip condition

Frictional data was logged into a database periodically during experiments, a total of 36 points were logged into the database for each complete fretting cycle. This data was processed in order to understand the variation of the friction force and sliding condition. The traction coefficient was calculated as the ratio of the global friction range, ($\Delta F_{max,}$) and twice of the applied normal load (2F).

For each of the preliminary tests, the variation of the traction coefficient and a representative friction loop in the stabilised condition are shown in Figure 4.21 through Figure 4.35.

The variation of the friction force at 260 MPa nominal contact pressure for the three different slip amplitude is shown in Figure 4.21 , Figure 4.22 and Figure 4.23. The friction loop corresponds in each figure to the sliding condition in the stabilised

state. The tests P1 and Test P2 were carried out in the mixed slip condition while the test P3 was carried out in gross slip condition.

The stabilised traction coefficients in mixed slip is in the range of 1.0 to 1.1 where as the stabilised traction coefficient in gross slip is about 1.4

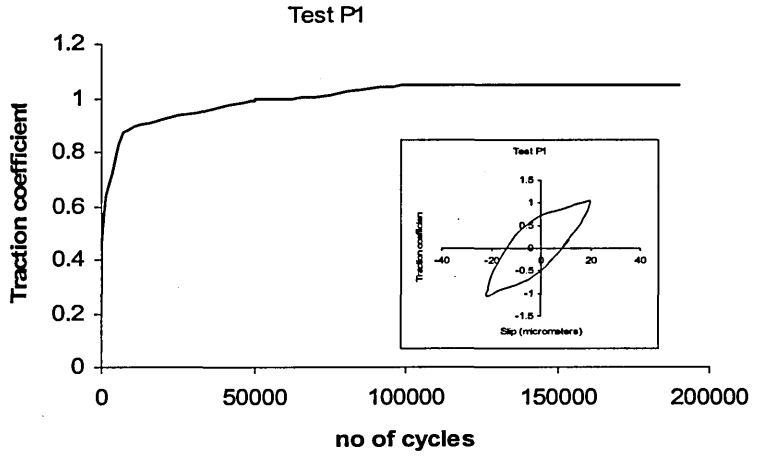

Figure 4.21 – Variation of traction coefficient and stabilised friction loop: Test P1; Nominal contact pressure – 260 MPa, Stroke – 20 μm, No of cycles 200,000.

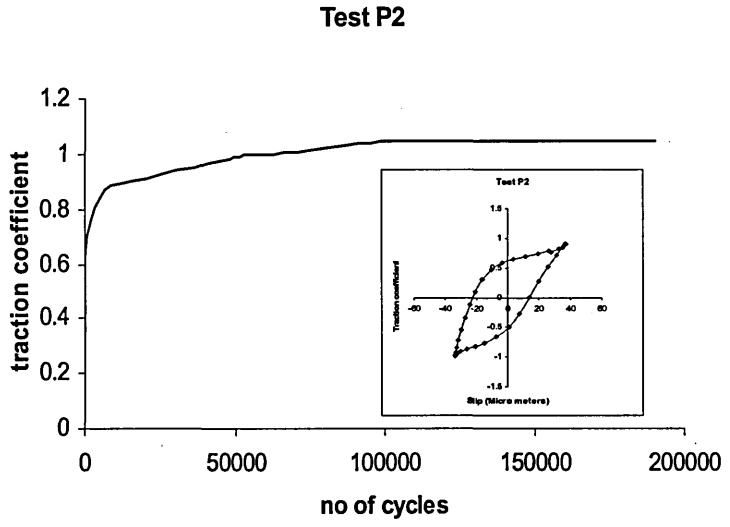

Figure 4.22 – Variation of traction coefficient and a stabilised friction loop: Test P2; Nominal contact pressure – 260 MPa, Stroke– 40 μm, No of cycles 190,000.

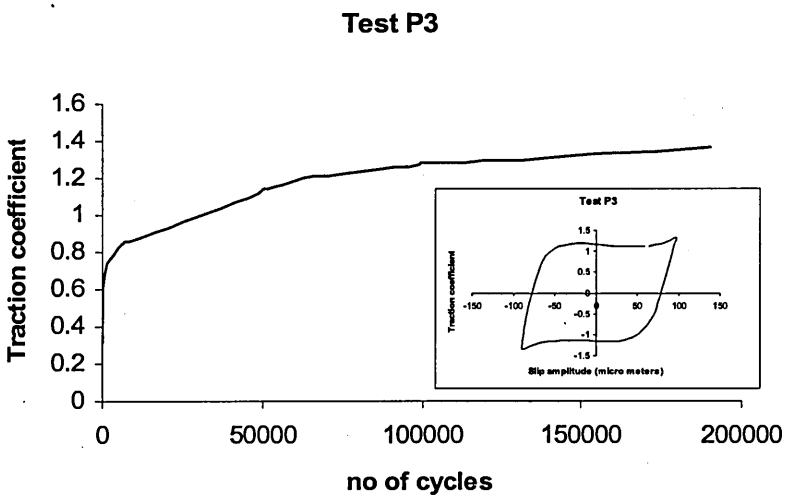

Figure 4.23 – Variation of traction coefficient and a stabilised friction loop : Test P3; Nominal contact pressure – 260 MPa, Stroke – 80 μm, No of cycles 190,000.

The variation of the traction coefficient at 200 MPa nominal contact pressure for three different slip amplitudes are shown in Figure 4.24, Figure 4.25 and Figure 4.26. Test P4 was carried out in the mixed slip condition while the tests P5 and P6 were carried out in the gross slip condition. The stabilised traction coefficients in the mixed slip condition were 0.9 whereas the stabilised traction coefficient in the gross slip is in the range of 1.2 to 1.6.

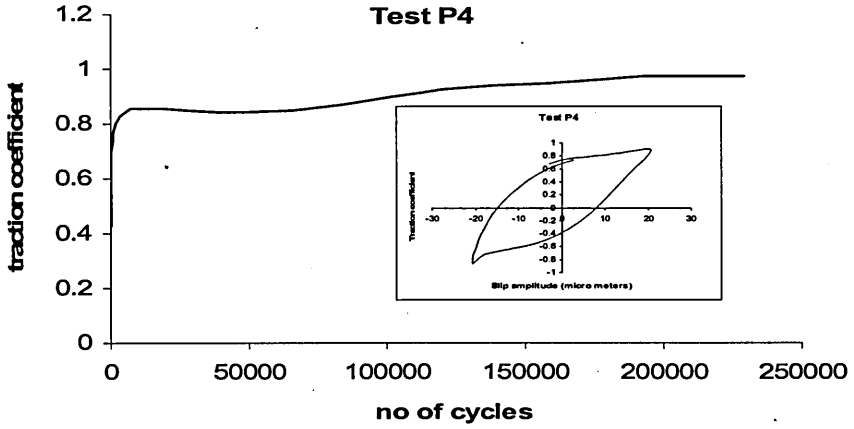

Figure 4.24 – Variation of traction coefficient and a stabilised friction loop : Test P4; Nominal contact pressure – 200 MPa, Stroke – 27 μm, No of cycles 300,000.

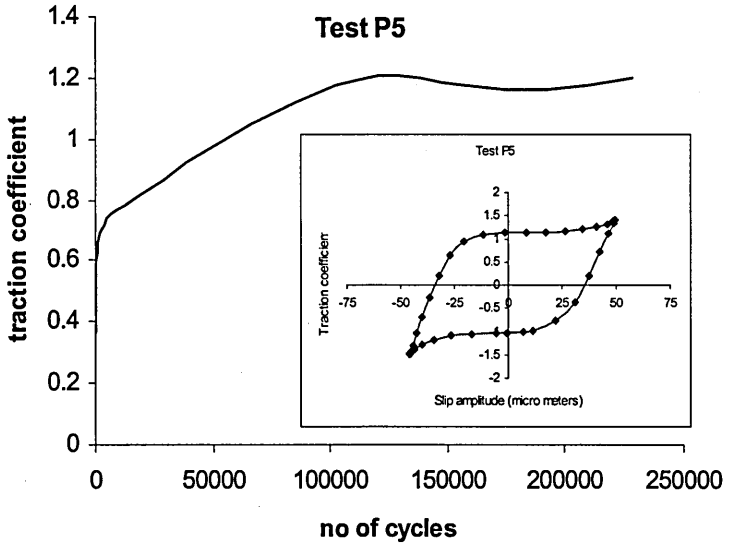

Figure 4.25 – Variation of traction coefficient and a stabilised friction loop : Test P5; Nominal contact pressure – 200 MPa, Stroke – 50 μm, No of cycles 250,000.

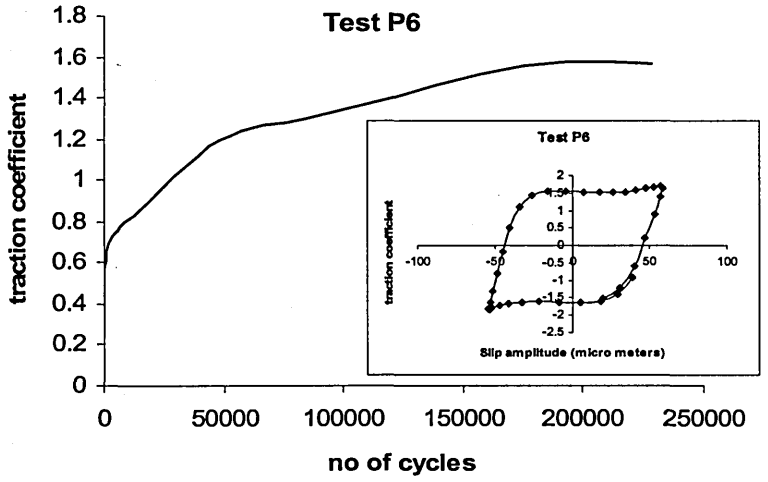

Figure 4.26 – Variation of traction coefficient and a stabilised friction loop : Test P6; Nominal contact pressure – 200 MPa, Stroke – 60 μm, No of\cycles 300,000.

The variation of the traction coefficient at 160 MPa nominal contact pressure for three different slip amplitudes is shown in Figure 4.27, Figure 4.28 and Figure 4.29. Test P7 and P8 were carried out in the mixed slip condition and test P9 was carried out in gross slip condition. The stabilised traction coefficients in the mixed slip condition varied in the range 0.9 to 1.0 whereas the stabilised traction coefficient in gross slip was stabilised at around 1.3.

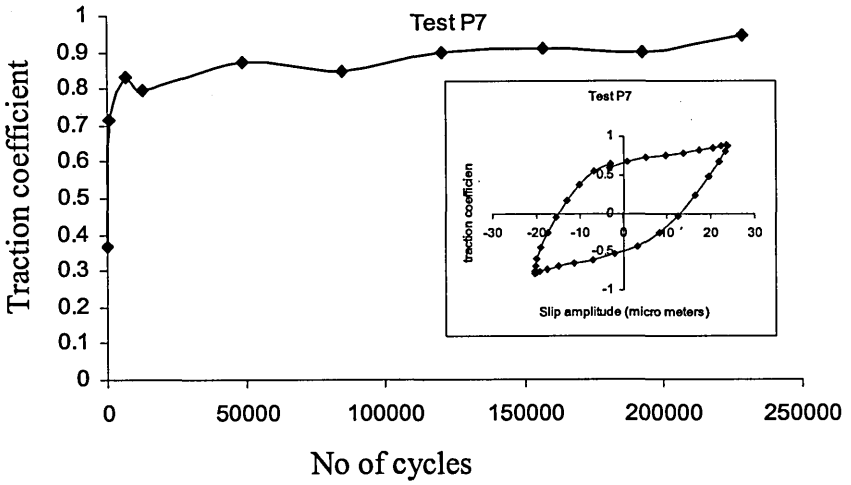

Figure 4.27 – Variation of traction coefficient and a stabilised friction loop : Test P7; Nominal contact pressure –160 MPa, Stroke – 25 μm, No of cycles 250,000.

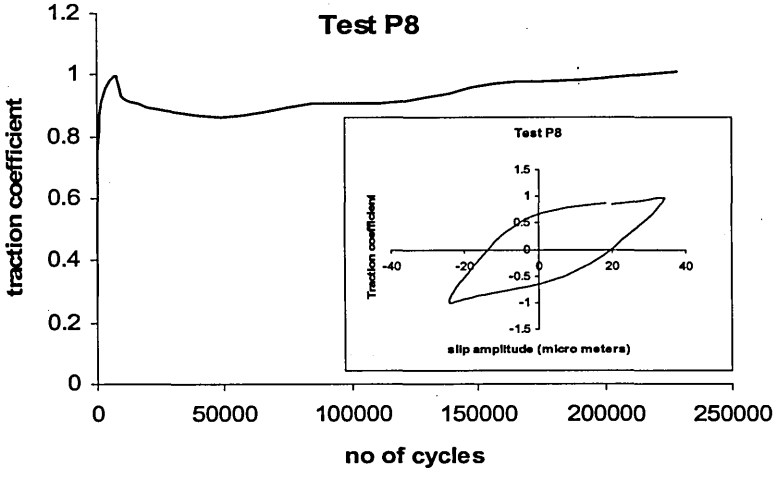

Figure 4.28 – Variation of traction coefficient and a stabilised friction loop : Test P8; Nominal contact pressure –160 MPa, Stroke – 30 μm, No of cycles 250,000.

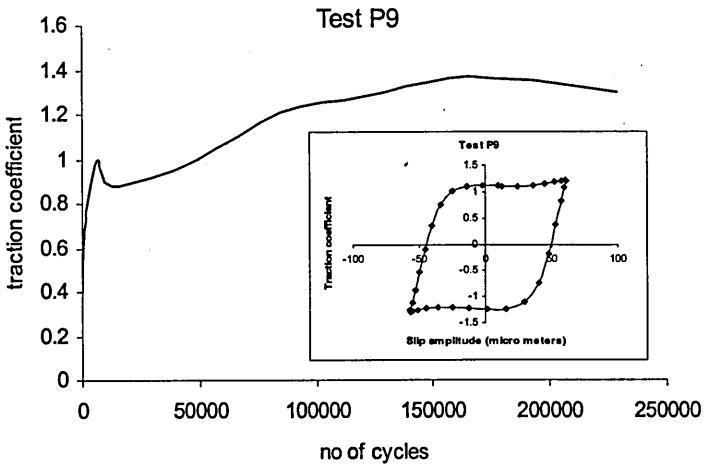

Figure 4.29 – Variation of traction coefficient and a stabilised friction loop : Test P9; Nominal contact pressure –160 MPa, Stroke – 60 μm, No of cycles 250,000.

The variation of the traction coefficient at 90 MPa nominal contact pressure for three different slip amplitudes is shown in Figure 4.30, Figure 4.31 and Figure 4.32. The test P10 was carried out in the mixed slip and Tests P11 and P12 were carried out in the gross slip condition. The stabilised traction coefficient in the mixed slip condition was 0.9 whereas in the gross slip condition it was in the range of 1.2 to1.4.

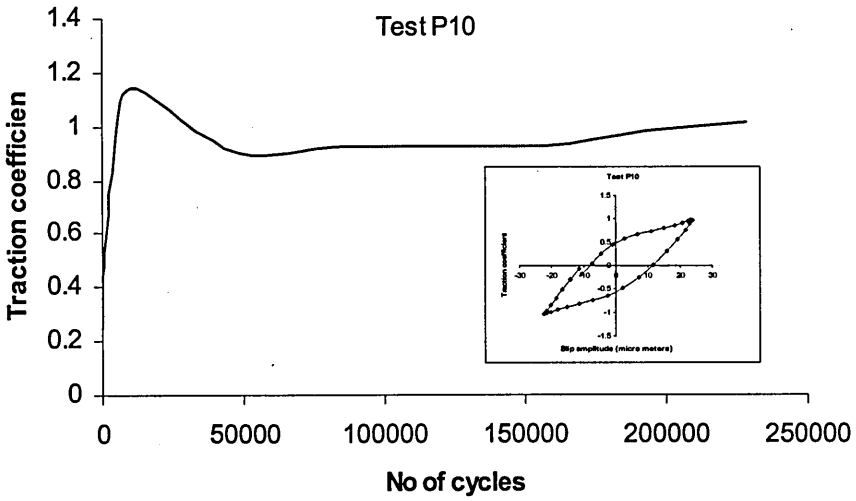

Figure 4.30 – Variation of traction coefficient and a stabilised friction loop : Test P10; Nominal contact pressure –90 MPa, Stroke – 25 μm, No of cycles 250,000.

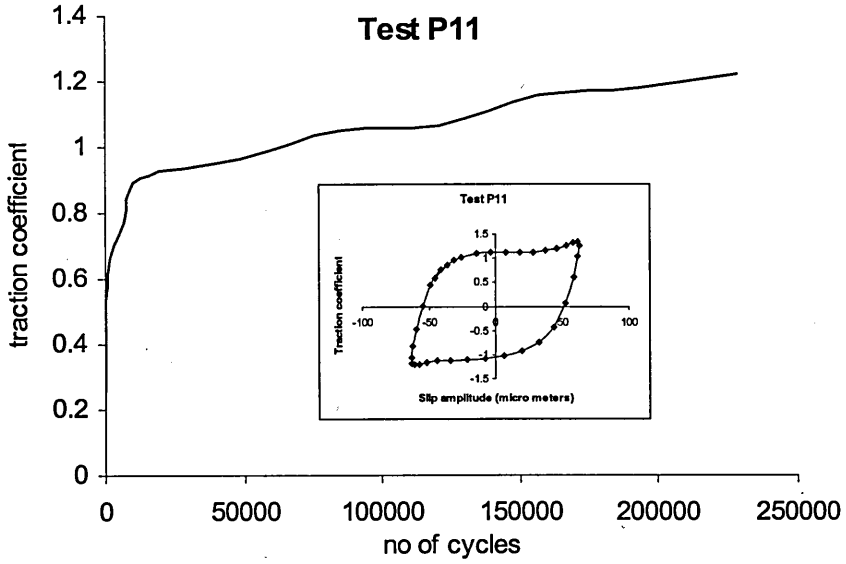

Figure 4.31 – Variation of traction coefficient and a stabilised friction loop : Test P11; Nominal contact pressure –90 MPa, Stroke – 55 μm, No of cycles 250,000.

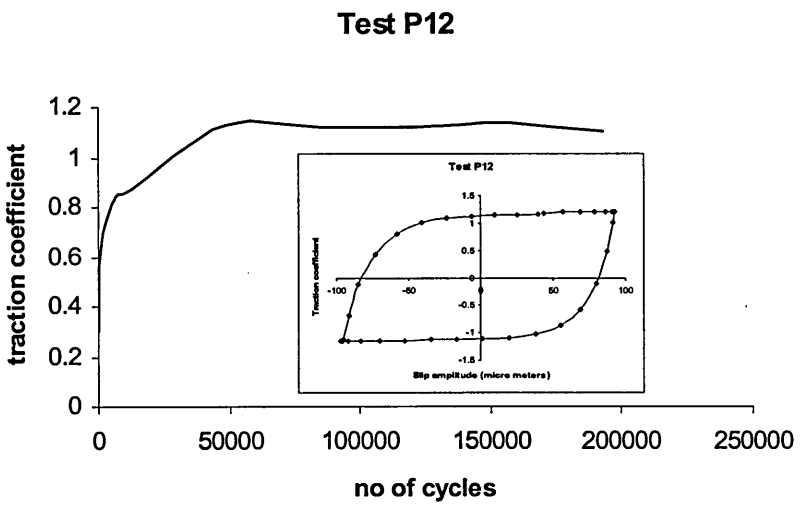

Figure 4.32 – Variation of traction coefficient and a stabilised friction loop : Test P12; Nominal contact pressure –90 MPa, Stroke – 80 μm, No of cycles 250,000.

Variation of the friction force at 60 MPa nominal contact pressure for three different slip amplitudes is shown in Figure 4.33, Figure 4.34 and Figure 4.35. Test P13 was carried out in the mixed slip condition and Test P14 and P15 were carried out in the gross slip condition.

The stabilised traction coefficient in the mixed slip condition was around 0.7 whereas in the gross slip condition it stabilised at around 1.1 to 1.3.

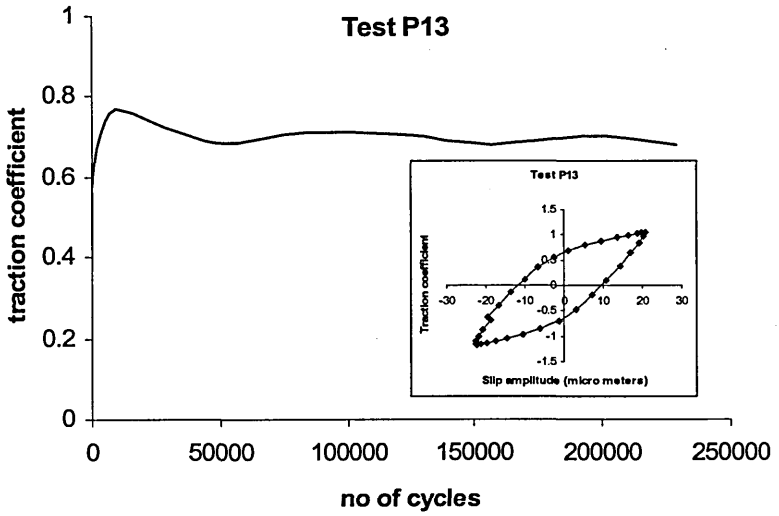

Figure 4.33 – Variation of traction coefficient and a stabilised friction loop : Test P13; Nominal contact pressure –60 MPa, Stroke – 25 μm, No of cycles 200,000.

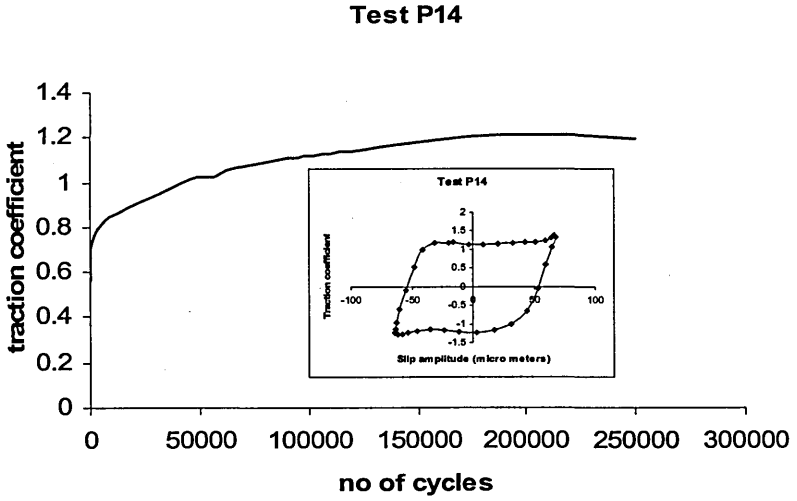

Figure 4.34 – Variation of traction coefficient and a stabilised friction loop : Test P14; Nominal contact pressure – 60 MPa, Stroke – 62 μm, No of cycles 250,000.

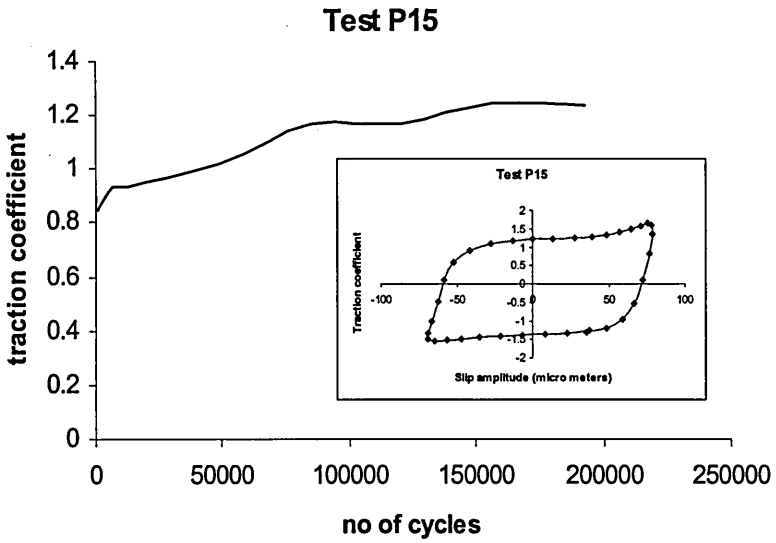

Figure 4.35 – Variation of traction coefficient and a stabilised friction loop : Test P15; Nominal contact pressure – 60 MPa, Stroke – 25 μm, No of cycles 250,000.

The frictional data for the P series is summarised in Table 4.5 and these results are discussed in detail in Chapter 6.2, Section 6.2.

Table 4.5 – Summary of stabilised traction coefficients for preliminary test series

Experiment	Nominal contact pressure MPa	Stroke amplitude (μm)	Stabilised traction coefficient
Test P1	260	20	1.0
Test P2	260	40	1.1
Test P3	260	80	1.3
Test P4	200	27	1.0
Test P5	200	50	1.2
Test P6	200	60	1.3
Test P7	160	25	0.9
Test P8	160	30	1.0
Test P9	160	60	1.36
Test P10	90	25	0.94
Test P11	90	55	1.17
Test P12	90	80	1.2
Test P13	60	25	0.7
Test P14	60	62	1.14
Test P15	60	70	1.32

4.43 Damage observations

Under certain loading conditions, two cracks could be observed on either side of the contact. The damage is presented as the damage in the left corner and the right corner separately. The damage area referred as left and right corner in the following microscopic images is schematically represented in Figure 4.36.

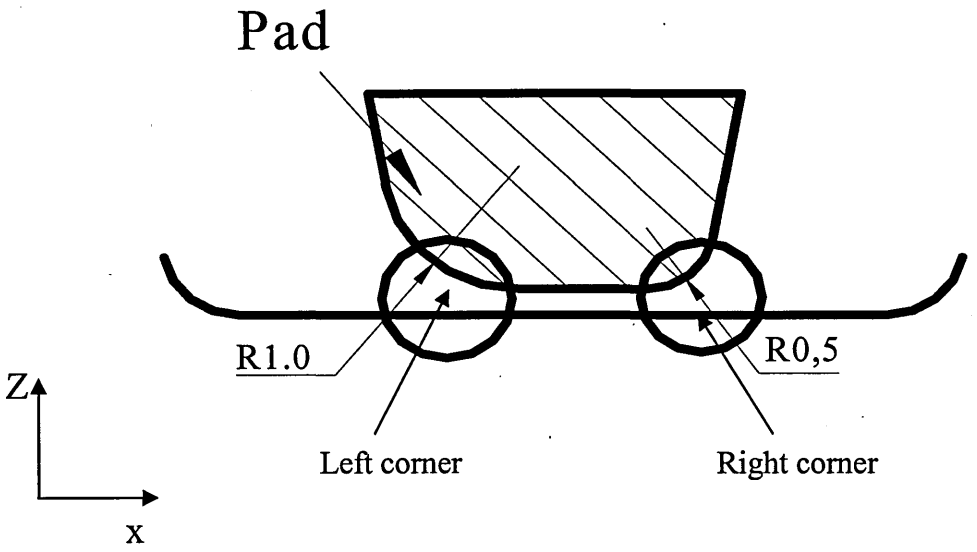

Figure 4.36 – Designation of the left and right corner in the damage zone

The damaged area in the specimen (valley of the contact) that has been in contact with the edge of the pad with higher radius (R =1 mm) is referred as the left corner and the area that has been in contact with the edge with radius (R = 0.5 mm) is referred as the right corner.

The damage observed at 260 MPa contact pressure for 200 000 cycles at 20 μm, 40 μm and 80 μm slip amplitudes is shown in figure 4.37 through 4.39. This was the highest nominal contact pressure at which the tests were carried out in the experimental programme.

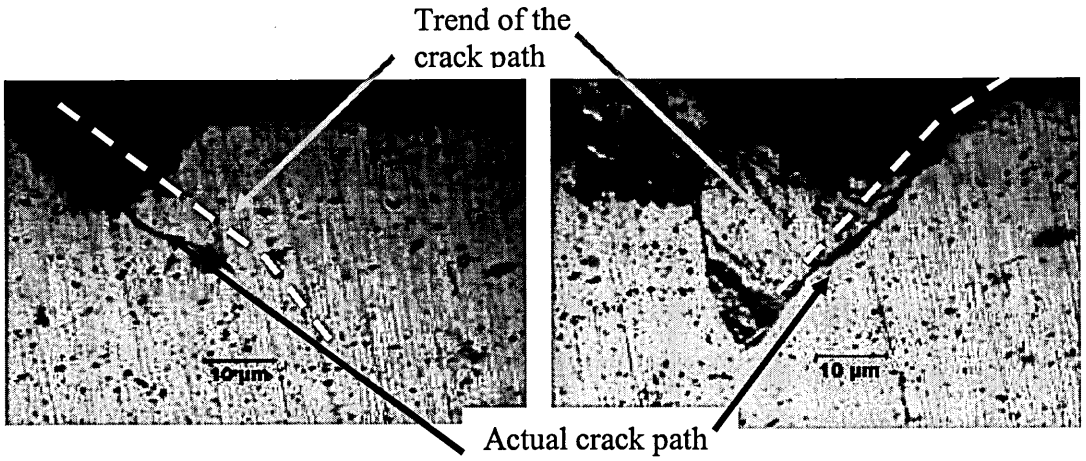

(a) (b)

Figure 4.37 -Damage observed in (a) left and (b) right corner for test P1; Nominal contact pressure – 260 MPa, Stroke – 20 μm, No of cycles 200,000.

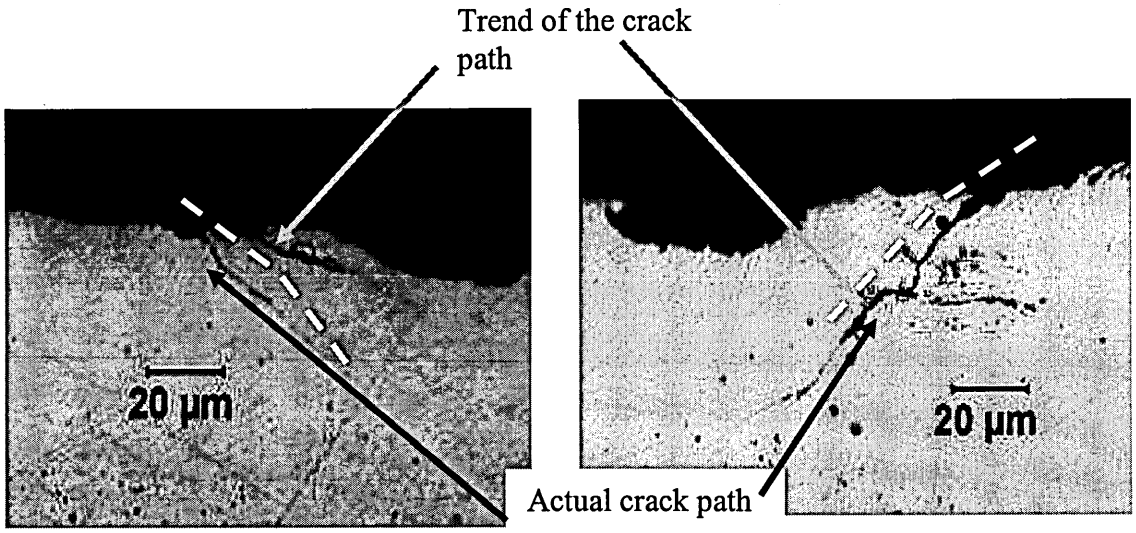

Figure 4.38 - Damage observed in left and right corner for test P2 Nominal contact pressure – 260 MPa, Stroke – 40 μm, No of\cycles 190,000.

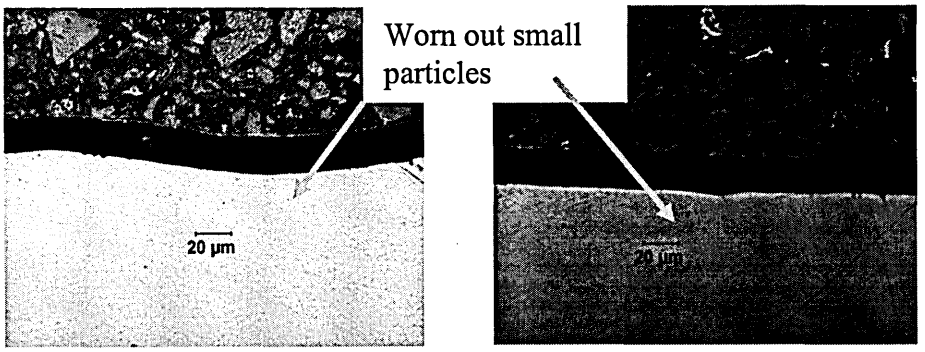

(a) (b)

Figure 4.39 - Damage observed in left and right corner for test P3 Nominal contact pressure – 260 MPa, Stroke – 80 μm, No of cycles 190,000.

Two cracks inclined to the surface could be observed for test P1 and test P2. Cracks were formed in the edge of contact. Further analysis shows that the initiation angle of the cracks in both cases is almost the same in the left and right corners and that after propagating about 10 μm to 20 μm. The observed trends of the cracks change as highlighted in Figures 4.37 and 4.38. In test P3, surface cracks could not be seen. However, delaminating type damage with a severely worn out scar could be observed for test P3.

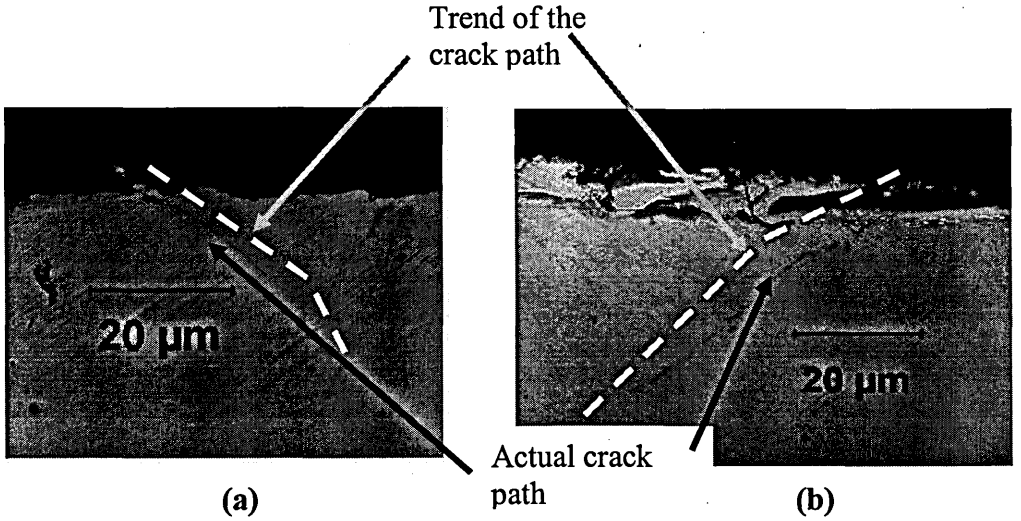

(a) (b)

Figure 4.40- Damage observed in left and right corner for test P4; Nominal contact pressure – 200 MPa, Stroke – 27 μm, No of cycles 300,000.

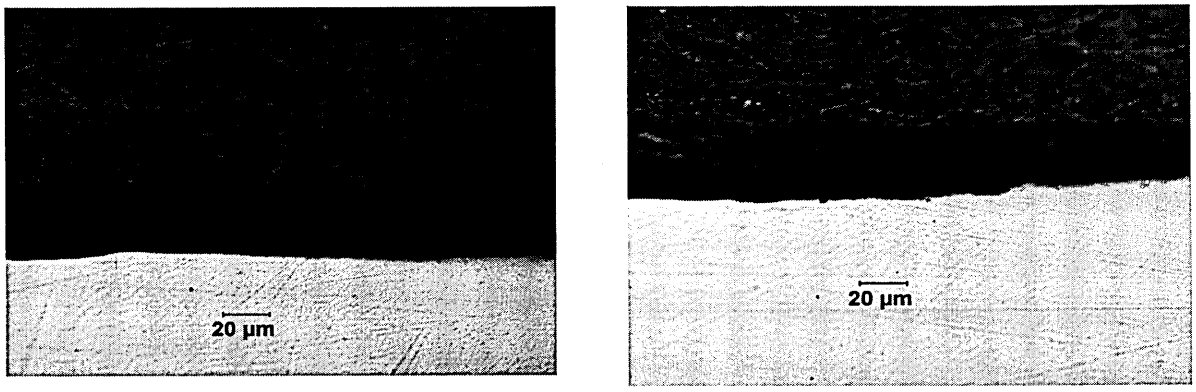

(a) (b)

Figure 4.41 - Damage observed in left and right corner for test; P5 Nominal contact pressure – 200 MPa, Stroke – 50 μm, No of cycles 250,000.

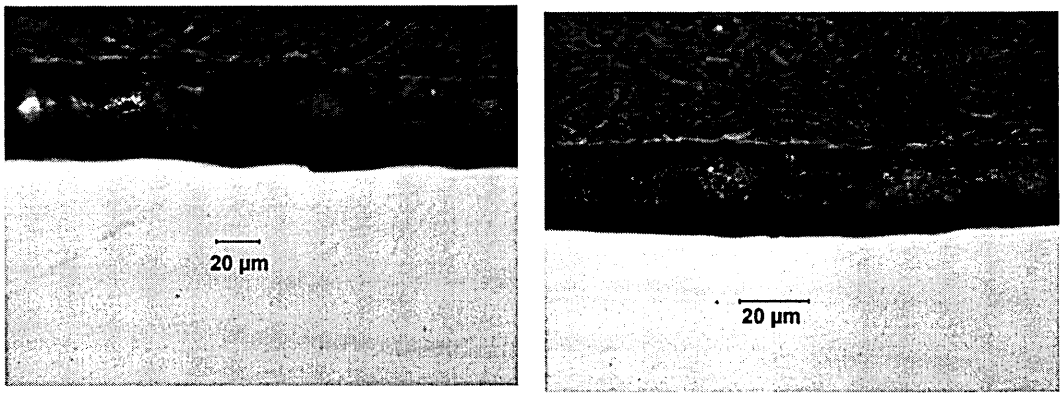

(a) (b)

Figure 4.42 - Damage observed in left and right corner for test P6; Nominal contact pressure – 200 MPa, Stroke – 60 μm, No of cycles 300,000.

The damage observed at 200 MPa nominal contact pressure for 250,000 cycles is shown in Figure 4.40 through figure 4.42.

While two cracks were observable on either side of the contact for test P4, no cracks were observable for test P5 and test P6. The cracks observed for test P4 again confirmed the typical pattern observed in test P1 and test P2 at 260 MPa contact pressure. However, the crack depth in Test P4 was less compared to the crack length observed for test P1 and test P2.

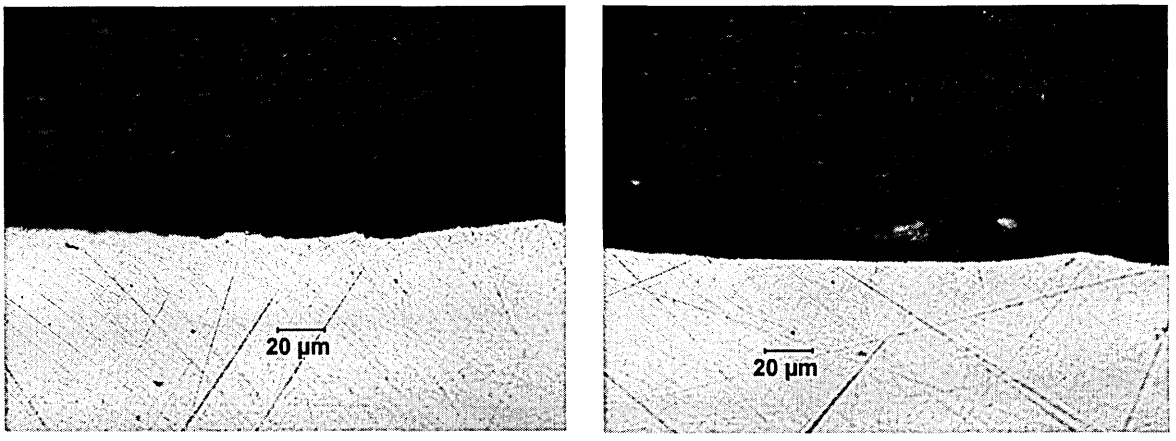

(a) (b)

Figure 4.43 - Damage observed in (a) left and (b) right corner for test P7 ; Nominal contact pressure –160 MPa, Stroke – 25 μm, No of cycles 250,000.

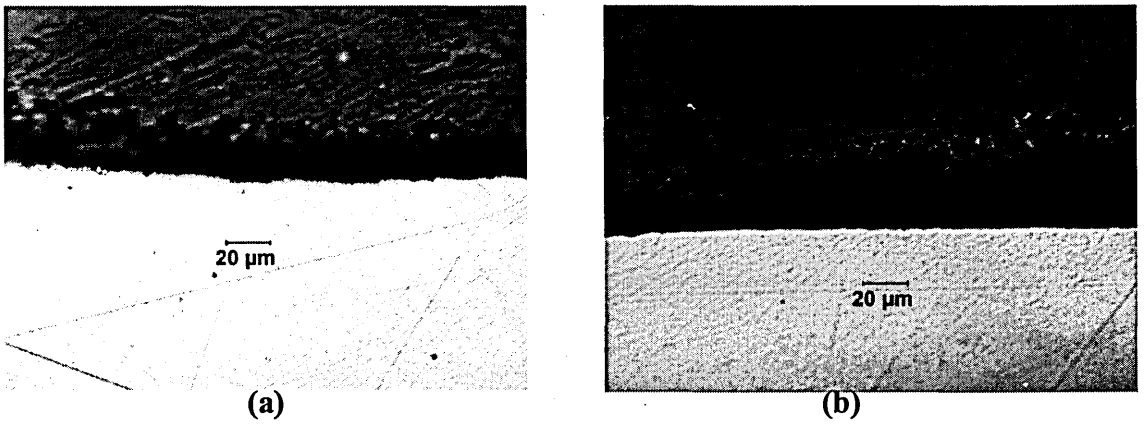

(a) (b)

Figure 4.44 - Damage observed in (a) left and (b)right corner for test P8 Nominal contact pressure –160 MPa, Stroke – 30 μm, No of cycles 250,000.

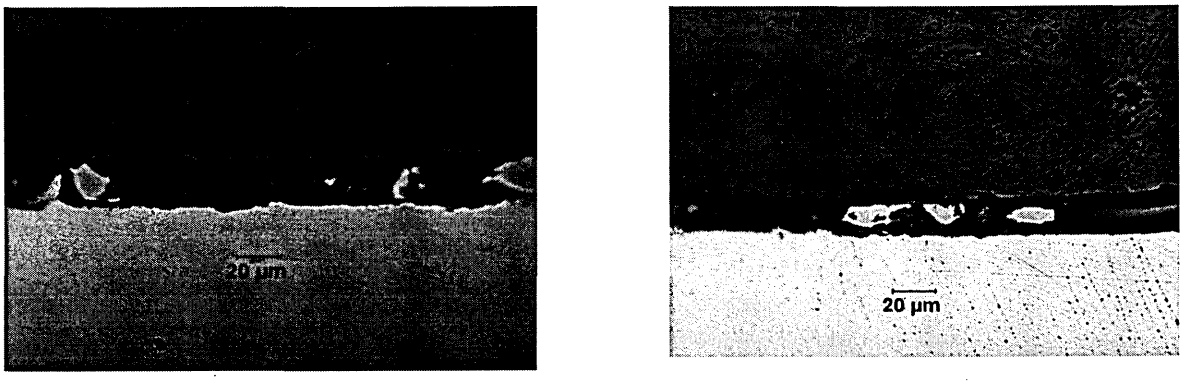

(a) (b)

Figure 4.45 – Damage observed in (a) left and (b) right corner for test P9 Nominal contact pressure –160 MPa, Stroke – 60 μm, No of cycles 250,000.

The damage observed at 160 MPa nominal contact pressure is shown in Figure 2.43 through Figure 2.45. During Tests P7, P8 and P9, no cracks could be observed. Delaminating type damage could be observed for test P9.

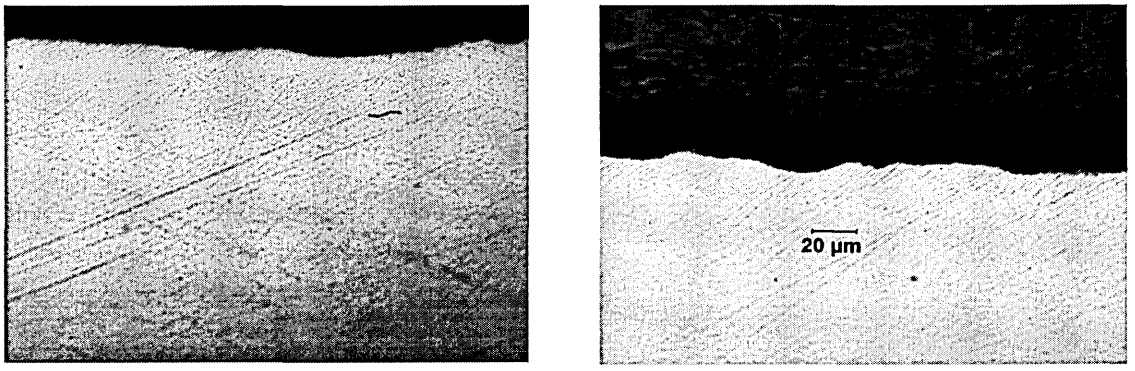

(a) (b)

Figure 4.46 – Damage observed in (a) left and (b) right corner for Test P10 Nominal contact pressure –90 MPa, Stroke – 25 μm, No of cycles 250,000.

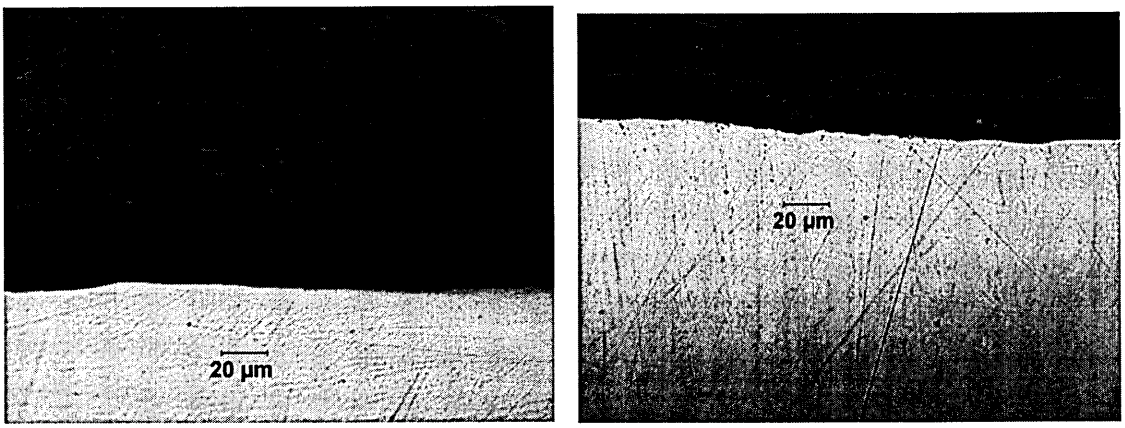

(a) (b)

Figure 4.47 – Damage observed in (a) left and (b) right corner for Test P11 Nominal contact pressure –90 MPa, Stroke – 55 μm, No of cycles 250,000.

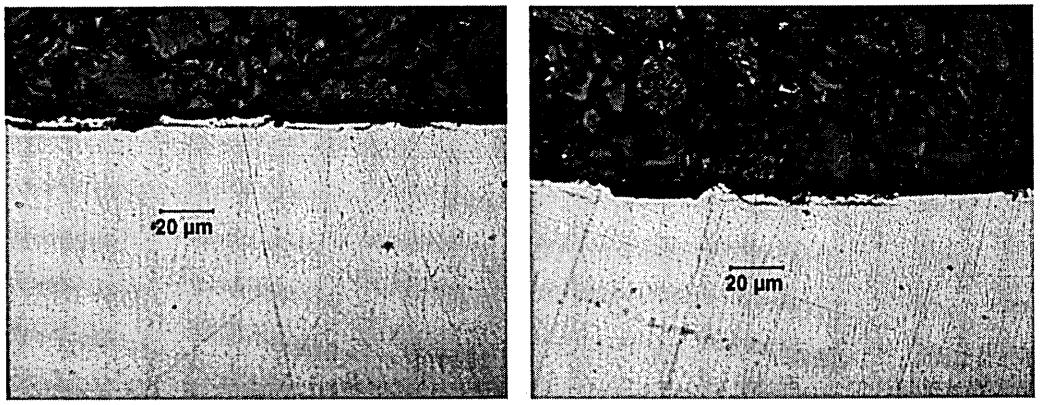

(a) (b)

Figure 4.48 – Damage observed in (a) left and (b) right corner for Test P12; Nominal contact pressure –90 MPa, Stroke – 80 μm, No of cycles 250,000.

The damage observed at 90 MPa nominal contact pressure is shown in Figure 2.46 through Figure 2.48.again during Test P10, P11 and P12, no cracks could be found.

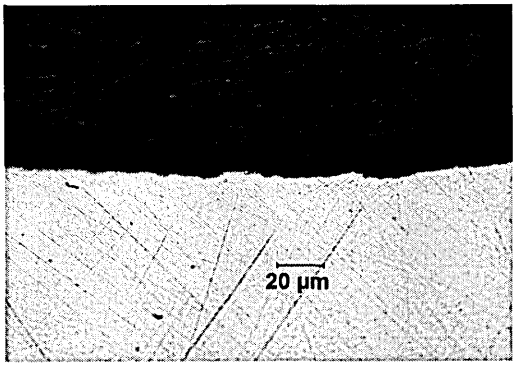

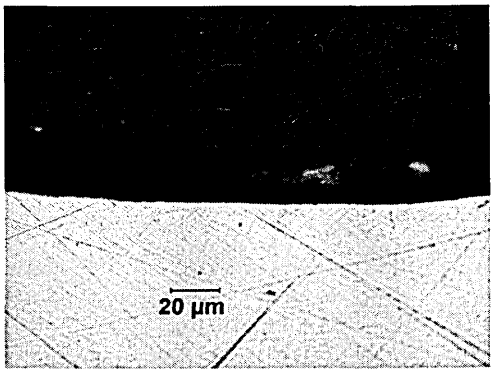

(a) (b)

Figure 4.49 – Damage observed in (a) left and (b) right corner for Test P13; Nominal contact pressure –60 MPa, Stroke – 25 μm, No of cycles 200,000.

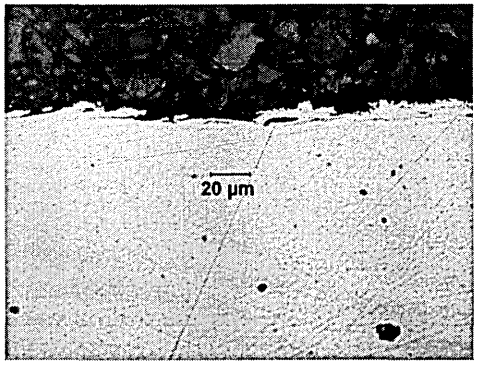

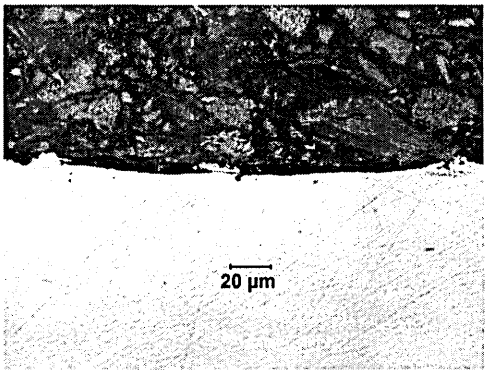

(a) (b)

Figure 4.50 – Damage observed in (a) left and (b) right corner for Test P14; Nominal contact pressure – 60 MPa, Stroke – 62 μm, No of cycles 250,000.

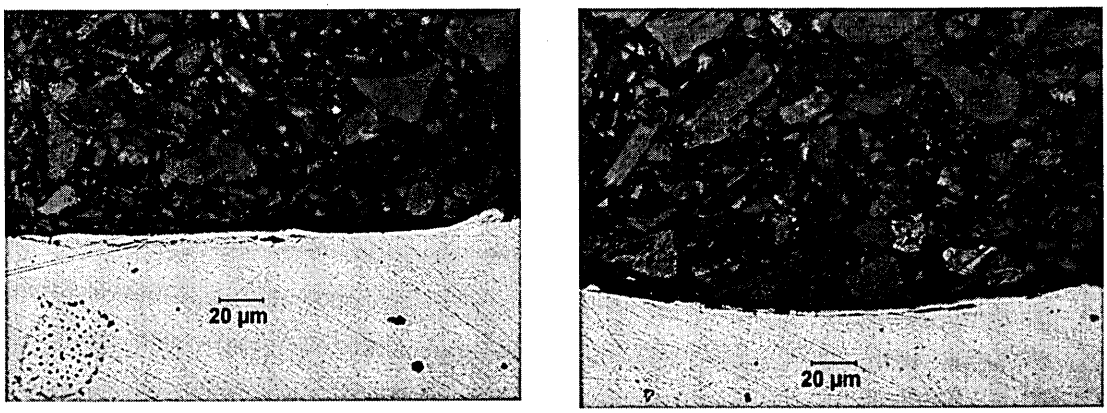

(a) (b)

Figure 4.51 – Damage observed in (a) left and (b) right corner for Test P15; Nominal contact pressure – 60 MPa, Stroke – 25 μm, No of cycles 250,000.

The damage observed at 60 MPa nominal contact pressure is shown in Figure 2.49 through Figure 2.51. During these tests again, no cracks were observed.

4.5 Interrupted tests.

A series of experiments were carried out in the stick slip boundary for various contact pressure for a range of loading cycles.

The tests were terminated after a predetermined number of cycles to observe the type of damage observable after sectioning the fretted specimen. The tests were carried out in the range of contact pressure from 70 MPa to 260 MPa and the number of cycles ranged from 600,000 cycles to 5,000,000 cycles.

Table 4.6 – Interrupted test series

Test No	Nominal pressure (MPa)	Number of cycles	Slip amplitude (μm)
Test I 1	100	600,000	21
Test I 2	140	600,000	24
Test I 3	180	600,000	32
Test I 4	160	1,600,000	30
Test I 5	120	2,000,000	28
Test I 6	70	2,000,000	18
Test I 7	110	2,800,000	22
Test I 8	90	2,800,000	20
Test I 9	145	4,100,000	30
Test I 10	80	3,000,000	18
Test I 11	80	5,000,000	17
Test I 12	260	2,000,000	36

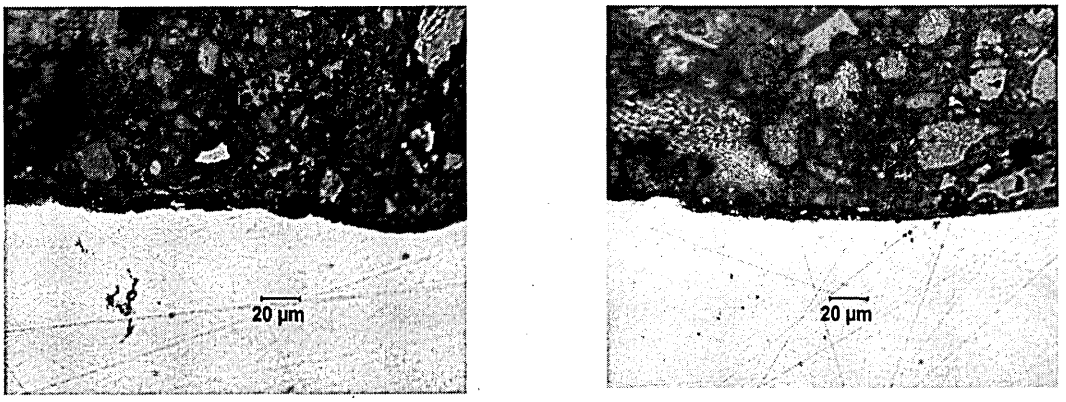

(a) (b)

Figure 4.52 – Damage observed in left and right corner for Test I 1; Nominal contact pressure – 100 MPa, Stroke – 21 μm, No of cycles 600,000.

Test I1 was carried out at 100 MPa nominal contact pressure for 600,000 cycles. The measured slip amplitude was 21 μm. No cracks could be observed on the damage surface for this test. The surface damage observed in Test I1 is shown in Figure 4.51.

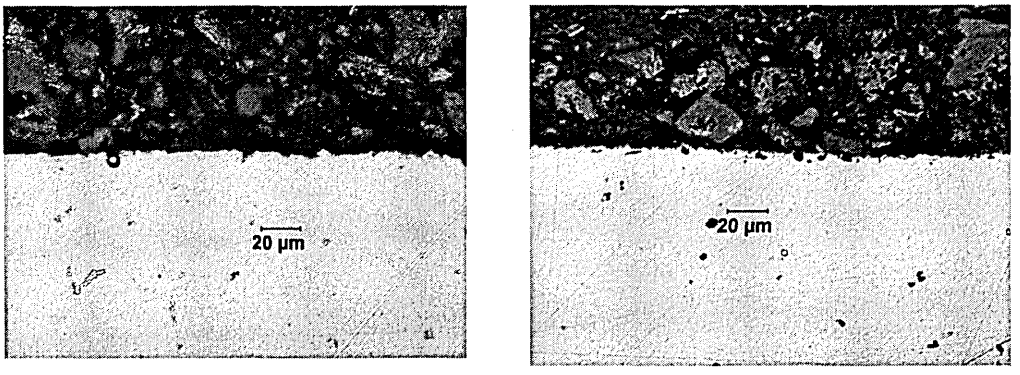

(a) (b)

Figure 4.53– Damage observed in left and right corner for Test I 2; Nominal contact pressure – 140 MPa, Stroke – 24 μm, No of cycles 600,000.

The surface damage observed in Test I 2 is shown in Figure 4.52. Test I 2 was carried out at 140 MPa nominal contact pressure for 600,000 cycles. The measured slip amplitude was 24 μm. No cracks could be observed on the damage surface for this test.

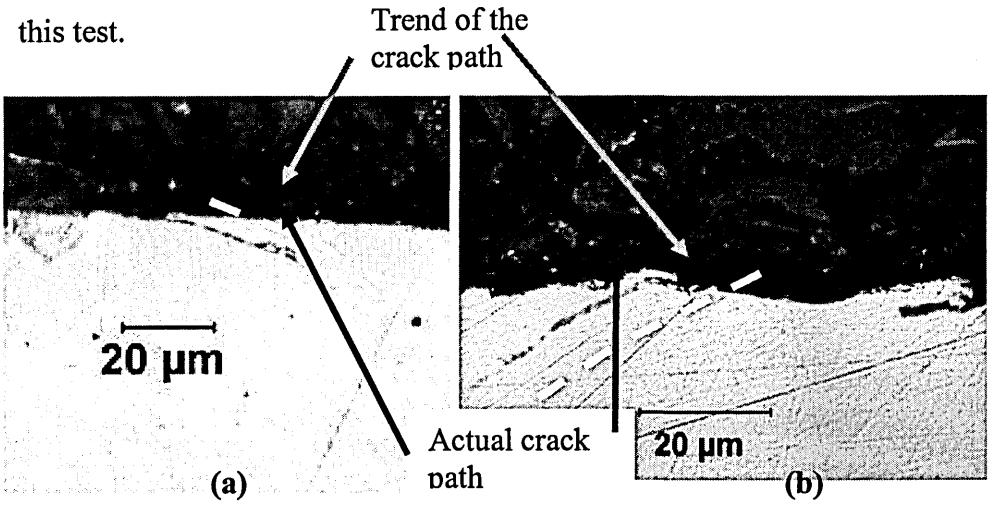

Figure 4.54– Damage observed in left and right corner for Test I 3; Nominal contact pressure – 180 MPa, Stroke – 32 μm, No of cycles 600,000.

Test I 3 was carried out at 180 MPa nominal contact pressure for 600,000 cycles. The measured slip amplitude was 32 μm. The surface damage observed in Test I3 is shown in Figure 4.54. Two cracks were observed on the damage surface for this test. Furthermore, the crack path observed is similar to the crack initiation angle and the crack path observed in the preliminary test series for tests P1, P2 and p4.

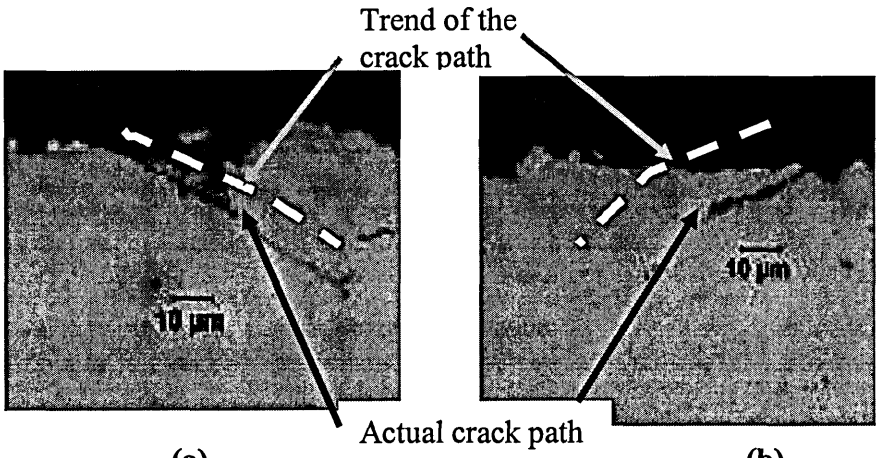

Figure 4.55– Damage observed in left and right corner for Test I 4; Nominal contact pressure – 160 MPa, Stroke – 30 μm, No of cycles 1,600,000.

Test I 4 was carried out at 160 MPa nominal contact pressure for 1,600,000 cycles. The measured slip amplitude is 30 μm. The surface damage observed in Test I 4 is shown in Figure 4.55. Two cracks could be observed on the damage surface for this test. Further more, the crack path observed in test I 4 is similar to the crack initiation angle and the crack path observed in the preliminary test series for test P1, test P2 and test p4.

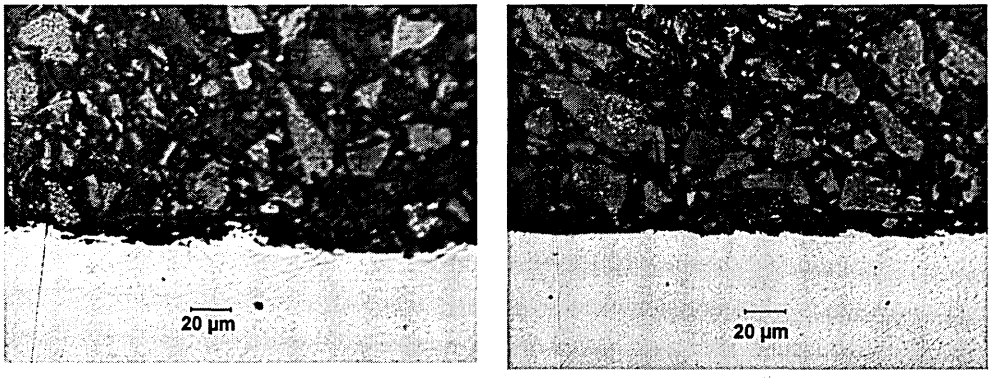

Figure 4.56– Damage observed in left and right corner for Test I 5; Nominal contact pressure – 120 MPa, Stroke – 28 μm, No of cycles 2,000,000.

The test I 5 was carried out at 120 MPa nominal contact pressure for 2,000,000 cycles. The measured slip amplitude was 28 μm. No cracks could be observed on the damage surface for this test. The surface damage observed in the Test I 5 is shown in Figure 4.56.

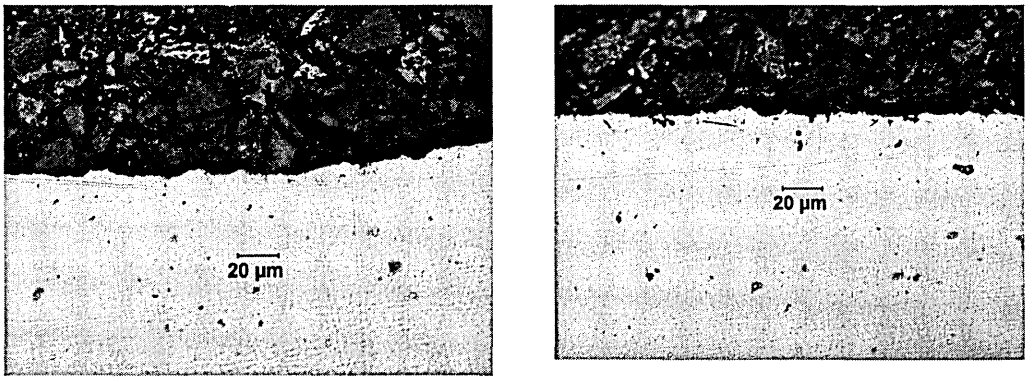

(a) (b)

Figure 4.57– Damage observed in left and right corner for Test I 6; Nominal contact pressure – 70 MPa, Stroke – 18 μm, No of cycles 2,000,000.

The test I 6 was carried out at 70 MPa nominal contact pressure for 2,000,000 cycles. The measured slip amplitude was 18 μm. No cracks could be observed on the damage surface for this test. The surface damage observed in the Test I 6 is shown in Figure 4.57.

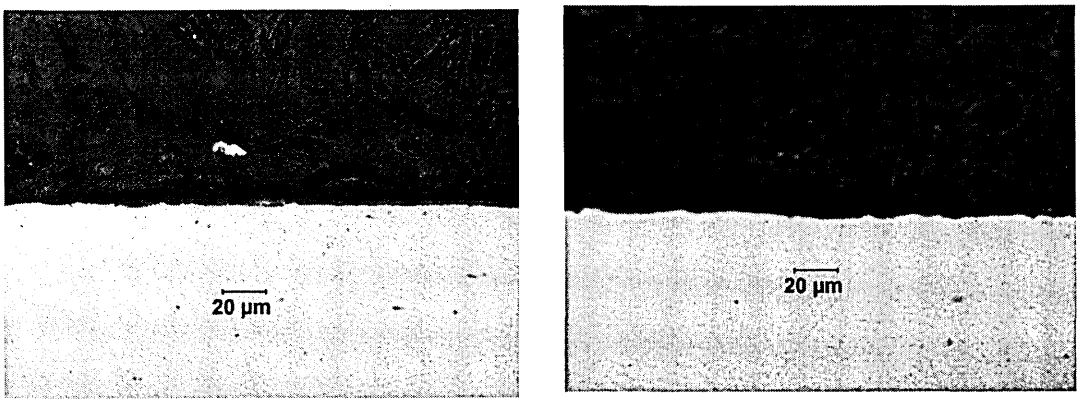

(a) (b)

Figure 4.58– Damage observed in left and right corner for Test I 7; Nominal contact pressure – 110 MPa, Stroke – 22 μm, No of cycles 2,800,000.

The test I 7 was carried out at 110 MPa nominal contact pressure for 2,800,000 cycles. The measured slip amplitude was 28 μm. The surface damage observed in the Test I 7 is shown in Figure 4.58. No cracks could be observed on the damage surface for this test.

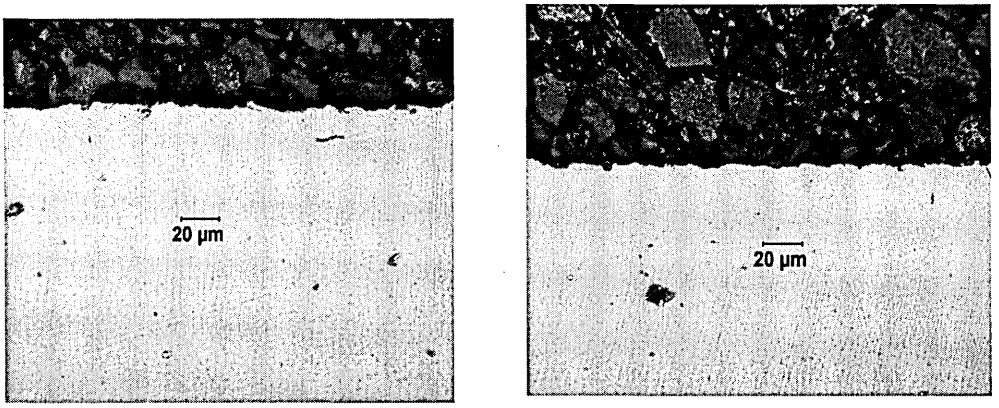

(a) (b)

Figure 4.59– Damage observed in left and right corner for Test I 8; Nominal contact pressure – 90 MPa, Stroke – 20 μm, No of cycles 2,800,000.

The test I 8 was carried out at 90 MPa nominal contact pressure for 2,800,000 cycles. The measured slip amplitude was 20 μm. No cracks could be observed on the damage surface for this test. The surface damage observed in the Test I 8 is shown in Figure 4.59.

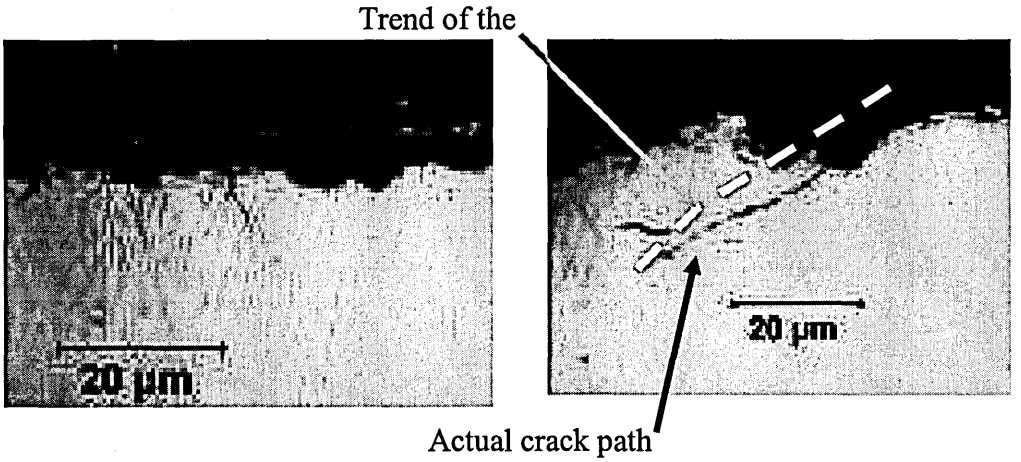

(a) **(b)**

Figure 4.60– Damage observed in left and right corner for Test I 9; Nominal contact pressure – 145 MPa, Stroke – 30 μm, No of cycles 4,100,000.

The test I 9 was carried out at 145 MPa nominal contact pressure for 4,100,000 cycles. The measured slip amplitude as 30 μm. The surface damage observed in the Test I 9 is shown in Figure 4.60. A crack was visible on the right hand side of the contact surface for this test. Further, the crack path observed in the test I 9 is similar to the crack initiation angle and the crack path observed in the preliminary test series for test P1, test P2 and test p4.

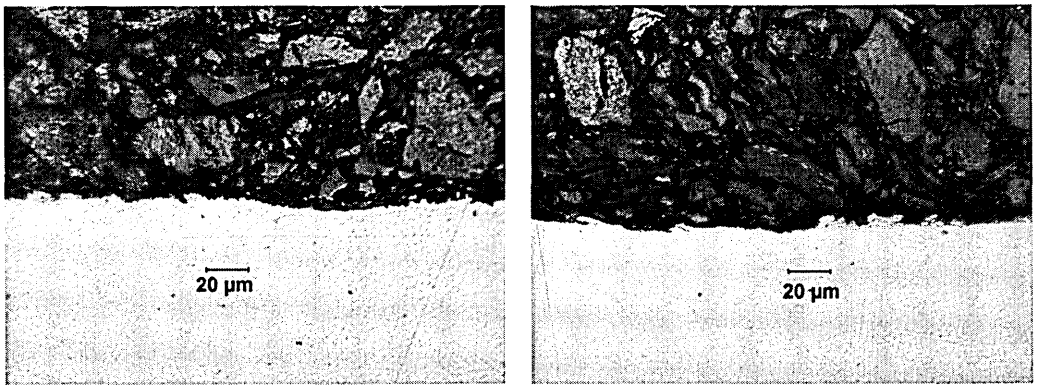

(a) (b)

Figure 4.61 - Damage observed in left and right corner for Test I 10; Nominal contact pressure – 80 MPa, Stroke – 18 μm, No of cycles 3,000,000.

The test I 10 was carried out at 80 MPa nominal contact pressure for 3,000,000 cycles. The measured slip amplitude was 18 μm. No cracks could be observed on the damage surface for this test. The surface damage observed in the Test I10 is shown in Figure 4.61.

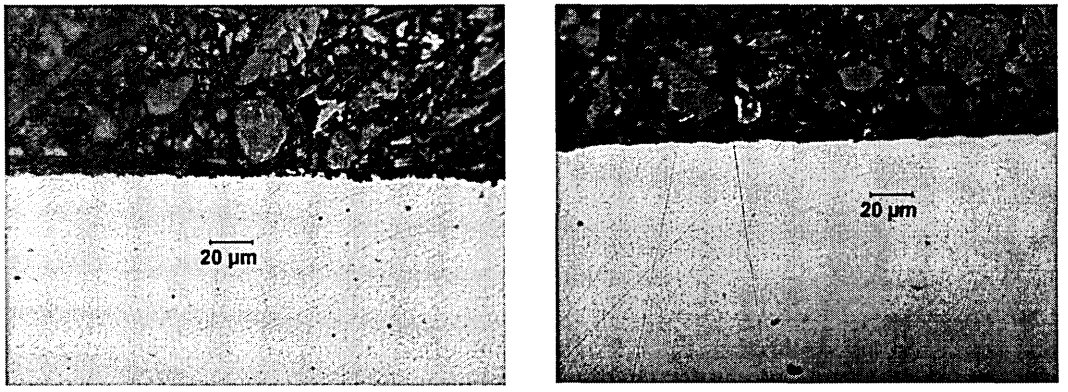

(a) (b)

Figure 4.62– Damage observed in left and right corner for Test I 11; Nominal contact pressure – 80 MPa, Stroke – 17 μm, No of cycles 5,000,000.

The test I 11 was carried out at 80 MPa nominal contact pressure for 5,000,000 cycles. The measured slip amplitude was 17 μm. The surface damage observed in the Test I11 is shown in Figure 4.62.No cracks could be observed on the damage surface for this test.

(a) (b)

Figure 4.63– Damage observed in left and right corner for Test I 12; Nominal contact pressure – 260 MPa, Stroke – 36 μm, No of cycles 2,000,000.

The test I 12 was carried out at 260 MPa nominal contact pressure for 2,000,000 cycles. The measured slip amplitude as 36 μm. . The surface damage observed in the Test I 12 is shown in Figure 4.63. Two cracks could be observed on the damage surface for this test. Further, the crack path observed in the test I 4 is well in agreement with the crack initiation angle and the crack path observed in the preliminary test series for test P1, test P2 and test p4. The surface damages observed in the P series and the I series have been discussed in Chapter 6, Section 6.5.

4.6 Cyclic tests

A series of cyclic tests were carried out in order to ascertain the reduction of fatigue strength due to fretting damage. The tests were carried out as follows. Firstly damage was created in the mixed slip condition and the gross slip condition separately in the same specimen as depicted in Figure 4.64.

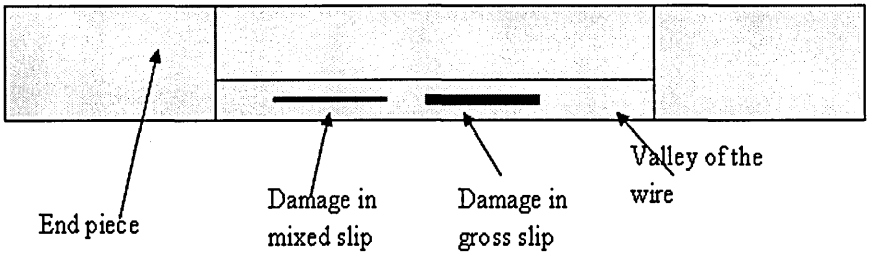

Figure 4.64 – Specimen preparation for cyclic testing.

Fretting damage was created in a particular specimen at a constant nominal contact pressure and a constant number of cycles in both conditions. The conditions for the tests were determined from the preliminary (P series) and the interrupted (I series) experimental programmes. Tests were carried out at 260 MPa, 200MPa and 180 MPa nominal contact pressure so that cracks are created in the mixed slip condition and wear in the gross slip condition. In the specimen C 1, two conditions similar to that of test P2 and test P3 were created and in the specimen C 2, conditions similar to that of tests P4 and P5 were created. In the specimen C 3, conditions similar to that of test I3 were created. The test conditions for the cyclic test series is depicted in Table 4.20

Table 4.7 – Fretting test programme for the cyclic test series

specimen	Test No	Displacement amplitude (μm)	Nominal contact pressure	No of cycles
Test C 1	C 101	40	260 MPa	250,000
Test C 1	C 102	80	260 MPa	250,000
Test C 2	C 201	27	200 MPa	300,000
Test C 2	C 202	50	200 MPa	300,000
Test C 3	C 301	32	180 MPa	600,000
Test C 3	C 302	55	180 MPa	600,000

Further, after creating the fretting damage in specimens C 1, C 2 and C 3, the specimens were subjected to cyclic loading. The direction of cyclic loading application is shown in Figure 4.65

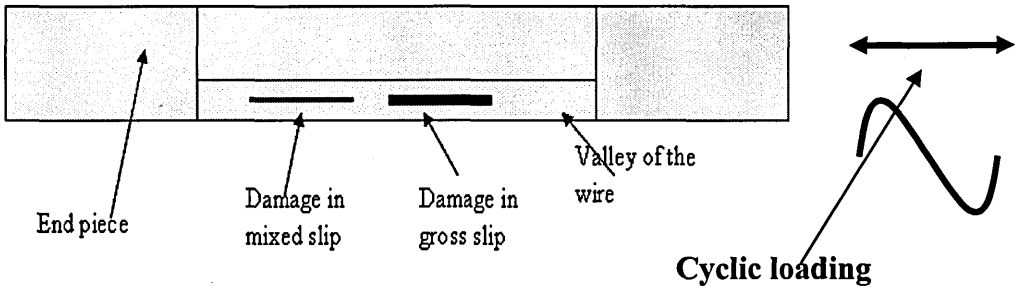

Figure 4.65 – Direction of the cyclic loading.

This bulk cyclic loading direction is the one that the pressure armour wire would experience in operation. At the time of testing, it was expected that the fretting damage in the mixed slip condition or gross slip condition would significantly reduce the fatigue strength in specimen C 1, C 2 and C 3. The cyclic loading test programme is given in Table 4.8.

Table 4.8 – Cyclic test programme

specimen	**Test stage 1**		**Test stage 2**	
	Stress amplitude % fatigue strength	No of cycles	Stress amplitude % fatigue strength	No of cycles
Test C **1**	80 %	5,000,000	90 %	3,000,000
Test C **2**	80 %	5,000,000	90 %	3,000,000
Test C **3**	80 %	5,000,000	90 %	3,000,000

The specimens were subjected to a two step cyclic loading programme. First the specimens were subjected to cyclic loading at stress amplitude of 80 % fatigue endurance strength up to 5,000,000 cycles and then again at stress amplitude of 90 % fatigue endurance strength up to 3,000,000 cycles. Despite the fact that both specimens were subjected to cyclic loading at very high stress amplitude, the specimens were not failed. Post test specimens were sectioned for examination and observations are given in Figure 4.66 to Figure 4.71.

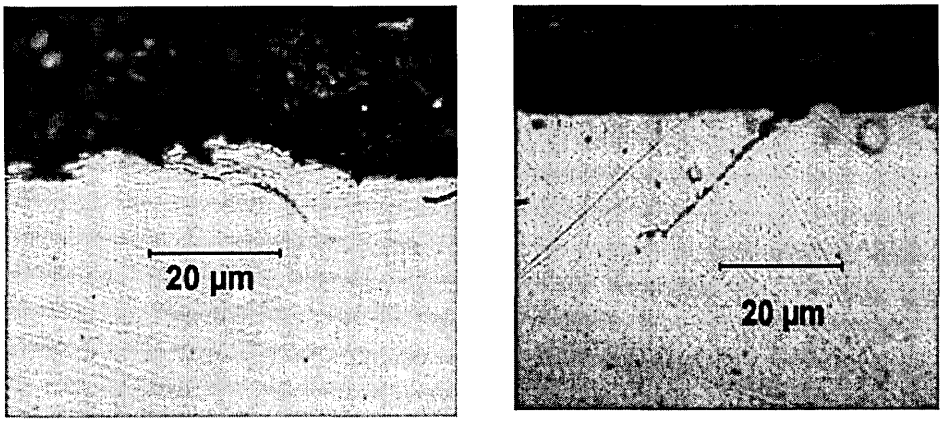

(a) (b)

Figure 4.66– Damage observed in left and right corner for test C 101

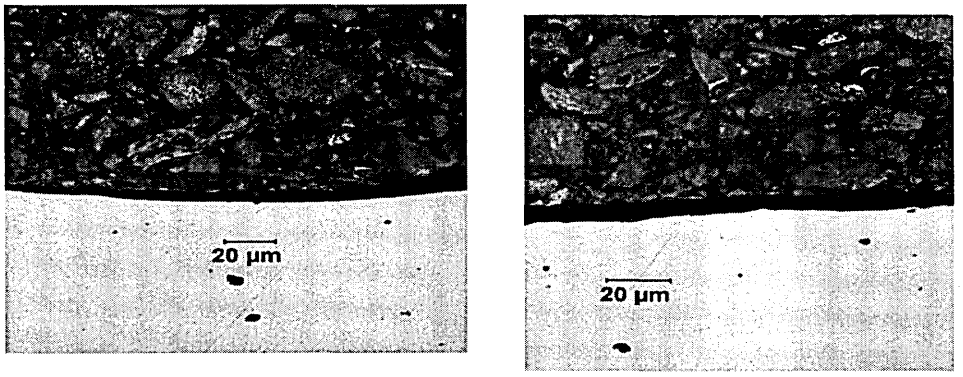

(a) (b)

Figure 4.67 – Damage observed in left and right corner for test C 102

The surface damage observed in tests C 101 and C102 are shown in Figures 4.66 and 4.67 respectively. Similar damage type was observed in C 101 and C 102 to that of tests P2 and P3.

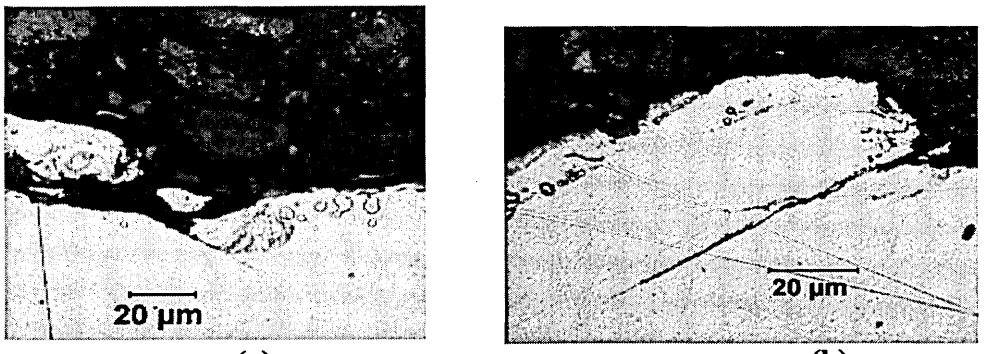

(a) (b)

Figure 4.68 – Damage observed in left and right corner for test C 201

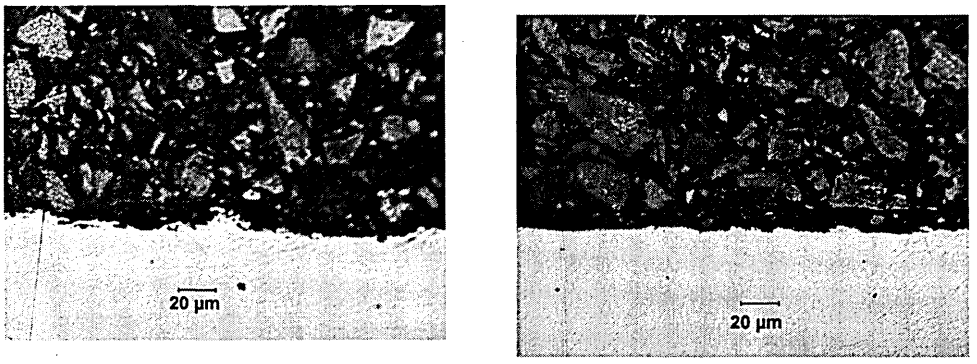

(a) (b)

Figure 4.69 – Damage observed in left and right corner for test C 202

Tests C 201 and C 202 were carried out under simialr conditions to Test P4 and P5. The surface damage observed in these tests are shown in Figure 4.68 and Figure 4.69 respectively. Microscopic observations revealed similar damage to that of Tests P4 and P5.

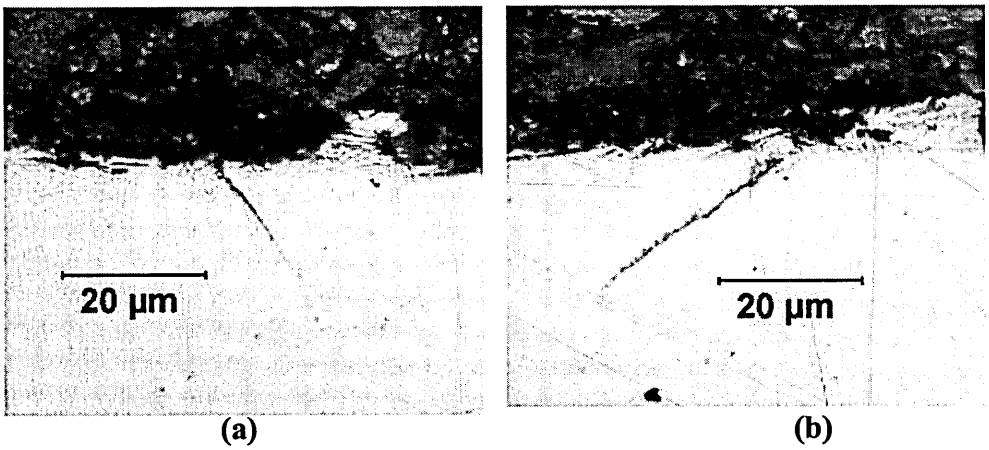

Figure 4.70 – Damage observed in left and right corner for test C 301

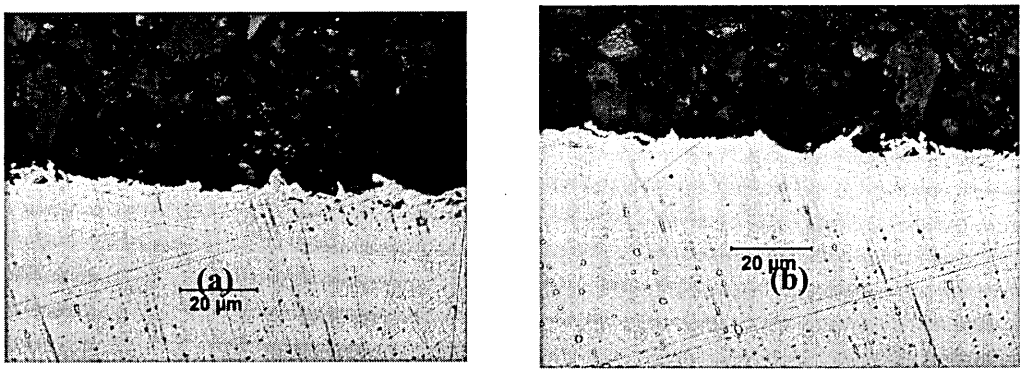

Figure 4.71 - Damage observed in left and right corner for test C 302

The tests C 301 was carried out under similar conditions to Test I 3 and microscopic observations of tests C 301 revealed similar type of damage to that of Test I 3. The test C 302 was carried out at the same nominal contact pressure and number of cycles the test I 3 was carried out but at higher slip amplitude in order to make sure that the slip condition is gross sliding. The surface damage observed in tests C 301 and test C 302 are shown in Figures 4.70 and 4.71 respectively.

CHAPTER 5: NUMERICAL ANALYSIS

Various numerical methods applicable to predict fretting damage behaviour were discussed in Chapter 2. Most of these methods are based on general multiaxial fatigue or fracture mechanics criteria developed for conventional fatigue (cyclic loading) damage predictions. Recently, successful fretting fatigue predictive models were developed based on these methods with certain modification or adaptation to address specific features of contact stress fields, for fretting conditions [**14,69,70,78,80**]. These methodologies are discussed in Chapter 2. In this chapter, a fracture mechanics based numerical procedure to predict the fretting damage behaviour is presented. The advantage of this methodology is that it predicts the crack initiation angle, crack path, whether the crack is self arresting or not, crack length and crack propagation life.

5.1 Contact geometry, pressure and stress distributions

The contact geometry for the current application is shown in the Figure 5.1

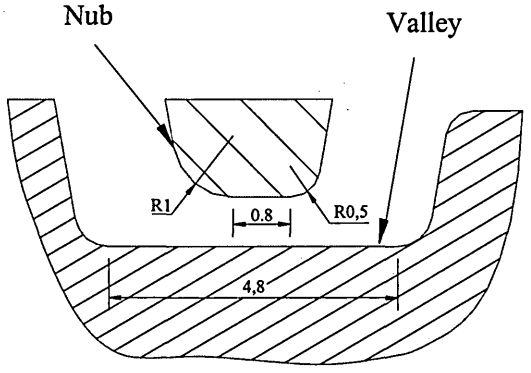

Figure 5.1 – Contact geometry for the current application

In the nub (which is the fretting pad in the current application) the corner radii on either side are different, which makes it unique when compared with previous contact geometries used in fretting experiments reported in the literature.

A closed form analytical method to calculate pressure distributions for a contact geometry with flat rounded corners was given by Ciavarella. et al **[46]** (Equation 2.5). The equation was originally developed for a contact with similar radii corners on either side. This equation is adapted to the current application by considering the contact profile as two separate halves having two different corner radii.

5.1.1 Equilibrium position for two halves

It was assumed that each halve consists of a radius R (R = R_1 or R_2) and flat length of $b \pm \delta$ as shown in Figure 5.2.

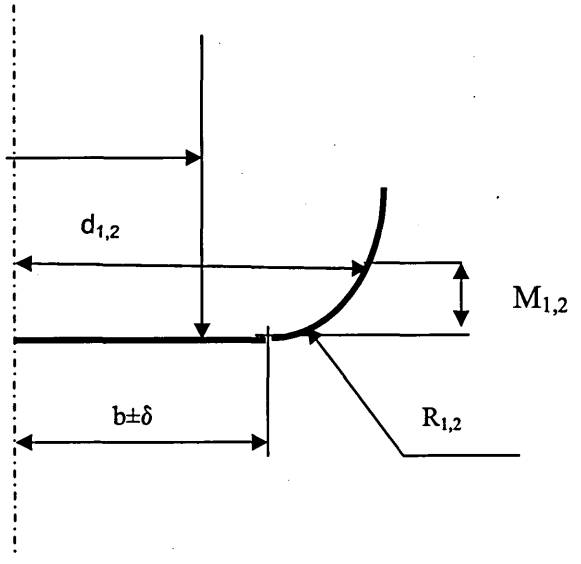

Figure 5.2 – Nomenclature for the pressure calculation

Initially a variable δ was assumed and the flat region in the first halve was assumed to be $(b+\delta)$ and the second half $(b-\delta)$. Equation 2.6 incorporating δ is written in the form; equation 5.1

$$\frac{4\Pr}{(b\pm\delta)E^*} = \frac{\pi - 2\phi_0}{4\sin^2\phi_0} + \frac{\cot\phi_0}{2} \qquad \text{-(5.1)}$$

d_1 and d_2 were calculated adapting the Equation 2.8 as,

$$d_{1,2} = \frac{(b\pm\delta)}{\sin\phi_0} \qquad \text{-(5.2)}$$

Considering Figure 5.3, the displacements M_1 and M_2 were derived as;

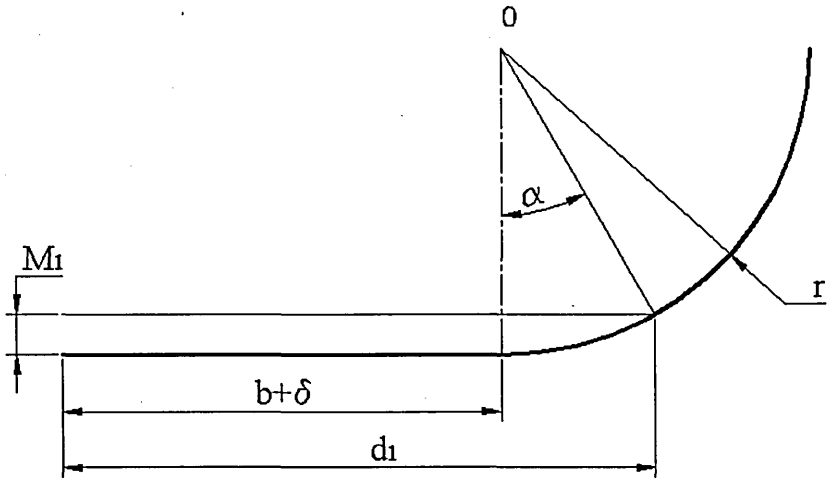

Figure 5.3 – the equilibrium position for one side of pad

$$Cos\alpha = \frac{r - M_{1,2}}{r} \qquad \text{-(5.3)}$$

$$\sin\alpha = \frac{d - (b\pm\delta)}{r} \qquad \text{-(5.4)}$$

$$M_{1,2} = r(1 - \cos(\sin^{-1}\left(\frac{d-(b\pm\delta)}{r}\right) \qquad \text{-(5.5)}$$

Where,

M_1 – the amount of the pad immersed into the specimen one side of the pad

M_2 – the amount of the pad immersed into the specimen in other side of the pad

The variable δ was obtained by iteration, when the condition $M_1 = M_2$ was satisfied. The pressure distribution obtained for the contact geometry is shown in figure 5.4, at 250 MPa nominal contact pressure.

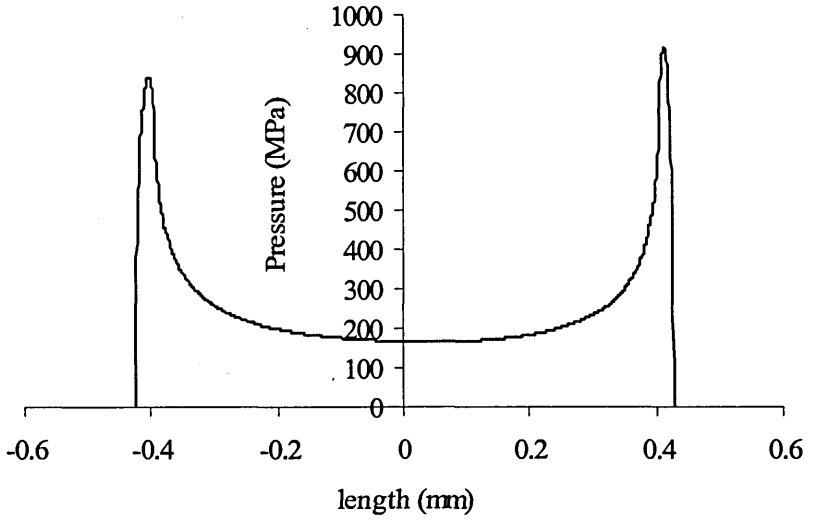

Figure 5.4 – Pressure distribution at 260 MPa contact pressure for the nub and valley contact.

The pressure distribution depends on the corner radius and the nominal contact pressure. The peak pressure is highest at the corner with lowest radius (r= 0.5 in the

current application). The pressure distributions obtained are used further to calculate the subsurface stress distributions.

5.1.2 Stress distributions

If we consider an elastic half space loaded over (0<x<b), by a normal pressure P and tangential traction Q distributed in an arbitrary manner as shown in Figure 5.5, the stress distributions are given by **[42]**.

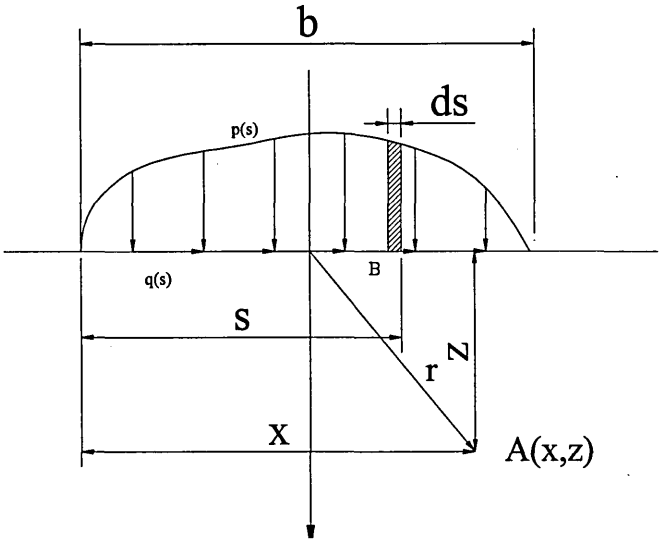

Figure 5.5 – Calculation of stress distribution of a contact half space.

$$\sigma_{xx} = -\frac{2z}{\pi}\int_0^b \frac{p(s)(x-s)^2 ds}{\{(x-s)^2+z^2\}^2} - \frac{2}{\pi}\int_0^b \frac{q(s)(x-s)^3 ds}{\{(x-s)^2+z^2\}^2} \qquad \text{-(5.6)}$$

$$\sigma_{zz} = -\frac{2z^3}{\pi}\int_0^b \frac{p(s)ds}{\{(x-s)^2+z^2\}^2} - \frac{2z^2}{\pi}\int_0^b \frac{q(s)(x-s)ds}{\{(x-s)^2+z^2\}^2} \qquad \text{-(5.7)}$$

$$\tau_{xz} = -\frac{2z^2}{\pi}\int_0^b \frac{p(s)(x-s)ds}{\{(x-s)^2+z^2\}^2} - \frac{2z}{\pi}\int_0^b \frac{q(s)(x-s)^2 ds}{\{(x-s)^2+z^2\}^2} \qquad \text{-(5.8)}$$

The stress tensor for the nub and valley contact including these stresses are shown in figure 5.6

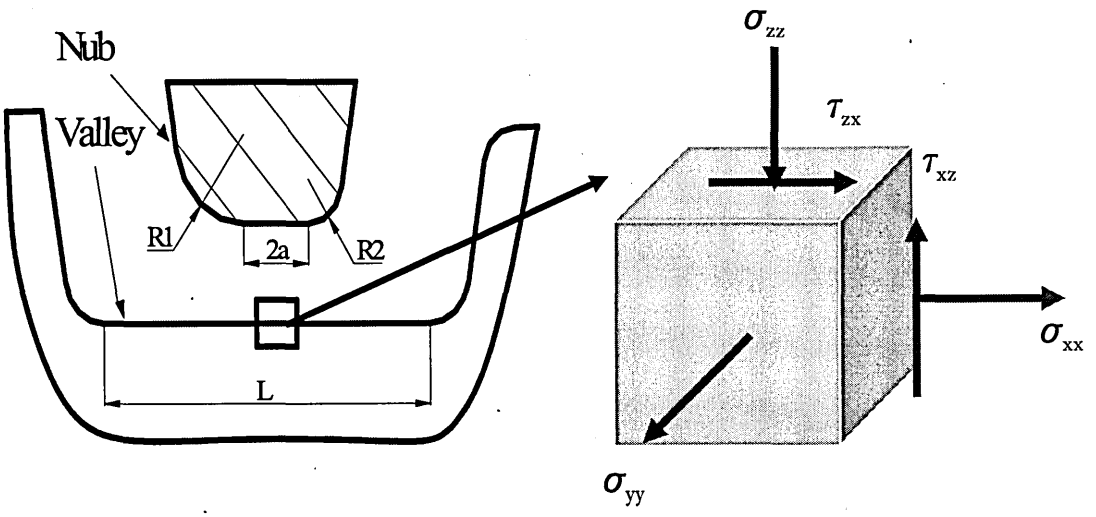

Figure 5.6 - The stress tensor for the nub and valley contact

In the stress tensor, σ_{yy} is induced due to the hoop stress of the pipe, σ_{xx} and τ_{xz} were due to friction and σ_{zz} was due to contact load. The calculated distribution of these stresses along the contact is shown in Figure 5.7 and Figure 5.8.

When the pad is moving from left to right (one corner to the other), the left side of the pad is called the trailing edge and the right side is called the leading edge. After reaching the right edge of displacement, the pad starts to move in the reverse direction and the leading edge changes to the trailing edge and the trailing edge changes to the leading position. The stress distribution, when the pad is moving from right to the left is then reversed to reflect the trailing and leading edge stress state. Typical Stress distribution at 260 MPa average contact pressure at 10 μm depth when pad moving from left to right is shown in the figure 5.7 and when the pad is moving right to left is shown in the figure 5.8.

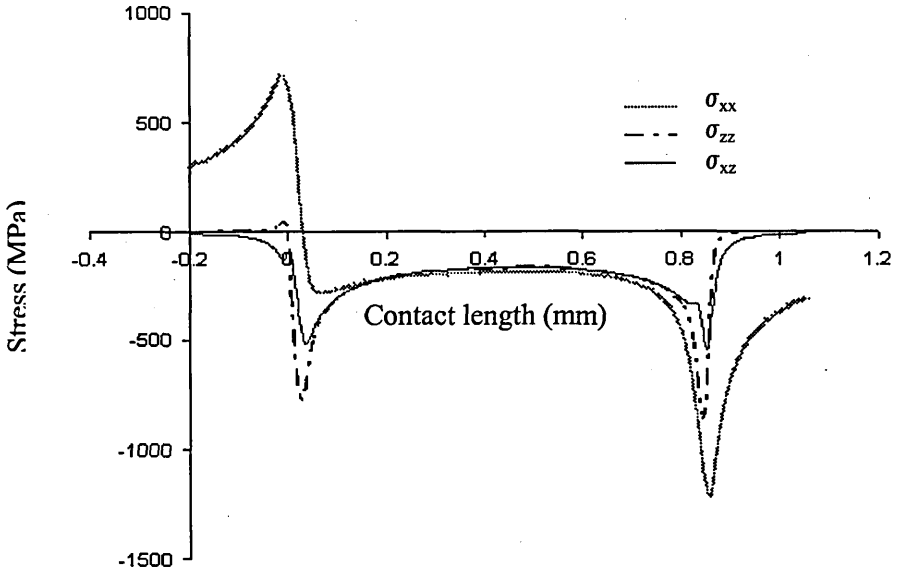

Figure 5.7 – Stress distribution, pad moving from left to right at 260 MPa nominal contact pressure, 10 μm depth ,

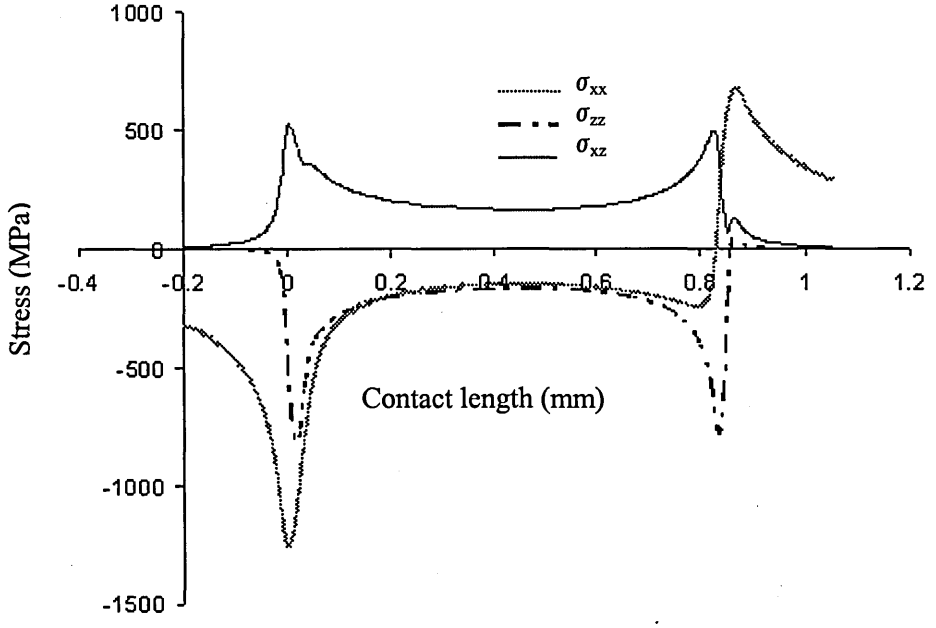

Figure 5.8 – Stress distribution at 260 MPa contact pressure, 10 μm depth , pad moving right to left

Analysis of Figures 5.7 and 5.8 show that a significant tensile stress is imposed in the vicinity of the trailing edge on the surface of the specimen by the σ_{xx} component of the stress tensor and a compressive stress in the vicinity of the leading edge. It is obvious that this cyclic variation of the stress state in microscopic movements is more responsible for fretting damage on the edges of the contact of the specimen and the pad **[42]**. A fracture mechanics based critical plane analysis to predict the crack length and crack propagation life is presented below.

5.2 Damage model

Fracture mechanics theories deal with the propagation of cracks in materials. Within the framework of fracture mechanics assumptions, the mode I (opening mode), mode II (shearing mode) are applicable to the crack growth under fretting conditions as shown in Figure 5.9.

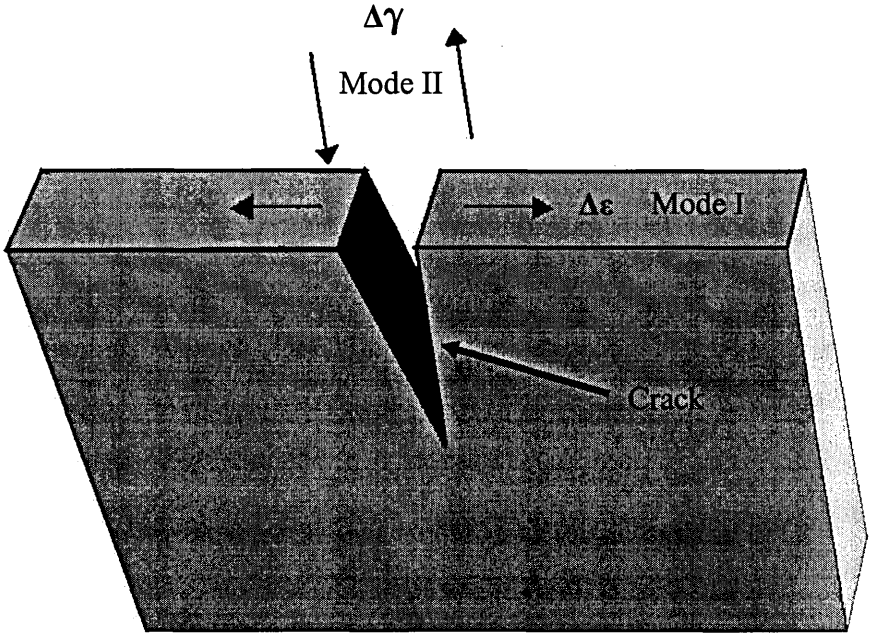

Figure 5.9 – Mode I and Mode II cracking modes in fretting.

If the loading history and the loading conditions are known, critical plane based models allow the determination of the fracture plane and the calculation of the fatigue life of the material. Critical plane approaches have evolved from experimental observations of the nucleation and growth of cracks during loading. Cracks will initiation and grow depending on the material stress and strain state either in the plane with maximum shear range (Mode II cracking) or tensile planes normal to the plane with maximum normal strain range (Mode I cracking) **[85, 86]**. The general aim of the critical plane concept is to reduce the multiaxial stress state to an equivalent uniaxial one.

The advantage of multiaxial fatigue analysis using the critical plane method is that in addition to the life prediction, it can predict the crack initiation angle if a suitable model is used for the stress state of current application. Recently, critical plane based approaches have found wider application in fretting fatigue analysis **[2, 14, 55 62, 66].** This is mainly due to the simplicity of applying critical plane based methods to a complex multiaxial state of loading in fretting and their ability to use plain fatigue data to predict fretting fatigue life.

5.2.1 Procedure

The analysis was carried out for the mode II –(shear strain) criteria and mode I – (normal strain) criteria separately. The crack nucleation location was assumed to be the point with maximum shear strain range on the contact surface. The propagation of the crack was analysed in small increments. A schematic explanation is presented in Figure 5.10. A 5 μm increment was used in the current analysis.

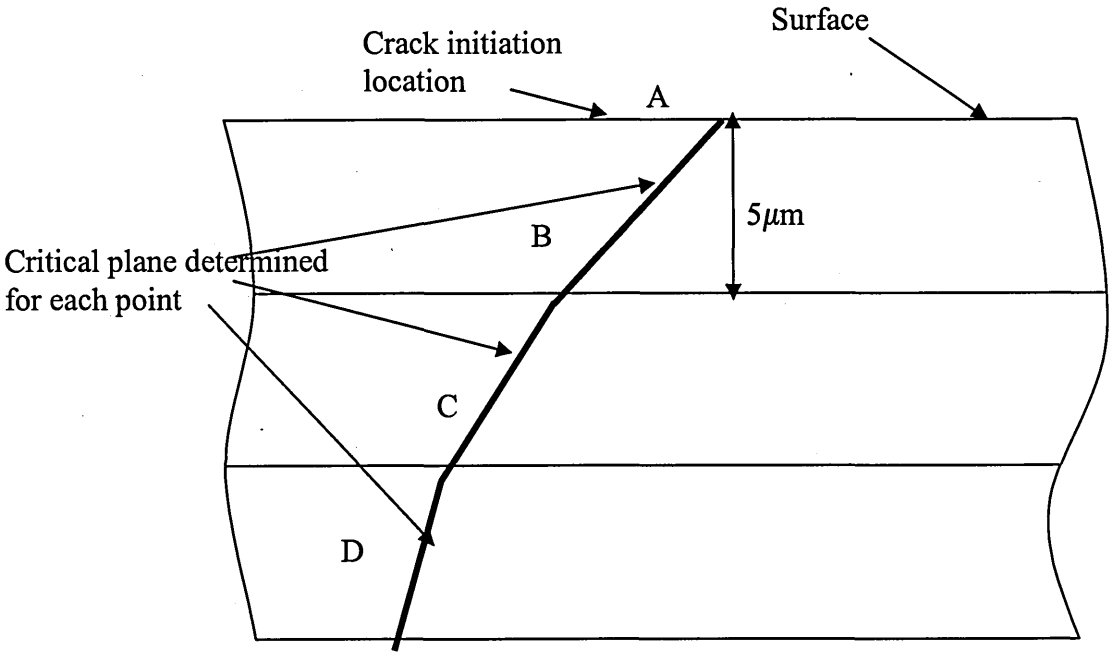

Figure 5.10 – Schematic representation of the analytical procedure.

The first step was to evaluate the state of stress condition on the contact surface and to ascertain the most probable crack initiation location (point A). Then it was decided that the crack would propagate along the plane with the maximum shear strain range or the plane with the maximum normal strain range (critical plane). Then the stress strain state was evaluated again at a point 5 μm deeper than the previous sample location along the previously predicted crack path and the new critical plane orientation was evaluated again to predict the most probable path the crack might take.

5.2.2 Normal, shear and resultant stresses on an oblique plane

Consider an oblique plane ABC to x y and z axes as shown in Figure 5.11. The normal vector σ_n makes angles $\boldsymbol{n_x}$ $\boldsymbol{n_y}$ and $\boldsymbol{n_z}$ with the $\boldsymbol{yz}$ $\boldsymbol{xz}$ and $\boldsymbol{xy}$ planes.

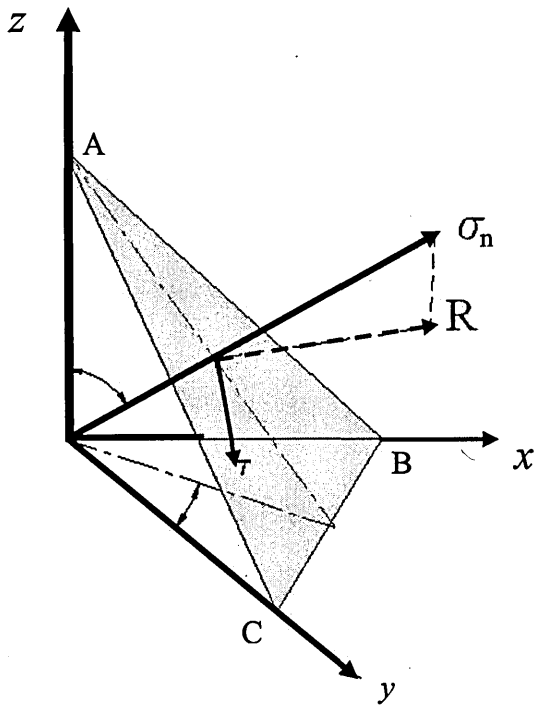

Figure 5.11 - Normal, shear and resultant stresses on an oblique plane.

The stress components in x y and z directions are given by [87];

$$R_{xn} = \sigma_{xx}\cos n_x + \tau_{xy}\cos n_y + \tau_{xz}\cos n_z \qquad \text{-(5.9)}$$

$$R_{yn} = \sigma_{yy}\cos n_y + \tau_{yx}\cos n_x + \tau_{yz}\cos n_z \qquad \text{-(5.10)}$$

$$R_{zn} = \sigma_{zx}\cos n_z + \tau_{zy}\cos n_x + \tau_{zy}\cos n_y \qquad \text{-(5.11)}$$

The resultant stress on the plane ABC is given by;

$$R^2 = R_{xn}^2 + R_{yn}^2 + R_{zn}^2 \qquad \text{-(5.12)}$$

The normal stress σ_n is given by resolution perpendicular to the plane ABC, [84].

$$\sigma_n = R_{xn}\cos n_x + R_{yn}\cos n_y + R_{zn}\cos n_z \qquad \text{-(5.13)}$$

The shear stress is given by,

$$\tau = \sqrt{R^2 - \sigma_n^2} \qquad \text{-(5.14)}$$

Substituting equations 5.9, 5.10 and 5.11 in 5.13 gives

$$\sigma_n = \sigma_{xx}\cos^2 n_x + \sigma_{yy}\cos^2 n_y + \sigma_{zz}\cos^2 n_z + 2\tau_{xy}\cos n_x \cos n_y + \\ + 2\tau_{yz}\cos n_y \cos n_z + 2\tau_{xz}\cos n_x \cos n_z \qquad \text{-(5.15)}$$

5.3 Critical plane analysis

A three dimensional critical plane analysis was carried out. The determination of the critical plane orientation is a crucial step in this analysis. The critical plane was taken as the plane with the maximum normal strain range [28] for normal strain criteria and the maximum shear strain range [16] for the shear strain criteria.

The orientation of an arbitrary plane can be defined by a normal vector as shown in the Figure 5.12, which is at a right angle to the plane concerned. In the current analysis, the normal vector is defined using two angles α and β. The angle α is the angle of the normal vector in the ***xy*** plane and the angle β is the angle of the normal vector from the ***xy*** plane.

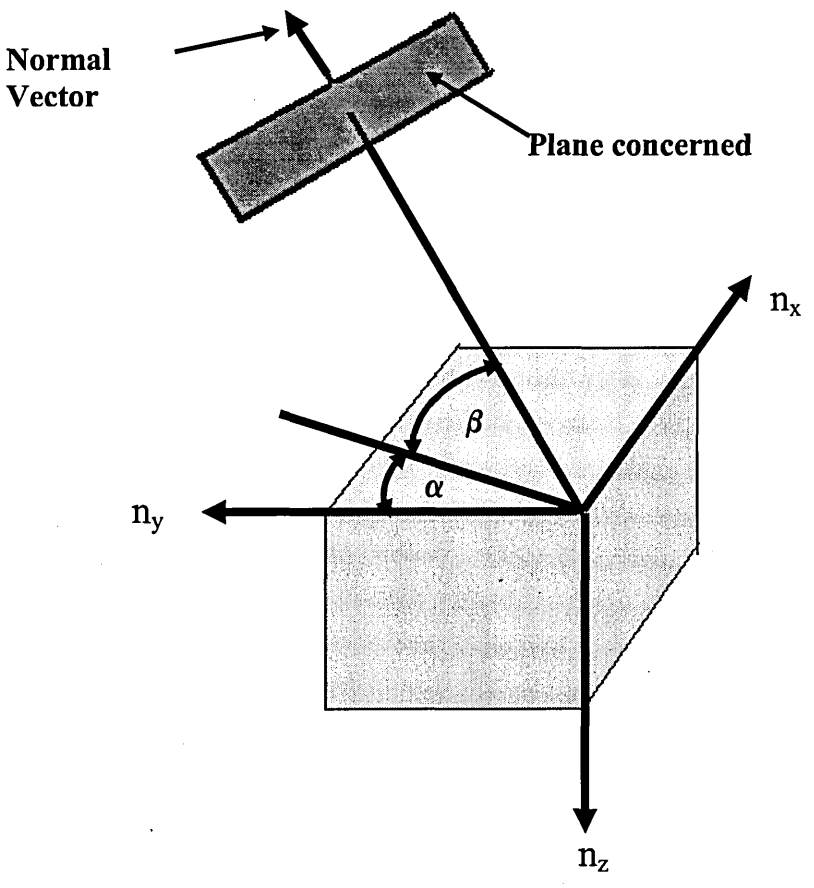

Figure 5.12 – directional cosines for the critical plane

The directional cosines for the normal vector are defined as,

$$n_x = \sin\alpha\cos\beta \qquad \text{-(5.16)}$$

$$n_y = \cos\alpha\cos\beta \qquad \text{-(5.17)}$$

$$n_z = -\sin\beta \qquad \text{-(5.18)}$$

Three-dimensional stress and strain transformations using the above equations are applied to each element to find the corresponding stresses and strains for 36 different

candidate critical plane angles, , in increments of 5° for $-\frac{1}{\pi} < \alpha < \frac{1}{\pi}$ and additional increments of 5° for $-\frac{1}{\pi} < \beta < \frac{1}{\pi}$.

5.3.1 Crack initiation location.

It is a well known fact from fatigue damage theories [30, 67] that local plastic deformation and damage accumulation must take place in order for a crack to initiate. It is assumed here that the surface crack is most susceptible to initiate from the location with maximum shear strain range or the maximum normal strain range. The distribution of shear strain range and normal strain range close to the vicinity of the contact edge, in the critical plane is shown in Figures 5.13 and 5.14 for left corner and the right corner of the contact respectively.

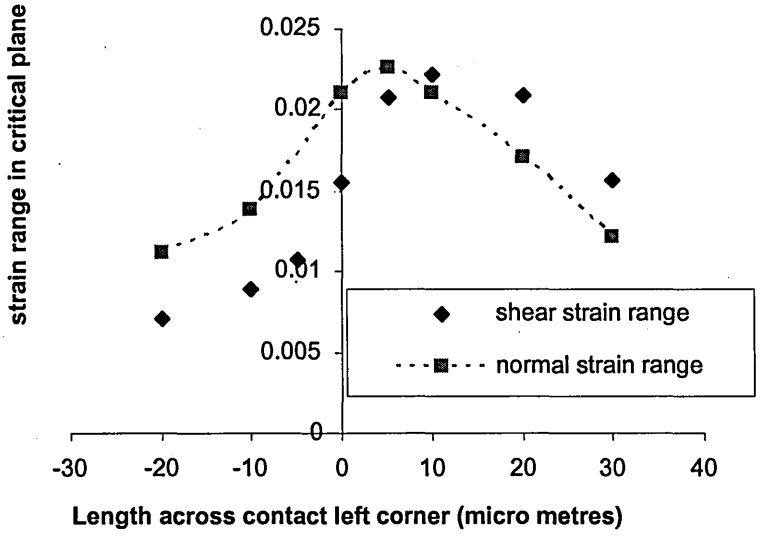

Figure 5.13 - Crack initiation location at left corner

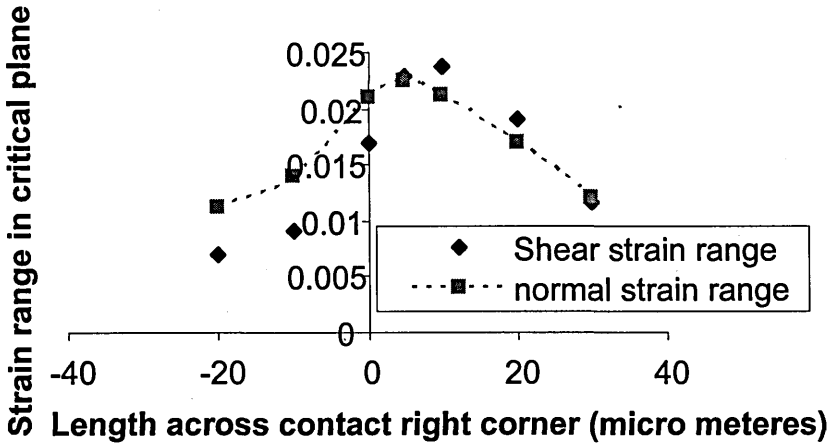

Figure 5.14 - Crack initiation location at right corner.

Both parameters predict that the most favourable location for the crack to initiate is at the edge of the contact.

5.3.2 Crack path analysis for mode I and mode II cracking

The prediction of the crack path for the 260 MPa nominal contact pressure in the left side corner for mode I and mode II cracking is shown in Figure 5.15 and Figure 5.16 respectively. The initial crack angle for the mode I prediction was 15^0 with the vertical direction and for the mode II predicted angle was 40^0 with the vertical . When moving into the material, the crack angle for mode I varied within the range of 20^0 - 30^0 and for the mode II prediction, the crack angle varied within the range of 60^0 - 70^0 as depicted in Figure 5.15 and Figure 5.16.

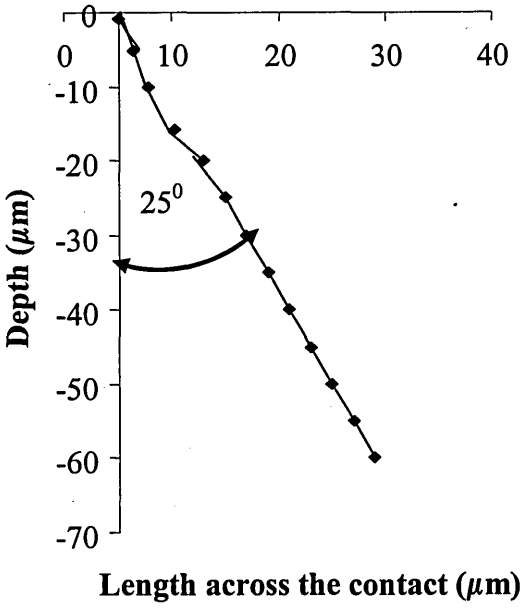

Figure 5.15- Crack path analysis for pure Mode I cracking

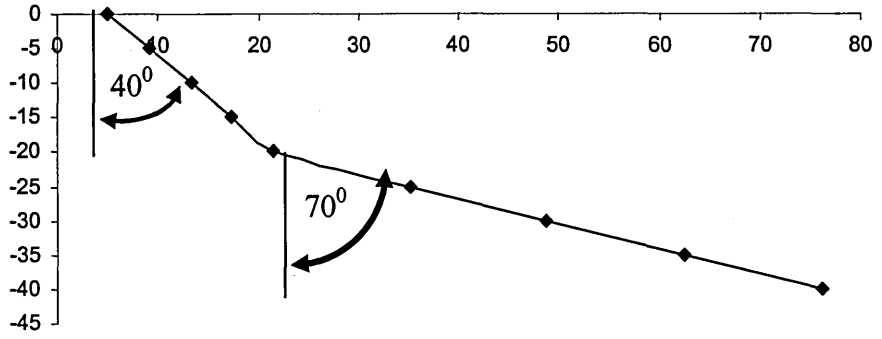

Figure 5.16 -Crack path analysis for pure mode II cracking

The most favourable path for the crack to propagate on is either the mode I crack path or the mode II crack path or a combination of both. A severity parameter is proposed based on von Misses yield criterion.

5.3.3 Severity comparison between shear and normal strain.

It was assumed that surface fretting cracks will initiate at a critical location where stress conditions are very high and propagate into the material either in the shear plane or the normal plane depending on the severity of stress state on each plane. The analysis was carried out in 5 μm steps and the stress state was analysed on each step to ascertain the direction of the crack. Severity for both the shear and the normal plane were compared with the yield criteria as follows.

Severity coefficient γ_K for the shear plane (mode II cracking) was assumed to be a function of shear strain range $\Delta\gamma$ [16, 82] in the critical plane and the severity coefficient for the normal plane (mode I cracking) the severity parameter ε_K was assumed to be a function of the normal strain range $\Delta\varepsilon$ [16, 82] in the critical plane.

A typical crack subjected to mode I loading is shown in Figure 5.17 and a typical crack subjected to mode II loading is shown in Figure 5.18.

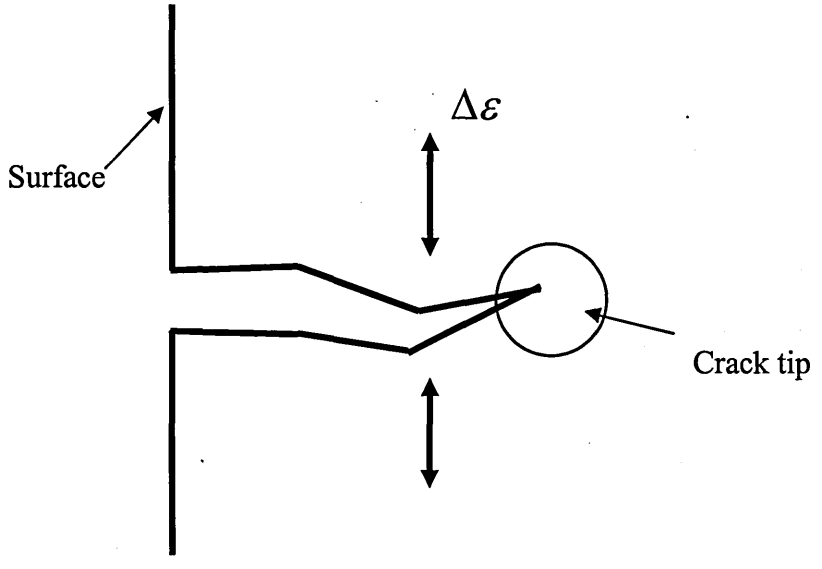

Figure 5.17 – A typical crack tip subjected to mode I loading.

In mode II cracking, the crack grows in the direction of shear loading and depends on the maximum shear strain range. During shear loading, the irregularly shaped crack results in friction that will retard the crack growth. A tensile normal stress will separate the crack surface and reduce the frictional forces allowing the crack to grow further. Therefore the general formulae for mode II crack growth take the form

$G\Delta\gamma + S\sigma_{Max}$ [26, 82].

Where,

$\Delta\gamma$ - Shear strain amplitude in the critical plane

σ_{Max} - Maximum normal stress in the critical plane

G - Shear modulus of the material

S - Material parameter

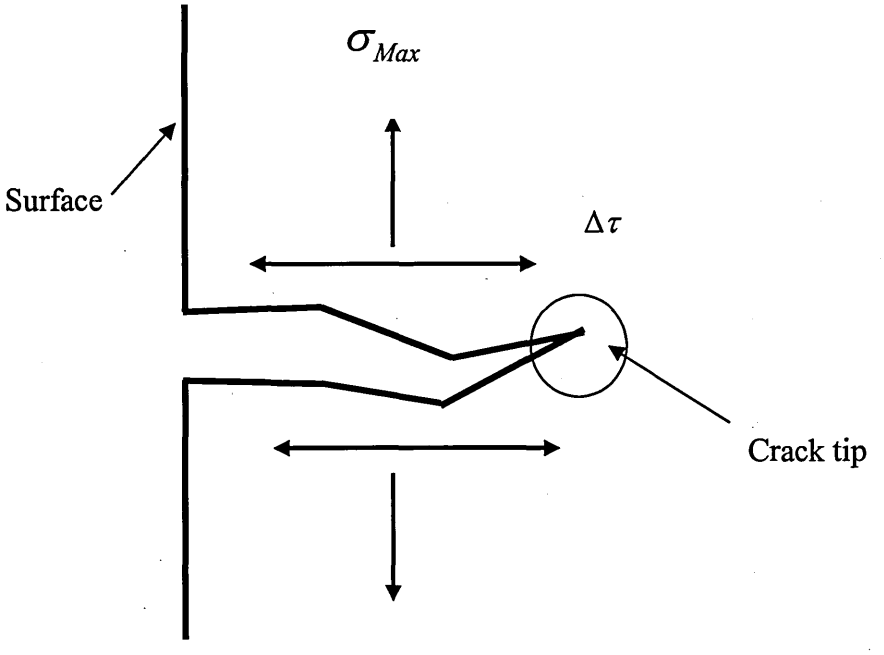

Figure 5.18 – A typical crack tip subjected to mode II loading.

Further, from the observation that it is necessary to create cyclic plasticity at the crack tip to propagate the crack, both parameters were compared with the yield strength of the material using the octahedral yield criteria, to ascertain and compare the **severity** of both parameters. The severity coefficients ε_k and γ_K are defined as,

$$\Delta\sigma_{Max} = \sigma_y \varepsilon_K \qquad \text{-(5.19)}$$

for the normal strain criteria (mode I)

and

$$G\Delta\gamma + \lambda\sigma_{Max} = \tau_y \gamma_K \qquad \text{-(5.20)}$$

for shear strain criteria (mode II)

where λ is a material parameter

The shear criteria (mode II) after substituting the von-Mises yield criteria,

$$\frac{1}{\sqrt{3}}\sigma_y \gamma_K = (\Delta\tau + K\sigma_{Max}) \qquad \text{-(5.21)}$$

If $\frac{\Delta\sigma_{Max}}{\sigma_y} > \frac{\sqrt{3}(G\Delta\gamma + K\sigma_{Max})}{\sigma_y}$; the crack will tend to follow the critical plane for mode I cracking. If $\frac{\Delta\sigma_{Max}}{\sigma_y} < \frac{\sqrt{3}(G\Delta\gamma + K\sigma_{Max})}{\sigma_y}$ then the crack tends to follow the mode II cracking.

5.3.4 Fracture mechanics analysis

The previous analysis was based on predicting the crack path for the crack to propagate due to the highly localised stress field on the contact surface but still questions remain un-answered. One is whether these cracks will propagate resulting in a catastrophic failure or not; another is about crack propagation life, in other words, at what number of loading cycles will the crack arrest or cause failure.

Although fracture mechanics theories can be successfully applied for life predictions of general fatigue situations, extra care must be taken when applying the LEFM theories to fretting situations. The major concerns that need addressing here are:

I. Fretting is a surface phenomena and a steep stress gradient exists very close to the contact and therefore a local mechanistic approach is more appropriate rather than a global approach when determining stress intensity factors.

II. The application of linear elastic fracture mechanic (LEFM) is inappropriate for short cracks which cross only a few grains of the material and therefore corrections to fracture mechanics theories are necessary in order to take account of short crack growth behaviour.

A fracture mechanics based analysis was carried out along the crack path predicted in Section 5.3.4 with corrections for short cracks.

Nisitani and Goto **[91]** have proposed that the rate of fatigue crack growth for short cracks is governed by equation 5.22. This equation was further established to be

reasonable to assume for short cracks by experimental and numerical analysis carried out by researchers **[21, 90]**.

$$\frac{da}{dN} = C(\Delta K_{eff} - \Delta K_{effth})^2 \qquad \text{-(5.22)}$$

where,

ΔK_{eff} - Effective stress intensity factor range, ΔK_{theff} - Effective threshold stress intensity factor range, N – Number of cycles, C – Crack growth coefficient

The ΔK_{theff} term represents the fact that the stress intensity range must exceed the threshold level, in order for short crack growth to occur.

McEvily and Yang **[90]** have proposed the term ΔK_{eff} as given in Equation 5.23 below to maintain a linear elastic formalism for short cracks.

$$\Delta K_{eff} = \left[\sqrt{2\pi r_e} + Y\sqrt{\frac{\pi}{2}a\left(\sec\left(\frac{\pi\sigma}{2\sigma_y}\right)+1\right)}\right]\Delta\sigma - \left(1-e^{-k}\right)\Delta K_{op\max} \qquad \text{-5.23}$$

They have found a good correlation of predictions with experimental results for short crack growth of carbon steel.

For the purpose of explanation, the Equation 5.23 is written as follows in terms of three different terms.

$$\Delta K_{eff} = \left[Term1 + Y\sqrt{Term2}\right]\Delta\sigma - term3 \qquad \text{-5.23 (a)}$$

Term1

According to McEvily and Yang **[90]**, Term1 takes into account the crack tip notch effect. The constant r_e is evaluated from the following equation.

$$\Delta K = \left\{\sqrt{2\pi r_e} + Y\sqrt{\pi a}\right\}\Delta\sigma \qquad \text{-5.24}$$

r_e is evaluated when $a=0$, $\Delta K = \Delta K_{effth}$ and $\Delta\sigma$ is the stress range at the endurance limit.

Term2

Term2 is calculated using the analysis proposed by Dugdale **[92]** to take into account the crack tip plasticity zone.

Term3

The third term accounts for the development of crack closure as a crack grows from the developing state to a length beyond which there is no further increase in crack closure.

For short cracks, EI Haddad et al **[93]** proposed from the observation that the threshold stress intensity factor for short cracks is less than that for long cracks and is calculated as follows.

$$\Delta K_{TH} = \Delta K_{TH\infty}\sqrt{\left(\frac{a}{a+d}\right)} \qquad \text{-(5.25)}$$

where, d is given by,

$$d = \frac{1}{\pi}\left(\frac{\Delta K_{TH\infty}}{Y\Delta\sigma_f}\right)^2 - a_0$$

Where, Y is a geometry factor, $\Delta\sigma_f$ is the fatigue limit for the given surface roughness, a_0 is the initial crack length set to the surface roughness and $\Delta K_{TH\infty}$ is the threshold stress intensity factor for a long crack

Further, the threshold stress intensity factor was corrected for the stress ratio in order to take into account the steep stress gradient and variation of stress ratio, very close to the contact surface. Walker **[88]** reported the dependence of the threshold stress intensity factor with the stress ratio as:

$$\Delta K_{TH\,eff} = \Delta K_{TH0}(1-R)^{n-1} \qquad \text{-(5.26)}$$

Where, R is stress ratio $= \sigma_{Min}/\sigma_{Max}$, ΔK_{TH0} Threshold stress intensity range for fully reversed cycles, $\Delta K_{TH\,eff}$ is effective threshold stress intensity range for given stress ratio and n is a material property

Further, Masounave and Bailon **[89]** reported that for carbon steel (n-1) = 0.93 so that the equation 5.26 can be written as

$$\Delta K_{TH\,eff} = \Delta K_{TH0}(1-R) \qquad \text{-(5.27)}$$

The fracture mechanics analysis was carried out until $\Delta K < K_{TH}$ for each point along the contact in the critical plane defined by the severity coefficient as shown in Figure 5.10. The life for the crack to propagate from one point to the other (from A to B; B to C etc) was carried out in incremental steps using the Equation 5.22 for mode I crack growth.

The cumulative life was calculated by adding the life spent on propagation of the crack in preceding section concerned. The material parameters assumed based on **[90]** are as follows,

$C = 2 \times 10^{-10}$ m/cycle

$k = 6$ 1/cycle

$K_{op\max} = 6.8$ MPa $m^{1/2}$

$\Delta K_{th,0} = 3.2$ MPa $m^{-1/2}$

A comparison of crack path, crack depth, and life predictions with experimental results are presented in the Chapter 6.

CHAPTER 6: DISCUSSION

The fretting damage behaviour of pressure armour wires of flexible pipes was investigated using the novel experimental set-up that has been designed and developed. Three series of tests were carried out and the results were presented in Chapter 4. During the investigations involving a wider range of loading conditions, various damage profiles, sliding conditions and, in some tests, fretting cracks were observed.

The preliminary test series was carried out in order to understand the effect of slip amplitude and contact pressure on friction, the damage behaviour, crack path, and the crack depth. The conditions under which cracks are observed was confined to a specific region of a "damage map". Detailed analyses of cracks revealed that they follow a path influenced by the local stress state. A fracture mechanics based critical plane analysis was developed to predict the crack path, crack depth and crack propagation life. The second experimental series (interrupted tests) was carried out in order to gain a better understanding of the crack growth process and to validate the crack path prediction and the damage map. A systematic quantification and analysis of results, together with a comparison of numerical predictions are presented in this discussion.

6.1 Preliminary experimental programme.

The preliminary experimental programme was carried out to cover a wide range of contact pressures and slip amplitudes. The nominal contact pressure was varied in the range from 60 MPa to 260 MPa and the slip amplitude was varied in the range from 20 μm to 80 μm. The tests ran approximately up to 250,000 loading cycles.

Pressure distribution

The predicted pressure distribution shows two peaks on either end of the contact. The peak values on either side are different in the current application due to the differences in corner radius. The corner with lower radius (0.5 mm) shown to be the highest peak of contact pressure while the higher corner radius (1.0 mm) led to comparatively lower peak contact pressure. At 260 MPa nominal contact pressure, the peak contact pressure was in the range of 850 MPa to 900 MPa (for each side) while the peak contact pressure ranged from 480 MPa to 500 MPa at 145 MPa nominal contact pressure. This clearly shows the influence of nominal contact pressure and the contact radius on the peak contact pressure. The lower the nominal contact pressure lower the peak contact pressure and the higher the corner contact radius the lower the peak contact pressure.

Slip boundaries

During the preliminary experimental investigation various slip conditions could be observed under different nominal contact pressure and slip amplitude. At low slip amplitudes the slip condition was mixed slip. As the slip amplitude was increased, a transition from mixed slip to gross slip was observed.

The slip condition was identified for each test by observing the behaviour of stabilised friction loops. The friction behaviour and the slip condition for each test is presented in Chapter 5.

A boundary between the mixed slip and gross slip condition was drawn from the results of preliminary experimental investigation. The slip boundary in a map of slip amplitude and nominal contact pressure as presented in Figure 6.1.

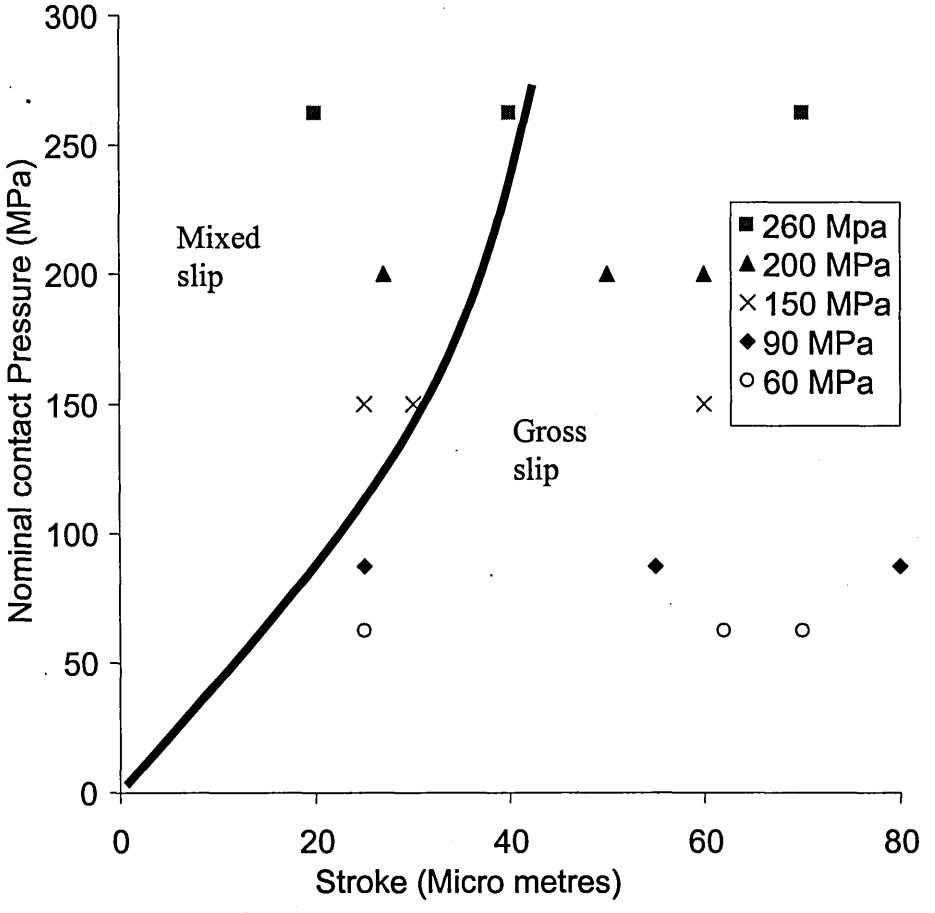

Figure 6.1- slip boundary between mixed slip and gross slip

The slip boundary shown in Figure 6.1 provides vital information with regard to the type of surface damage under different slip regimes. The map reveals that at high contact pressure the transition occur at slip amplitudes of around 40 μm. At low contact pressure, typically below 100 MPa, the transition occurs at slip amplitudes approximately below 20 μm.

6.2 Variation of the friction force

Large variations of traction coefficient could be observed during experimental investigations. The traction coefficient varied with the normal force and the slip amplitude. A comparison of stabilised friction loop at 260 MPa nominal contact pressure for different slip amplitudes is shown in Figure 6.2. The analysis shows that the traction coefficient increases gradually with the slip amplitude and attains maximum value under the gross slip condition.

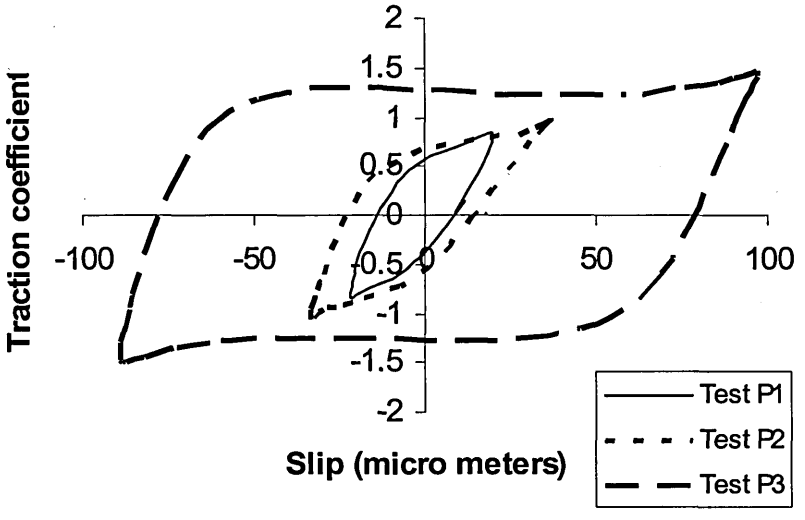

Figure 6.2 – Variation of traction coefficient with slip amplitudes: (260 MPa nominal contact pressure).

The variation of traction coefficient under mixed slip conditions and gross slip conditions was analysed separately. The variation of the traction coefficient with number of loading cycles under mixed slip conditions is shown in Figure 6.3 and the variation under gross sliding is shown in Figure 6.4

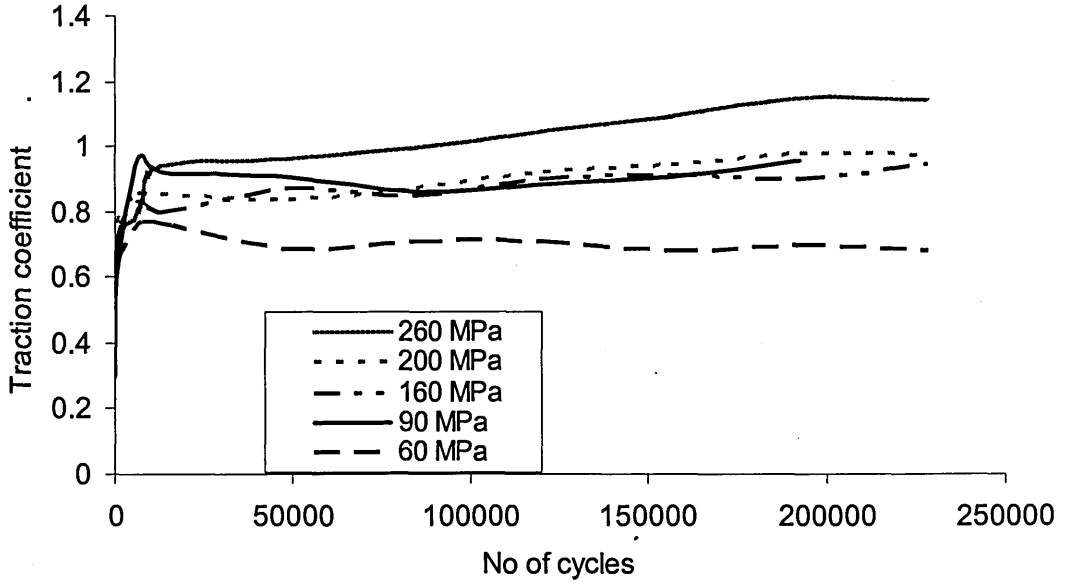

Figure 6.3. Effect of contact pressure on evolution of friction under mixed slip.

Figure 6.3 reveals that the traction coefficient stabilises at around 10,000 to 50,000 cycles. The highest traction coefficient was observed for the highest nominal contact pressure 260 MPa and the lowest stabilised traction coefficient was observed for the lowest nominal contact pressure which is 60 MPa. At 260 MPa nominal contact pressure the stabilised traction coefficient was found to be approximately 1.1 whereas at 60 MPa nominal contact pressure the stabilised traction coefficient dropped down to approximately 0.7.

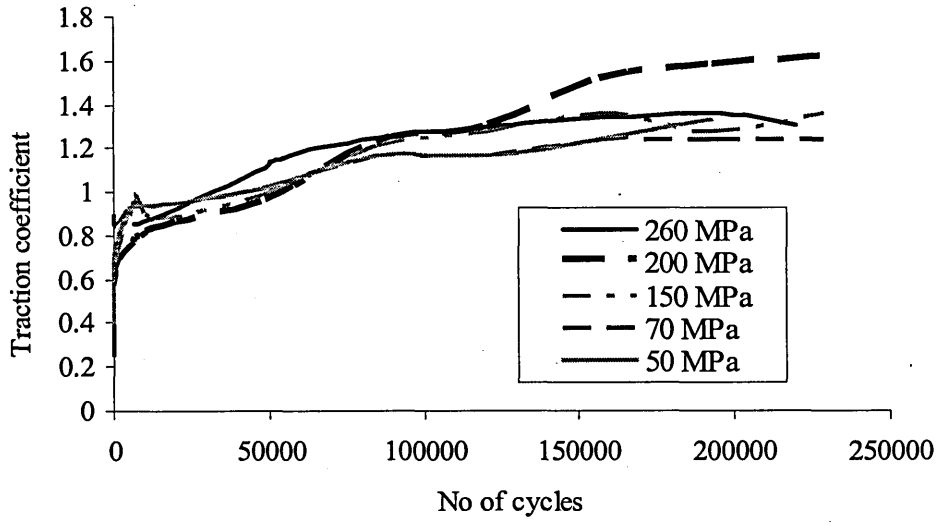

Figure 6.4-. Evolution of friction for different nominal contact pressure in gross slip

The evolution of the coefficient of traction during testing under gross slip for different nominal contact pressures is shown in Figure 6.4. Generally, the traction coefficient varied in the range of 1.2 to1.5 under the gross slip condition.

It was observed that, at the beginning of an experiment with a new fretting pad and specimen, the traction coefficient always started at a lower value (around 0.3 -0.4) and the value stabilised after approximately 10,000 cycles, as shown in Figure 6.5.

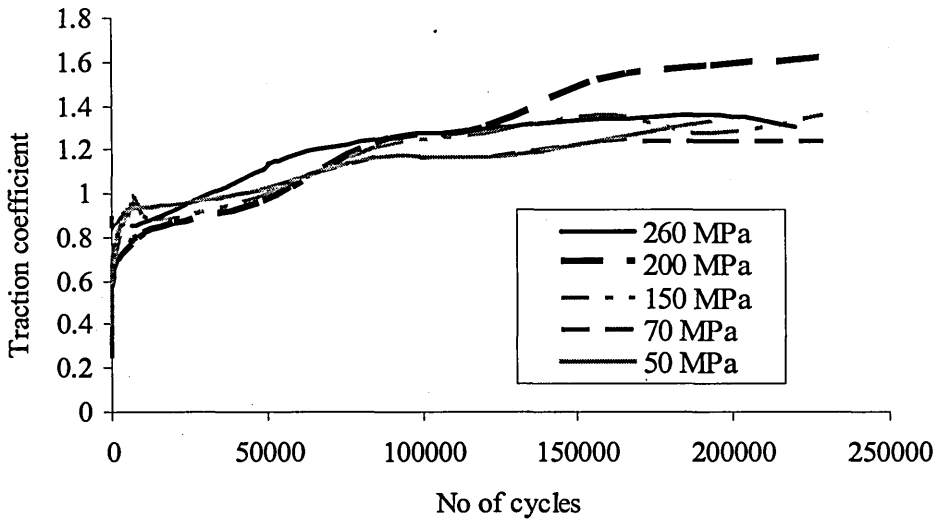

Figure 6.4-. Evolution of friction for different nominal contact pressure in gross slip

The evolution of the coefficient of traction during testing under gross slip for different nominal contact pressures is shown in Figure 6.4. Generally, the traction coefficient varied in the range of 1.2 to1.5 under the gross slip condition.

It was observed that, at the beginning of an experiment with a new fretting pad and specimen, the traction coefficient always started at a lower value (around 0.3 -0.4) and the value stabilised after approximately 10,000 cycles, as shown in Figure 6.5.

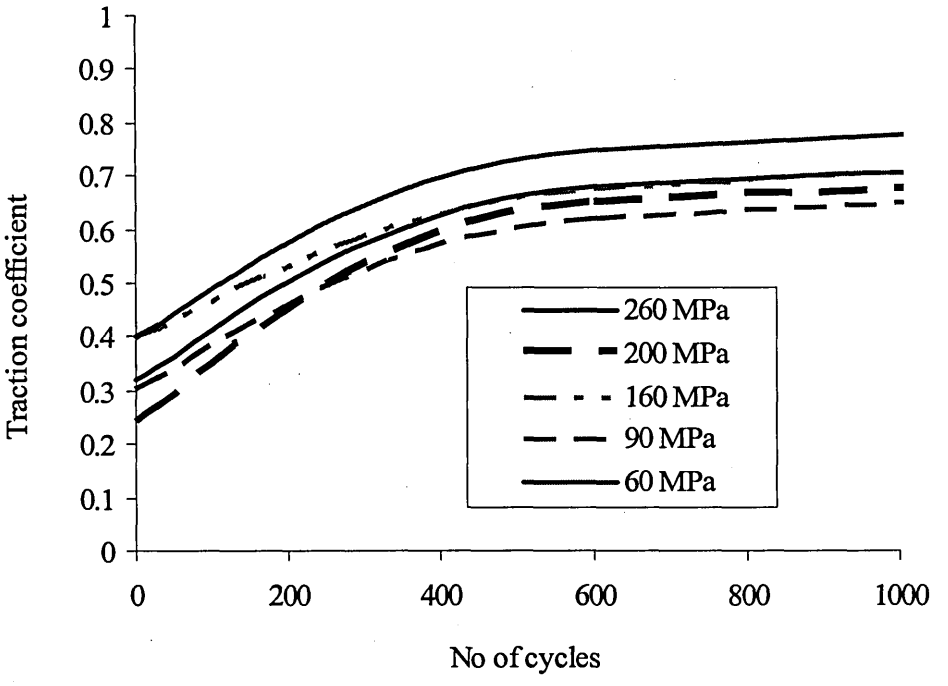

Figure 6.5 -Variation of friction force with number of cycles

The lower value of friction in the early stage of the experiment was explained by the existence of an oxide film on the surface of the material which has a lubricating effect. After this layer is disrupted by fretting action after a few thousand loading cycles, the traction coefficient reaches a maximum value for the particular slip amplitude and nominal contact pressure.

The variation of the stabilised maximum traction coefficient for a range of slip and nominal pressure conditions is shown in Figure 6.6. This figure suggests that there is a maximum value of traction coefficient of approximately 1.5; this is considered to be the coefficient of friction of the damaged surface under gross slip. The lower values of traction coefficients were observed for mixed slip. The maximum value of traction coefficient was found to be independent of the magnitude of the normal load.

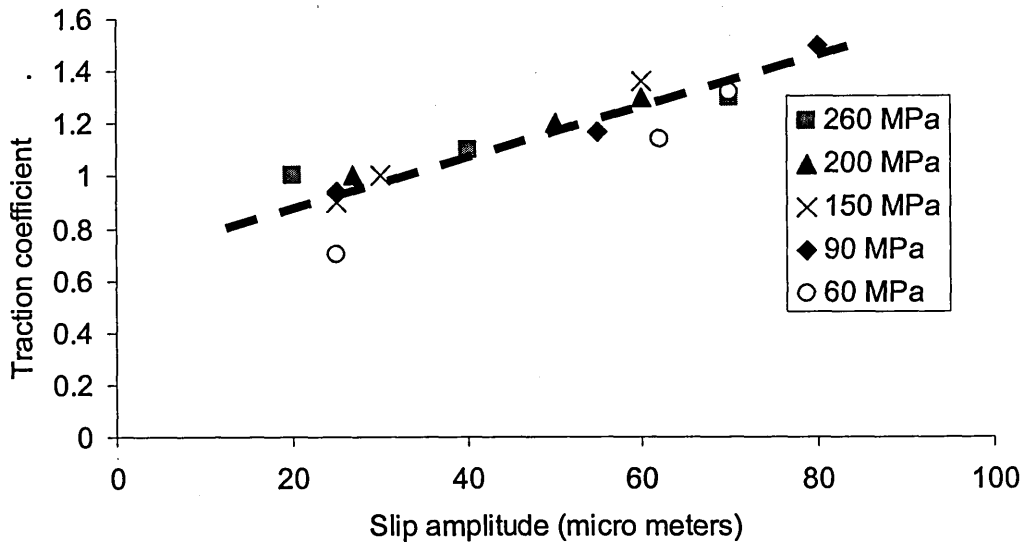

Figure 6.6.- Variation of stabilised traction coefficient with the slip amplitude.

6.3. Wear profiles under different slip conditions

The wear profiles were examined during the preliminary experimental programme. At constant contact pressure, a low rate of wear was observed at low slip amplitudes compared to high slip amplitudes at the same contact pressure.

In the current experimental investigation, experiments were carried out with mixed slip and gross slip conditions and the global sliding condition was distinguished by observing the shape of the friction loop. The analysis of the fretted valley profile provides evidence of the existence of a stick region on either side of contact close to the edge of contact. A comparison of fretted valley profiles for a mixed slip regime and a gross slip case for nominal contact pressure 150 MPa is given in Figure 6.7.

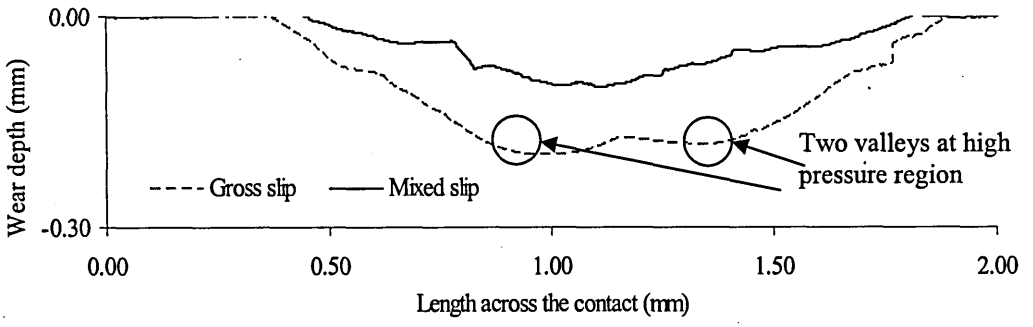

Figure. 6.7 - The comparison of the fretted valley profile under mixed slip and gross slip: (200 MPa contact pressure)

Analysis of Figure 6.7 shows that the rate of wear is very high under gross slip conditions compared to the mixid slip conditions for the same nominal contanct pressure. Two deep valleys could be observed in the gross slip profile at either side of the contact region where peak pressure exist (refer to the pressure distribution shown in figure 5.11). In contrast to this, no deep valleys could be observed in the mixed-slip regime. A similar pattern was observed for tests carried out with 200 MPa, 160 MPa 90 MPa and 60 MPa nominal contact pressures as shown in Figure 6.7, to Figure 6.10.

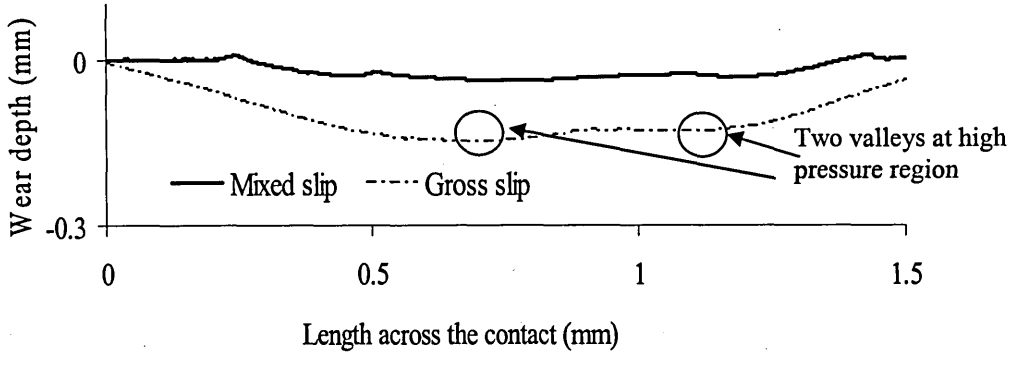

Figure. 6.8 – The comparison of the fretted valley profile in mixed slip and gross slip: (160 MPa contact pressure).

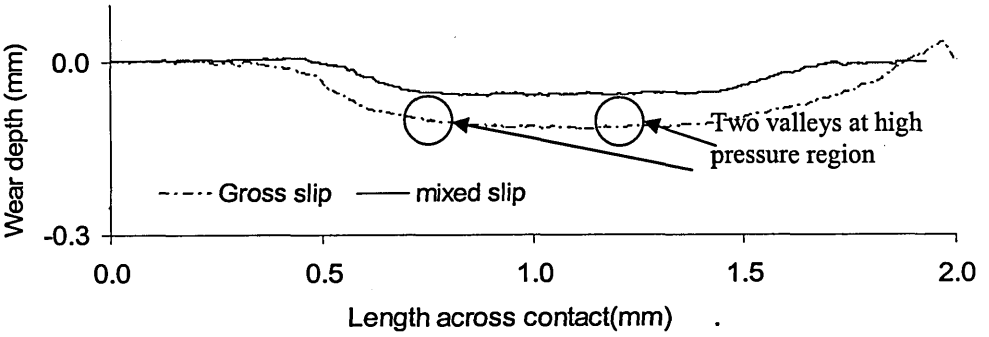

Figure. 6.9 - A comparison of the fretted valley profile in mixed slip and gross slip at 90 MPa contact pressure

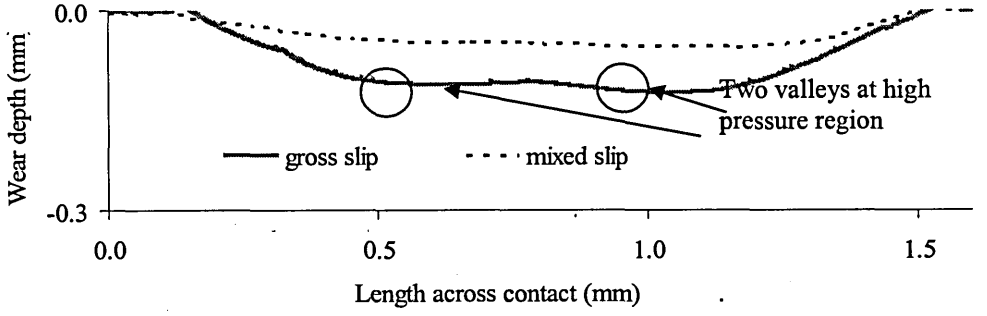

Figure. 6.10 - A comparison of the fretted valley profile in mixed slip and gross slip at 60 MPa contact pressure

The observation of two valleys in the gross slip region can be explained by the highest wear rate occurring in the high contact pressure regions at the edges of contact. In the middle section with low contact pressure, a peak was observed under gross slip condition. In contrary to this, a peak was observed in either side of the contact region under mixed slip condition.

The existence of a peak in wear profile even in the region where a high contact pressure region, can be explained using the slip condition. The results suggests that there exists a stick regions in the peak contact pressure regions for the mixed slip sliding regime and the wear rate is less in the mixed slip regime compared the gross slip condition.

Analysis of the wear profile reveals that, although in the experimental set-up the global slip and the contact pressure between the specimen and the pad was controlled, the local slip condition at any point along the contact is influenced by the contact pressure distribution. For example, the regions of low contact pressure would slip before the regions of high contact pressure assuming equal shear traction. Therefore different slip regimes may occur along the contact depending on the magnitude of the global slip.

From the above analysis, three different slip conditions were identified as stick, mixed slip and gross slip, for the current tests. They are schematically illustrated in Figure 6.11 to 6.13 respectively.

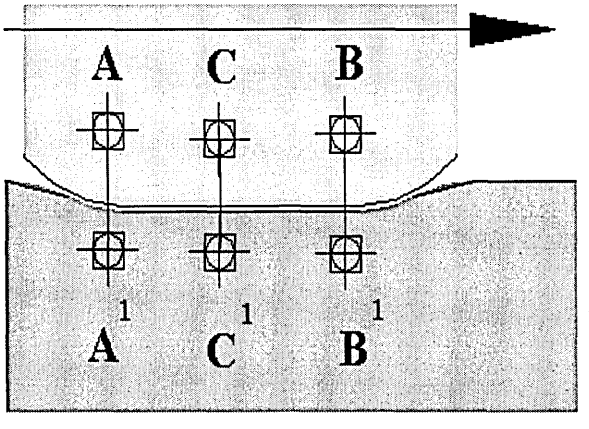

Figure 6.11 - Stick condition

For small global slip the complete contact region is under stick. In this regime, the pad displacement occurs due to microscopic elastic displacements between the pad and the specimen due to the deformation of local asperities on mating surfaces. This regime is predominant at very high contact pressures and, at low global slip amplitudes typically below 15 μm.

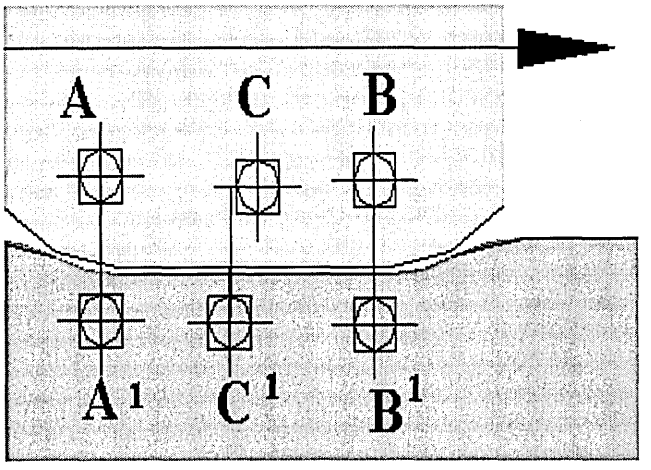

Figure 6.12 - Mixed slip condition

An increase in the global slip amplitude would make the middle region, where the contact pressure is lowest, slip, whilst the two end regions A and B remain in stick. Further increase in the global slip would create slip in the region B and not in the region A. This condition is denoted as mixed slip.

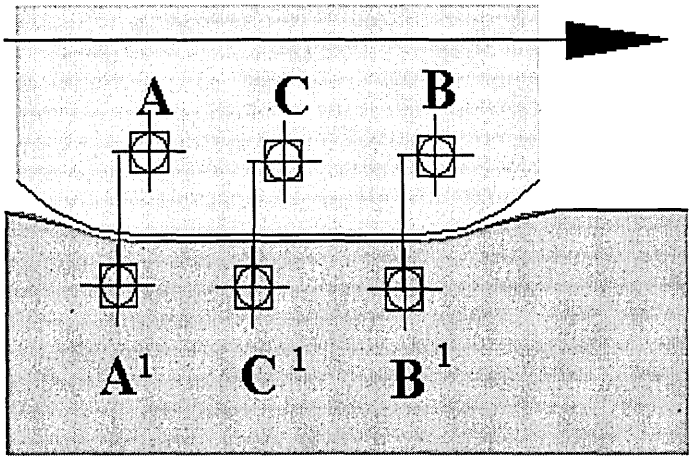

Figure 6.13 - Gross slip condition

Finally the whole contact may be subjected to relative slip and this situation is known as gross slip. This regime is typical with high global slip amplitudes typically above 60 μm. The slip regimes mentioned are characterised by the shape of the friction loop and the typical shape of the friction loop for each condition was presented in Chapter 2.

6.4 Variation of Wear Depth

The variation of maximum wear depth of the scar of each test against the slip amplitude is shown in Figure 6.14. A strong influence of slip amplitude and the nominal contact pressure on the wear depth was observed.

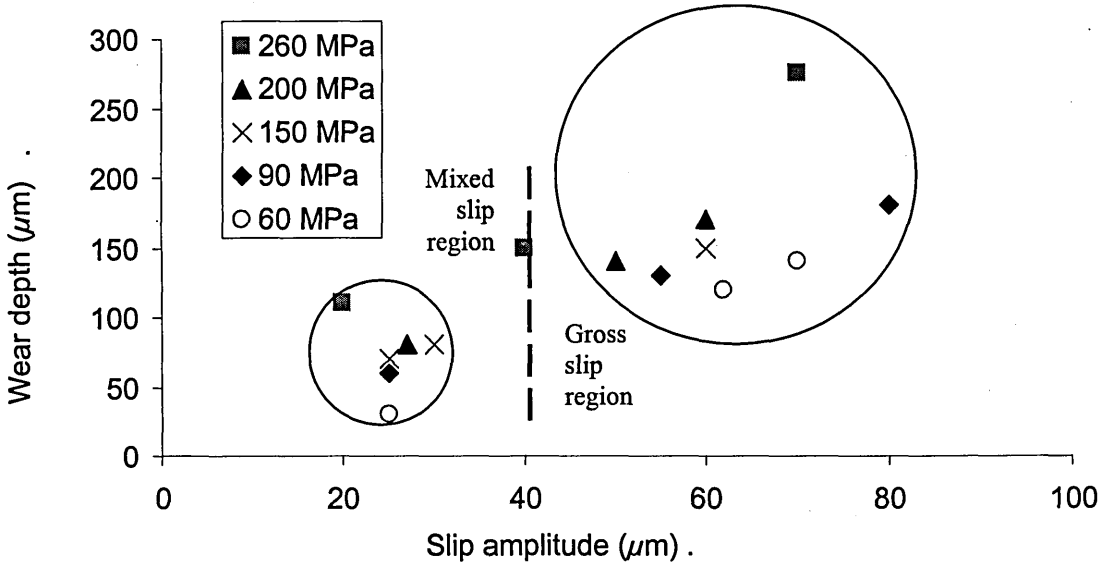

I

Figure 6.14. Variation of wear depth with slip amplitude

The wear depth was found to increase with increasing slip amplitude and normal load.

6.5 Surface cracks

During the preliminary experimental investigations, surface cracks were observed only at high contact pressure under the mixed slip condition. Under gross slip conditions, a deep surface wear scar was observed without surface cracks. The loading region where the cracks were observed in the preliminary test series is depicted in Figure 6.15.

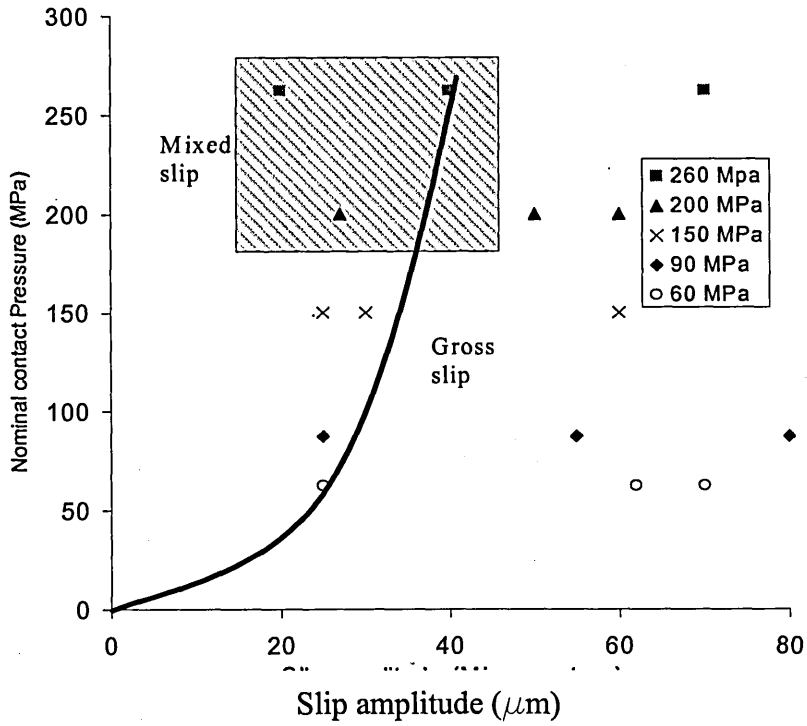

Figure 6.15 – The loading region for fretting cracks

Cracks were observed at 260 MPa and 200 MPa nominal contact pressure, under the mixed slip condition. The cracks observed at 260 MPa, with 20 μm slip amplitude (Test P1) are shown in Figure 4.35. The cracks observed for the same nominal contact pressure at 40 μm (Test P2) are shown in Figure 4.36 and the cracks observed at 200 MPa at 27 μm (Test P4) are shown in Figure 4.38. In all three tests (Test P1, P2 and P4) two cracks were observed at each end of contact. Both cracks were inclined while the left side crack was shorter than the right side.

The difference of crack length can be explained using the contact pressure distribution as the peak contact pressure in the left hand side is less compared to the peak pressure at right hand side. The general trend path observed in these investigations is depicted in Figure 6.16.

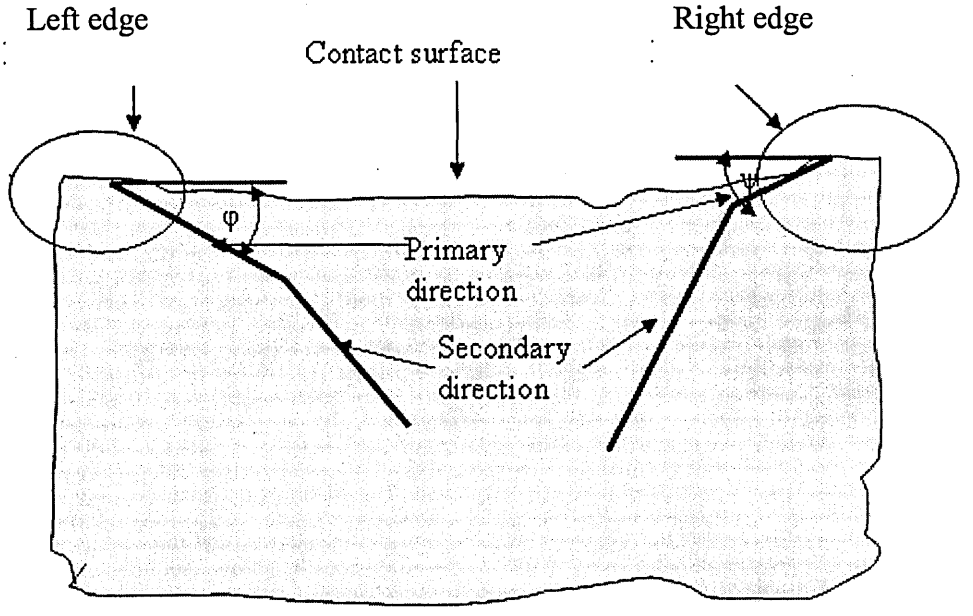

Figure 6.16 – The general trend of the crack path observed in the preliminary experimental investigations.

The analysis of crack path observed in the preliminary experimental investigation show that the crack path changes direction after moving about 10 μm to 20 μm from the surface. The cracks at both the left and right edges initiated at approximately the same angle to the surface $(\varphi \approx \psi)$. The crack at the left edge was longer compared to the right edge during the initial stage. Both cracks were kinked and the secondary directions of the crack tip are approximately the same. The total depth of the crack at the right edge was greater than that of the crack at the left edge.

6.6 Numerical analysis and perdition of the crack path

In order to understand and explain this behaviour and to assess the crack path, the sub surface stress state was analysed and a critical plane based numerical methodology was developed. The numerical procedure was presented in Chapter 4.

In the numerical analysis, à severity parameter was introduced in order to ascertain whether the crack at any point (from the initiation to the final failure or crack arrest at a certain depth) is governed by the mode I cracking or mode II cracking. The results of the analysis (for mode I and mode II and prediction of the crack path) for test P2 are summarised in Tables 6. 1 and 6.2.

	Mode II parameter				Mode I parameter			
Depth (μm)	$\sigma_{n\,Max}$	$\Delta\gamma$	ψ	$\sqrt{3}(\Delta\tau + K\sigma_{Max})/\sigma_y$	$\sigma_{n\,Max}$	$\Delta\varepsilon$	ξ	σ_{nMax}/σ_y
1	608	0.017	40	3.9	1893	0.023	15	2.1
5	357	0.013	40	2.7	1181	0.017	15	1.3
10	157	0.009	40	1.8	734	0.012	25	0.8
15	-463	0.007	70	0.3	556	0.01	25	0.6
20	-438	0.006	70	0.22	455	0.008	25	0.5
25	-421	0.006	70	0.13	391	0.007	25	0.4
30	-426	0.005	70	0.06	349	0.006	25	0.3

Table 6.1 – predictions of severity parameter for the left corner: Test P2

Mode II parameter					Mode I parameter			
Depth (μm)	$\sigma_{n\,Max}$	$\Delta\gamma$	ψ	$\sqrt{3}(\Delta\tau+K\sigma_{Max})/\sigma_y$	$\sigma_{n\,Max}$	$\Delta\varepsilon$	ξ	σ_{nMax}/σ_y
1	**475**	**0.0195**	**40**	**3.9**	2058	0.029	15	2.2
5	**262**	**0.013**	**40**	**2.5**	886	0.0159	20	0.98
10	-574	0.0089	70	0.2	**564**	**0.012**	**25**	**0.62**
15	-462	0.0083	70	0.4	**456**	**0.008**	**25**	**0.5**
20	-397	0.0071	70	0.3	**401**	**0.007**	**25**	**0.44**
25	-353	0.0063	70	0.3	**391**	**0.007**	**25**	**0.43**
30	-320	0.0053	70	0.2	**349**	**0.006**	**25**	**0.38**
35	-324	0.0054	70	0.2	**318**	**0.006**	**25**	**0.35**

Table 6.2 – predictions of severity parameter for the right corner: (Test P2)

Where, $\Delta\gamma$ is the maximum shear strain range, $\Delta\varepsilon$ is the maximum normal strain range, $\sigma_{n\,Max}$ is the maximum normal stress, ψ is the angle of the mode II crack path with vertical direction, ζ is the angle of the mode I crack path with vertical direction

The results of the severity parameter at the left corner show that the influence of the mode II is dominant when the crack is closer to the surface. The initial angle of the crack path is 40^0 with the normal to the surface.

After growing approximately 15 μm the shear crack path changes towards the surface (70^0) and at this point the maximum normal stress amplitude on the mode II plane is compressive. According to the severity parameter at this point, the crack propagation is more dominant by mode I and the crack follows the mode I path.

Analysis of the results at the right edge show that same influence of mode II cracking at the right edge is less than at the left edge. The severity comparison suggests that the mode II influence is approximately 10 μm deep and the crack follows a mode I crack path beyond 10 μm.

The crack path prediction using the severity parameter for the preliminary test series is compared with the actual crack path observed experimentally, in Figure 6.17 through Figure 6.22.

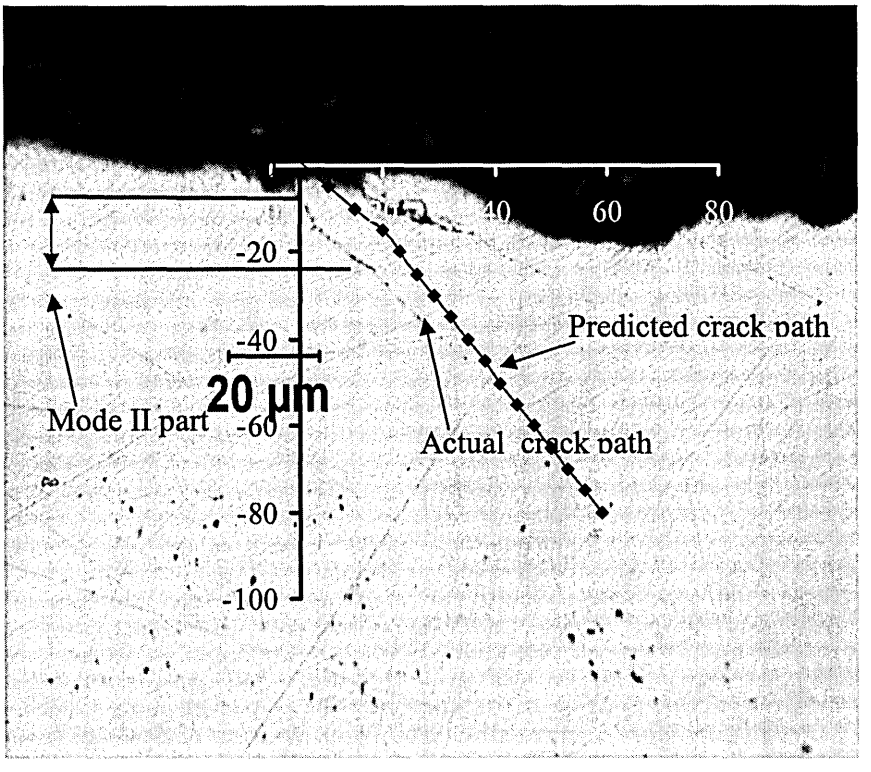

Figure 6.17 Prediction of crack path using severity parameter (test P2 left edge)

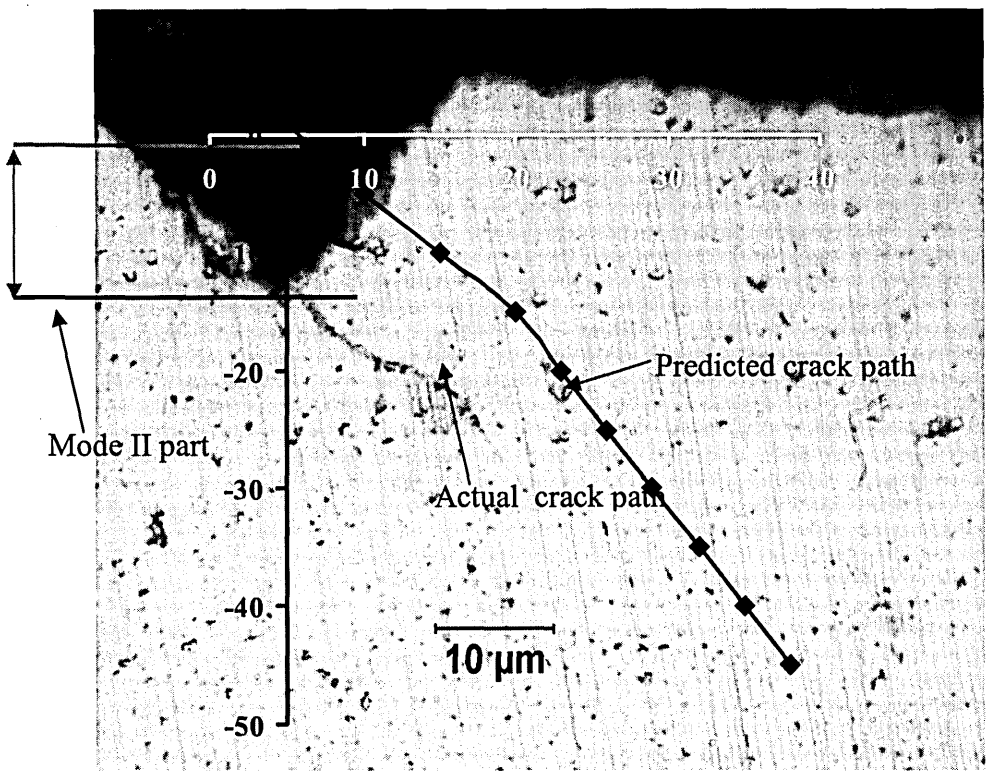

Figure 6.18 Prediction of crack path using severity parameter (test P1 left edge)

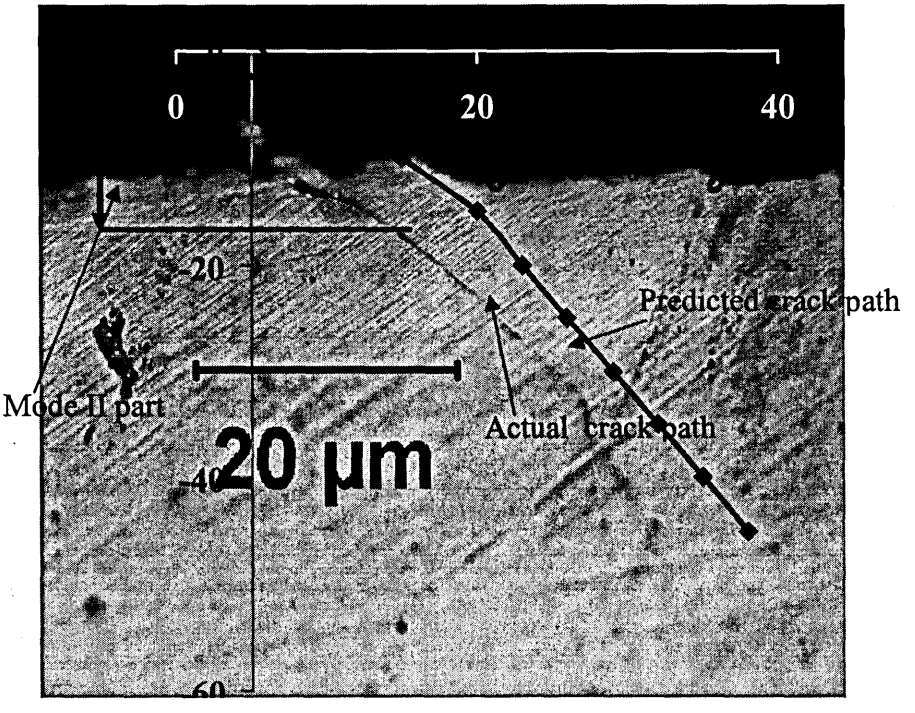

Figure 6.19- Prediction of crack path using severity parameter (test P4 right edge)

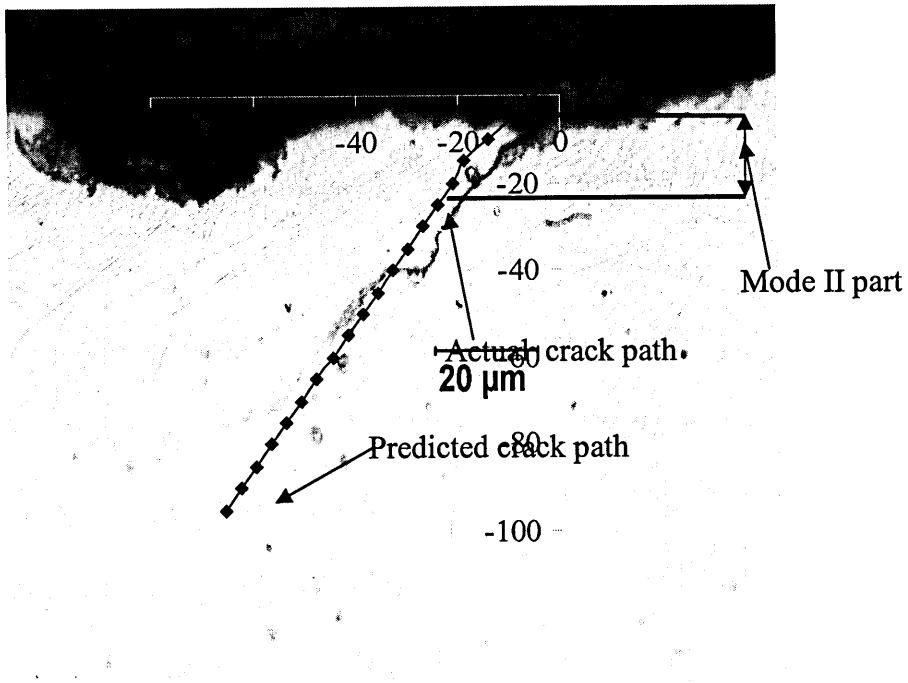

Figure 6.20 - Prediction of crack path using severity parameter (test P2 right edge)

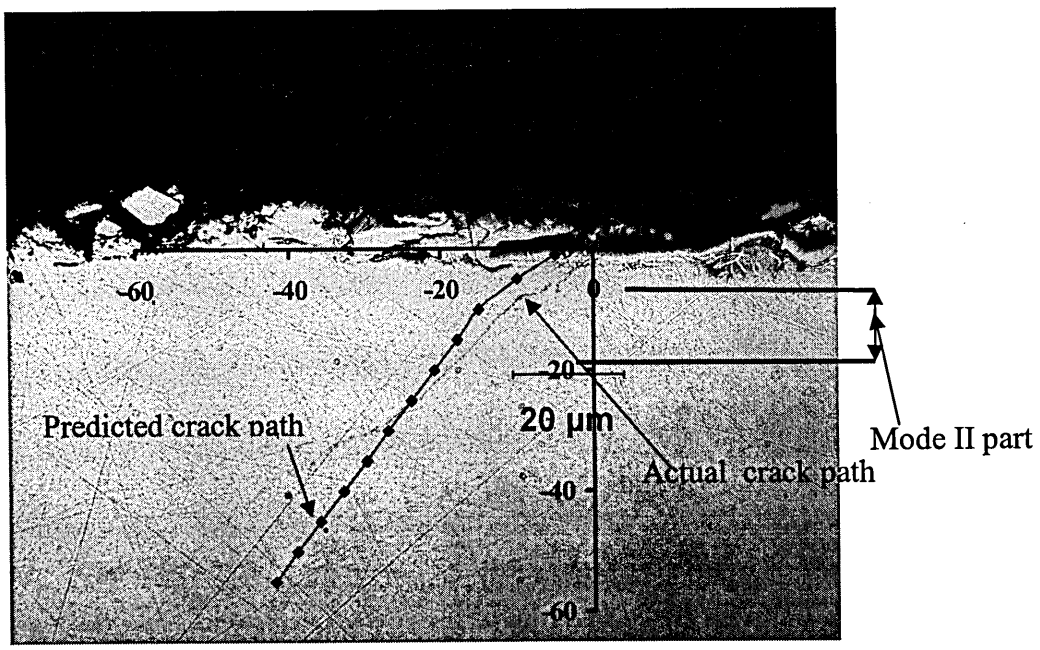

Figure 6.21- Prediction of crack path using severity parameter (test P4 right edge)

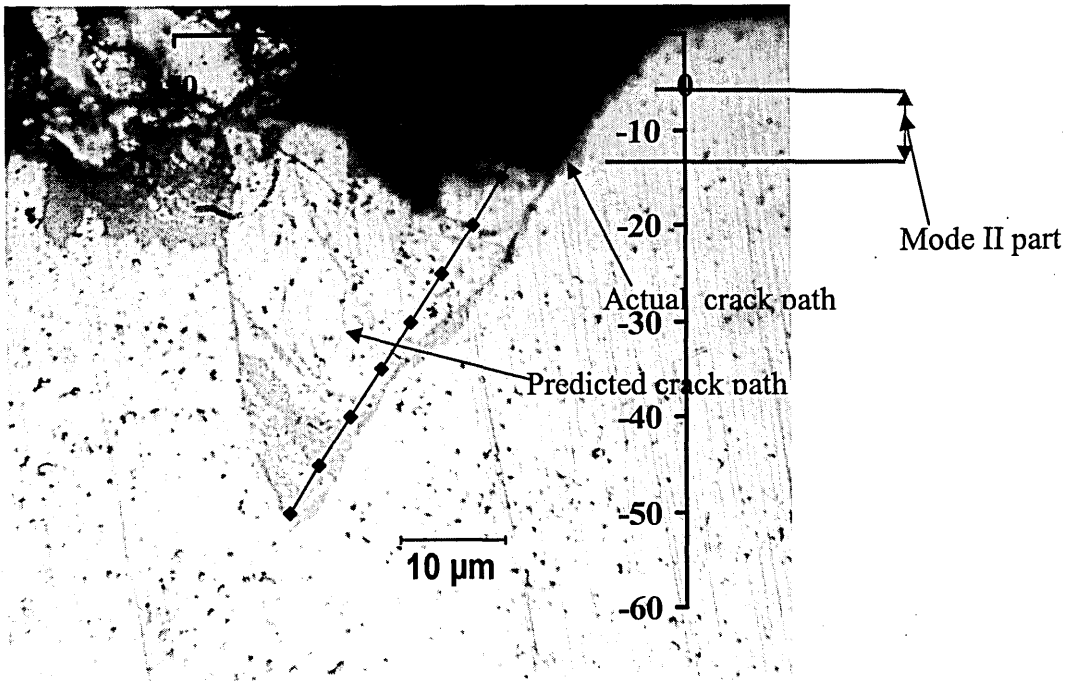

Figure 6.22- Prediction of crack path using severity parameter (test P1 right edge)

6.7 Crack nucleation behaviour during interrupted test programme (series I)

The envelope where fretting originated cracks could be observed was defined in Figure 6.15. This envelope was further investigated during the interrupted test series and the details of the interrupted test series together with the predicted crack path are discussed below.

The interrupted tests revealed that at constant normal contact load, the observable cracks appear after certain numbers of cycles and the lengths of these cracks depend on the nominal contact pressure. Figure 6.23 depicts results of all the tests carried out with the mixed slip condition.

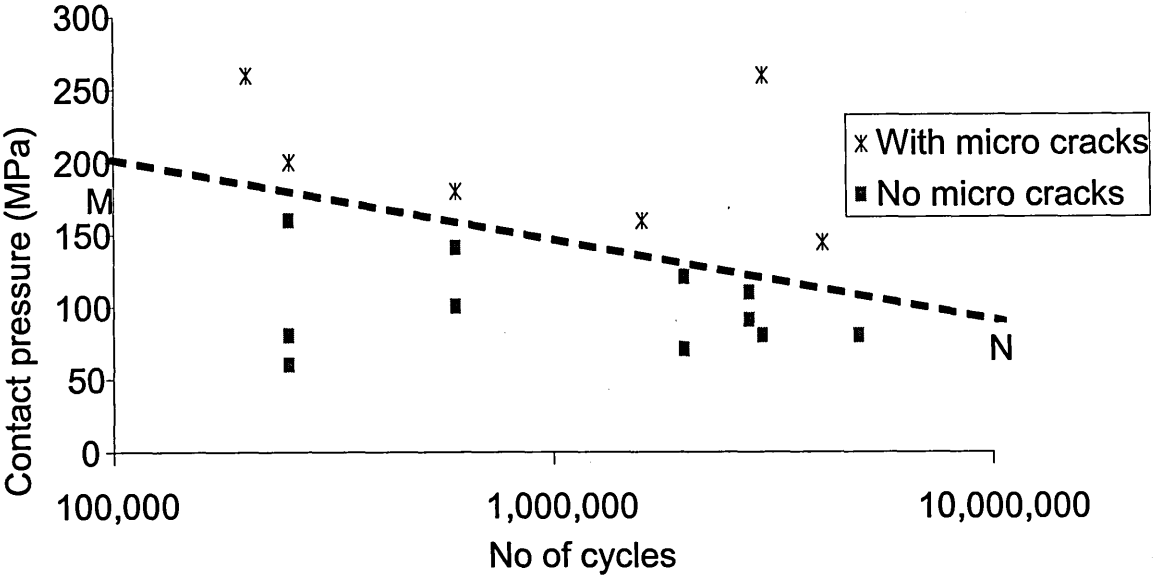

Figure 6.23 - Crack nucleation boundary

From these results, a boundary could be drawn where fretting originated surface cracks could be observable and the boundary is shown in Figure 6.23. Figure 6.24 to 6.26 depicts the actual crack and the crack path predictions for Test I 12, Test I 3 and Test I 4 .

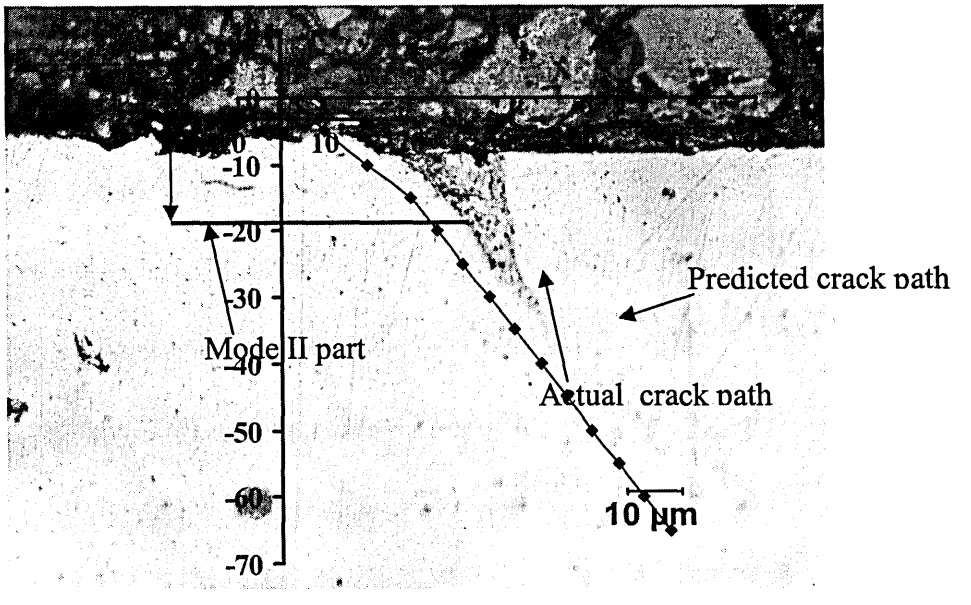

Figure 6.24 Prediction of crack path using severity parameter: (test I 12 left corner)

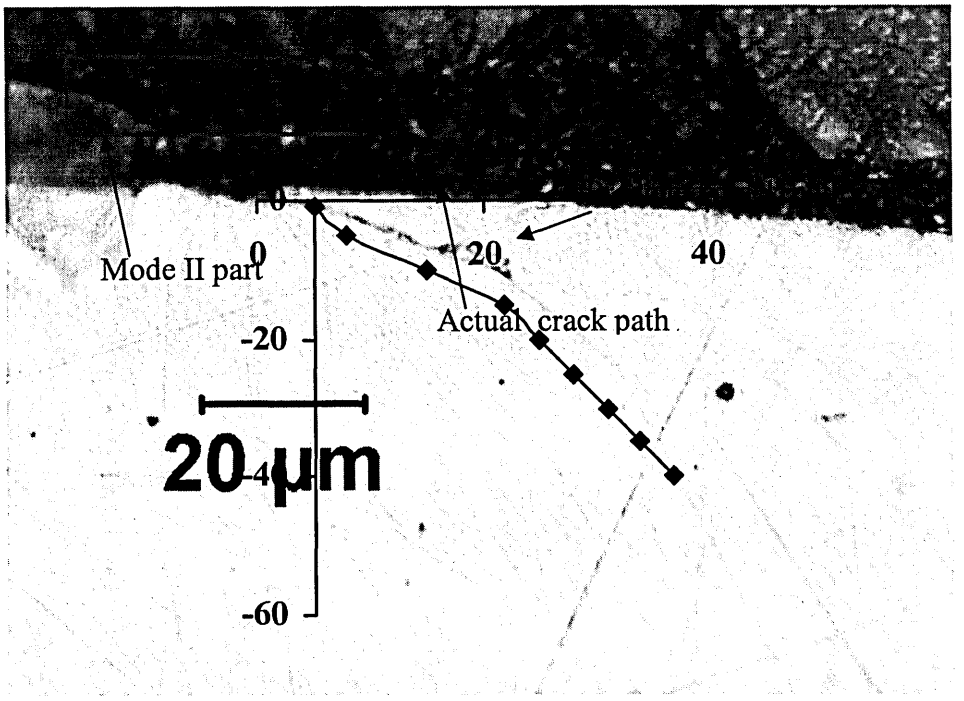

Figure 6.25 - Prediction of crack path using severity parameter: (test I 3 left corner)

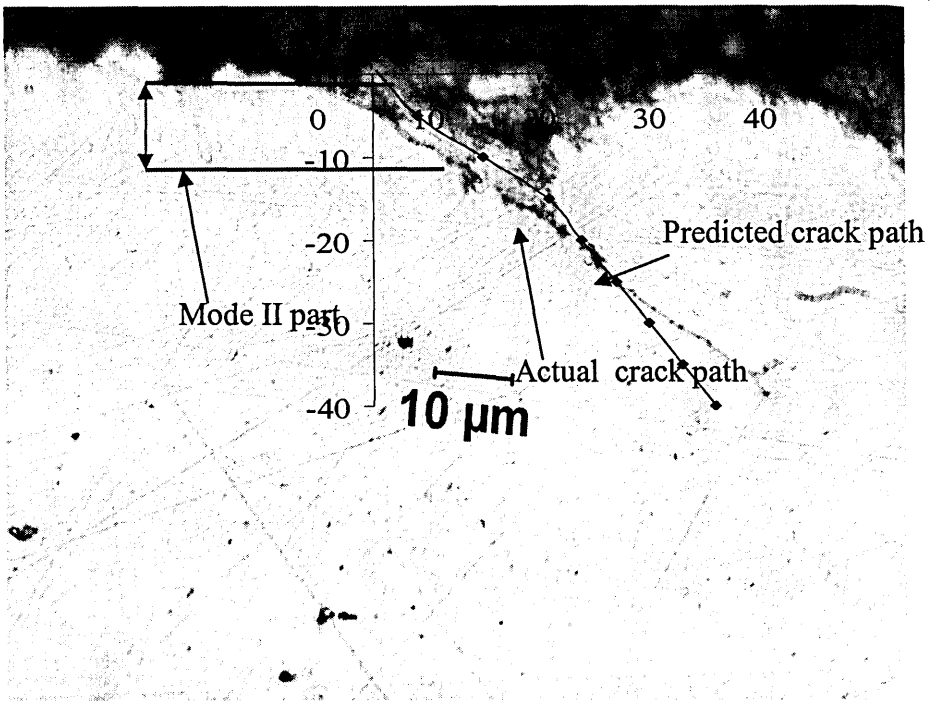

Figure 6.26 Prediction of crack path using severity parameter: (test I 4 left corner)

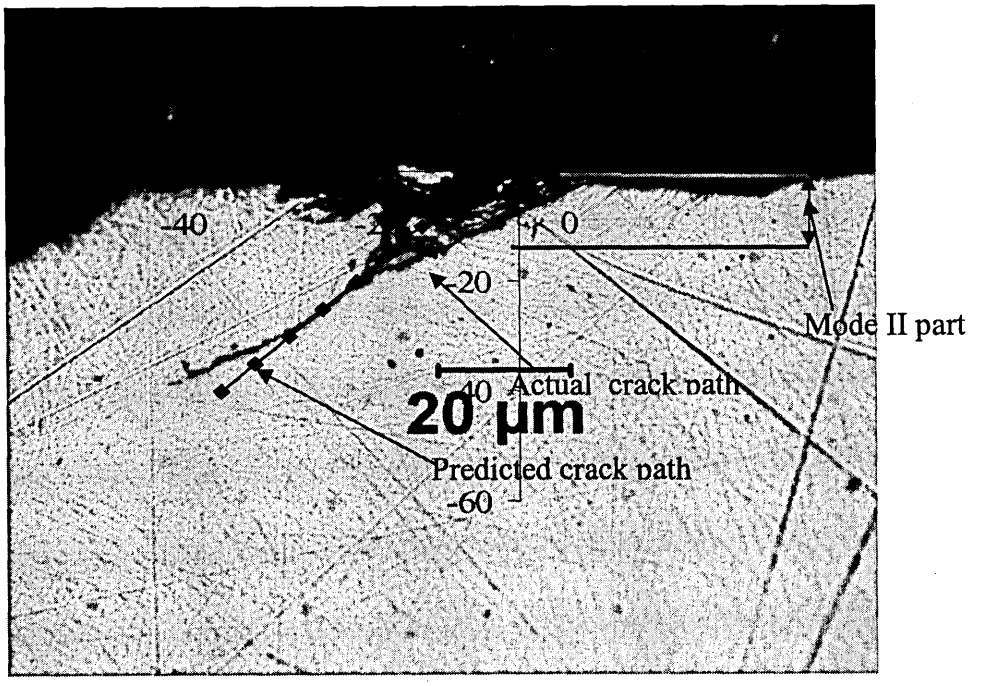

Figure 6.27 Prediction of crack path using severity parameter: (test I 3 right corner)

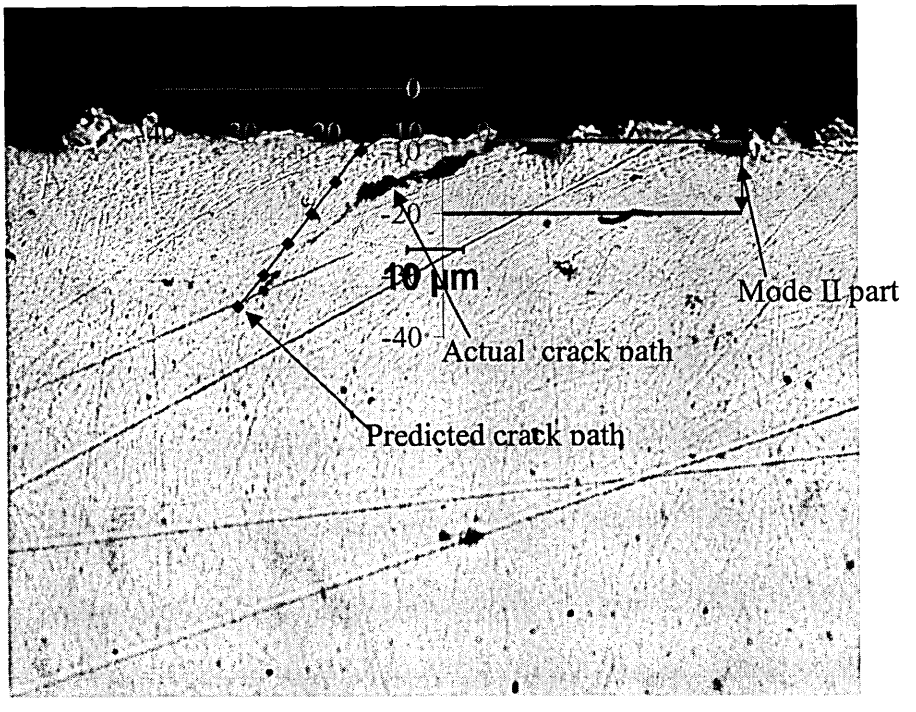

Figure 6.28 Prediction of crack path using severity parameter: (test I4 right corner)

6.8 Life prediction

The relationship between crack growth and number of loading cycles was predicted based on the fracture mechanics concept described in Chapter 5. The crack propagation life for the left and right edges predicted by this method are shown in Figure 6.29 and 6.30, respectively.

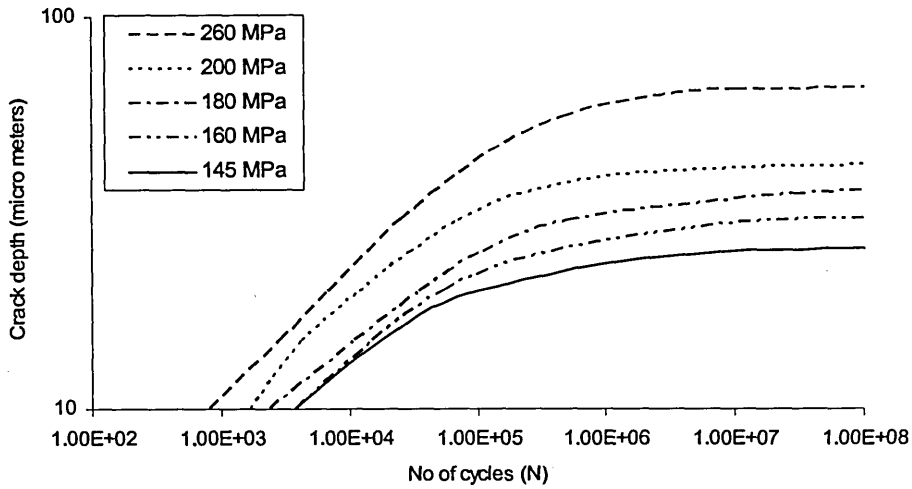

Figure 6.29 – Prediction of crack depth at the left edge.

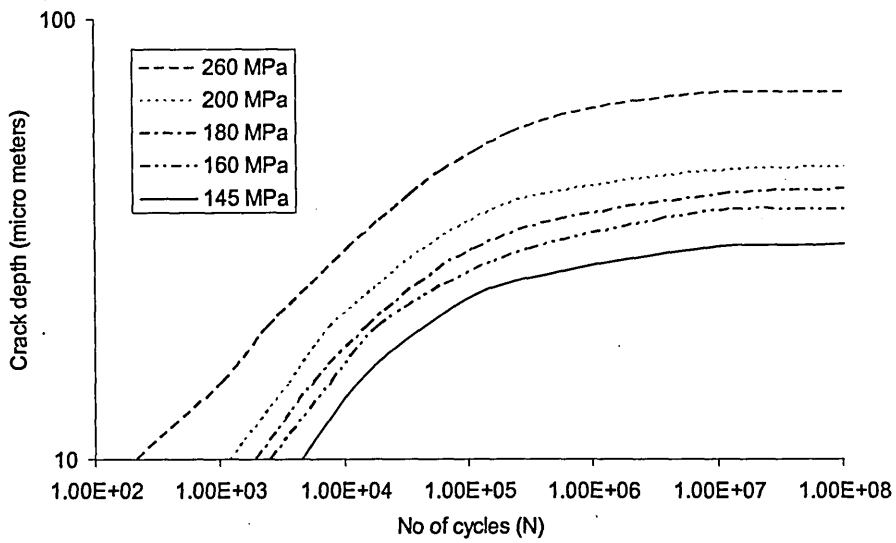

Figure 6.30 – Prediction of crack depth at the right edge.

The analysis shows that all tests analysed within the nominal contact pressure range from 145 MPa up to 260 MPa nominal contact pressure, should arrest resulting in non-propagating cracks. According to the analysis, cracks with 260 MPa nominal contact pressure would arrest at approximately 65 μm depth at left edge (1 mm corner radius) and at approximately 70 μm depth at the right edge (0.5 mm corner radius). Further the analyses showed that the cracks in all test conditions reach the maximum length and arrest approximately around 10 million loading cycles.

6.9 Depth of crack arrest.

The range of stress intensity factor of the left edge crack for the 260 MPa and 160 MPa nominal contact pressure cases were compared with the threshold stress intensity factor range to obtain the depth of crack arrest. Figure 6.31 shows that the threshold stress intensity range gradually increases with the crack depth and the stress intensity range gradually decreases with the crack depth. The above analysis was carried out in the absence of a cyclic bulk stress. Further, the Figure 6.31 depicts that the value $\Delta K_{eff} - \Delta K_{effth}$ is lower for the low nominal contact pressure. The condition $\Delta K_{eff} < \Delta K_{effth}$ need to be satisfied in order for the crack to arrest and this was achieved for 160 MPa nominal contact pressure at approximately 30μm crack depth and for 260 MPa nominal contact pressure this was 65μm crack depth.

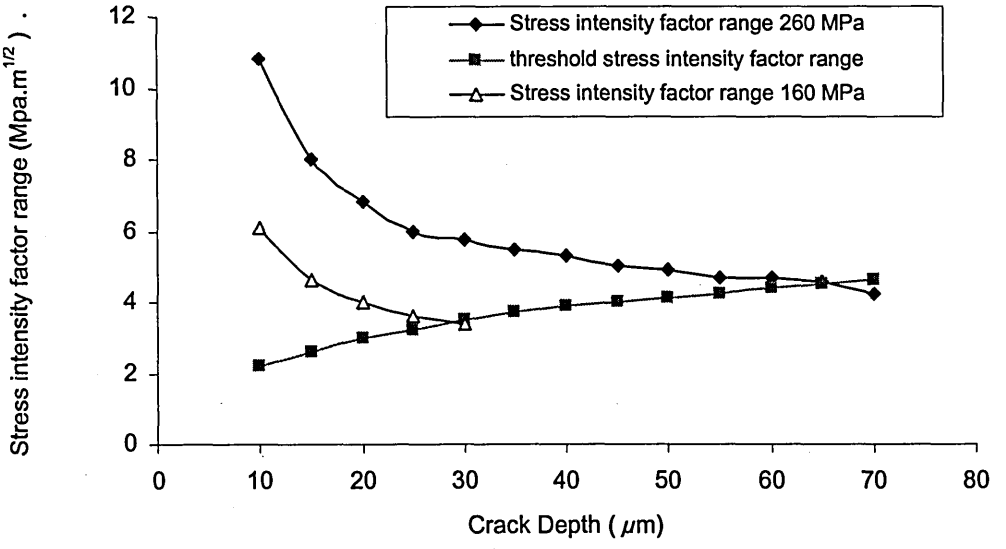

Figure 6.31 – Comparison of ΔK_{eff} and ΔK_{th} with crack length

6.10 Comparison of the crack arrest depth with experimental results.

The experimentally observed crack depths were compared with numerical predictions. The experimental crack depth and the corresponding number of cycles was compared with the numerical predictions in Figure 6.32 and 6.33 for the left and right edges respectively. Good correlation is evident between numerically predicted crack depth and experimentally determined crack depth. A summary of the comparison of experimental and numerical crack depths is presented in Chapter 7.

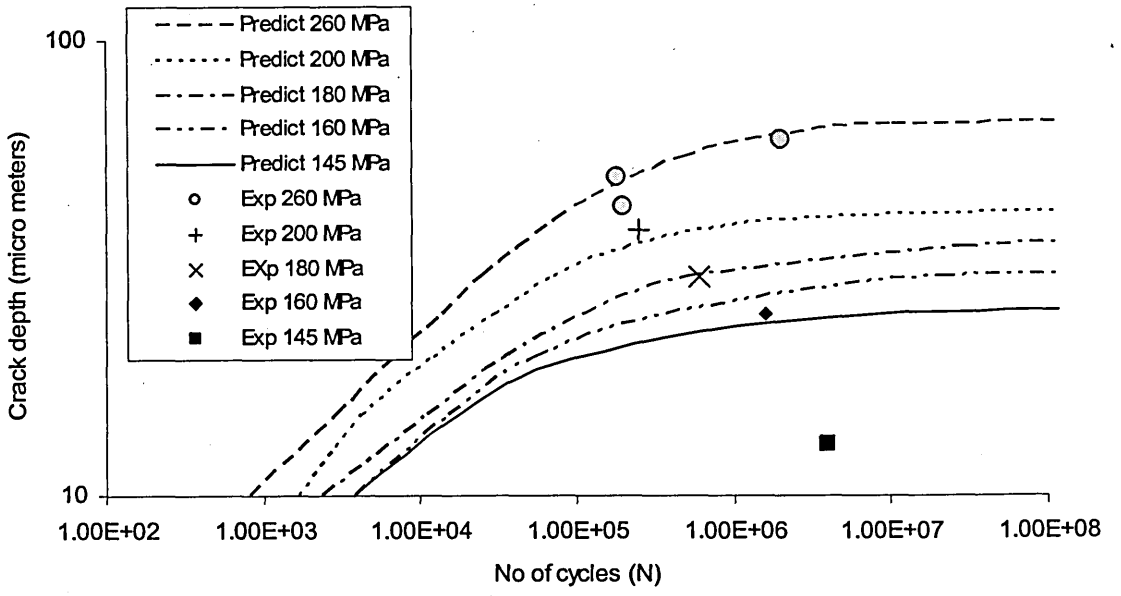

Figure 6.32 – Comparison of numerical and experimental crack propagation behaviour;(left edge).

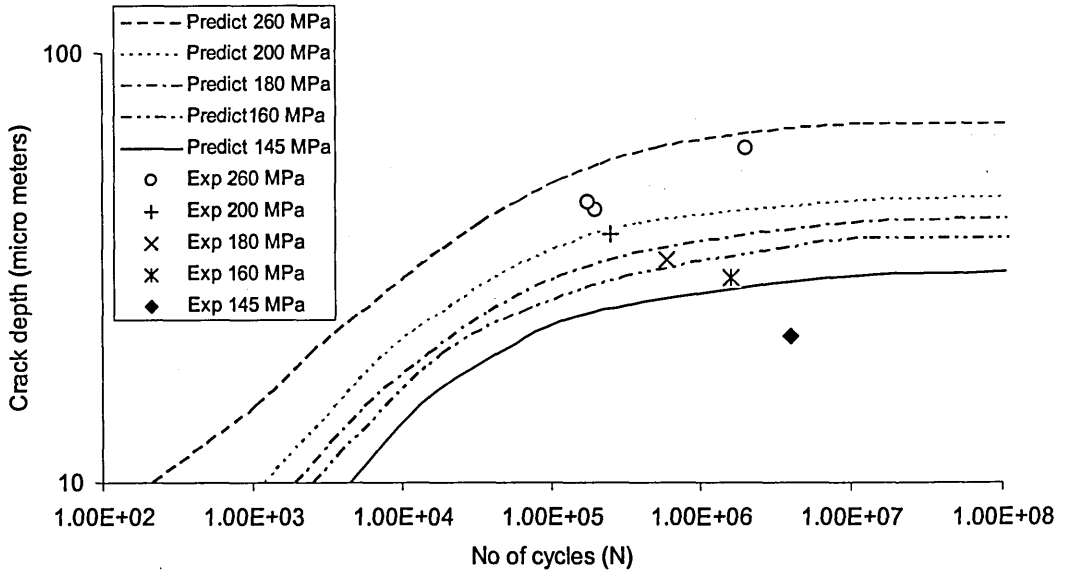

Figure 6.33 – Comparison of numerical and experimental crack propagation behaviour; (right edge)

6.11 Numerical analysis of fretting fatigue

Further, a numerical analysis was carried out to explore the behaviour of crack propagation when a bulk cyclic stress is superimposed in the axial direction (σ_{xx}) of the wire (the cyclic bulk stress is in the same as the fretting sliding direction). The comparison of the effective stress intensity factor range at 260 MPa nominal contact pressure with a 200 MPa cyclic bulk stress amplitude is shown in Figure 6.34.

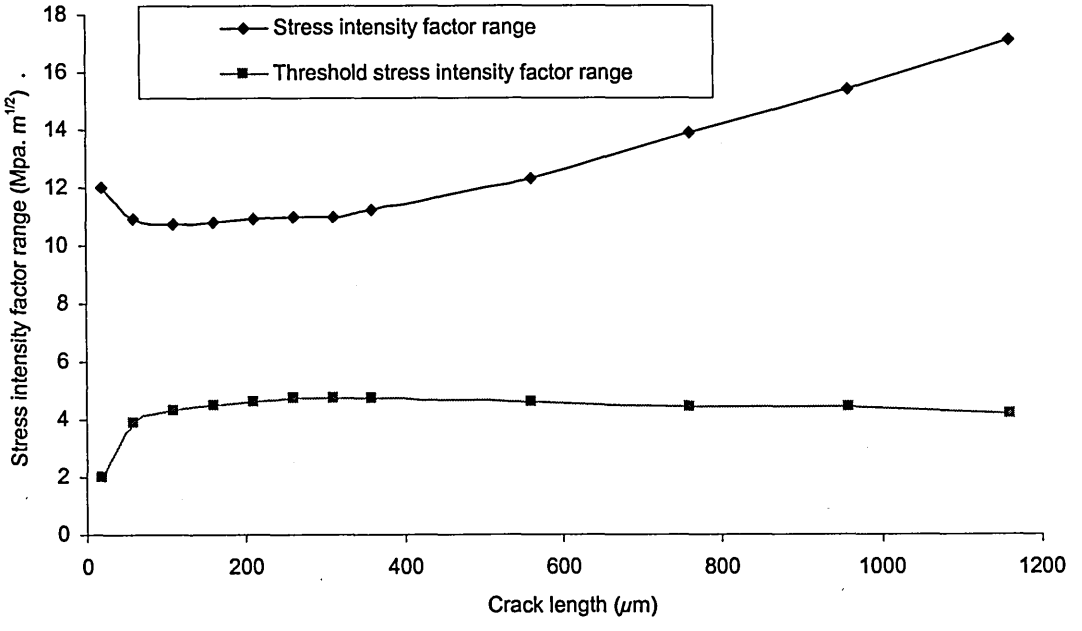

Figure6.34 – Variation of stress intensity factor range and threshold stress intensity factor range (200 MPa bulk stress amplitude in X direction at 260MPa nominal contact pressure)

Although the applied cyclic stress amplitude is only about 50% of the fatigue limit of the pressure armour wire material, the Figure 6.34 shows that the specimen can fail under fretting conditions.

6.11.1 Crack path prediction with superimposed cyclic bulk stress

The crack path was predicted based on the numerical procedure discussed in Chapter 5. The predicted crack path at 260 MPa nominal contact pressure with a 270 MPa cyclic bulk stress amplitude is shown in Figure 6.35.

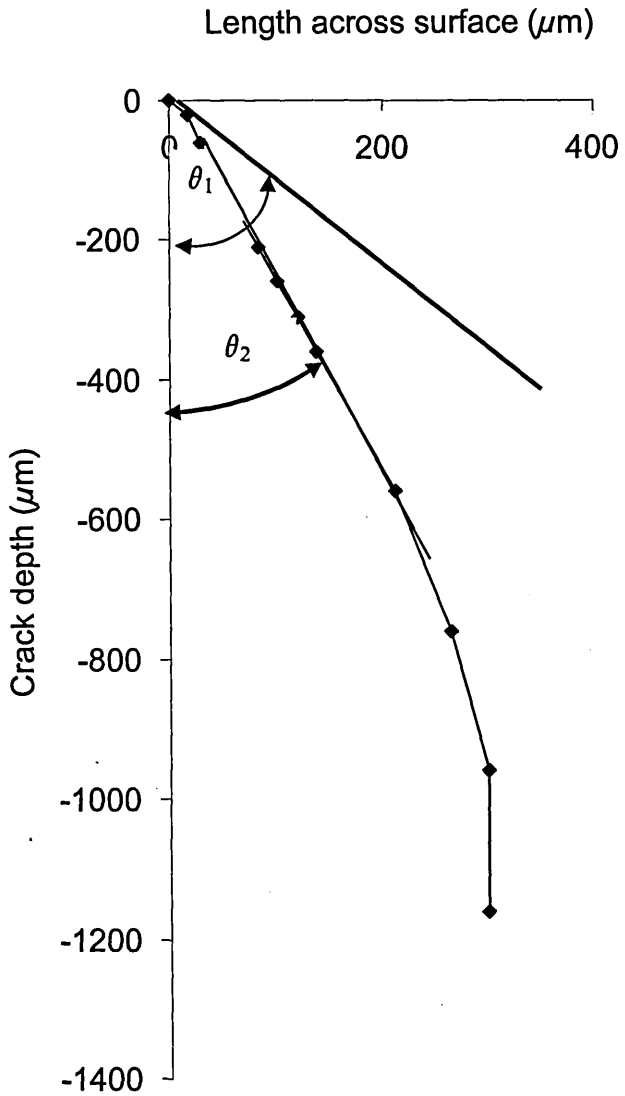

Figure 6.35 - Predicted crack path: (260 nominal contact pressure and 270 MPa cyclic bulk stress).

The crack path (Figure 6.35) shows an initial mode II part of the crack growing approximately to a depth of 20 μm. The mode II part makes an angle (θ_1) approximately 40^0 with the normal direction to the surface . The crack path deviates after the dominant mode changes from mode II to mode I and maintains approximately an angle (θ_2) in the range of 30^0 – 35^0. After the crack propagates about 1-2 mm, the trajectory of the crack changed to almost right angles to the contact surface as the cyclic bulk stress becomes more dominant in crack propagation.

This behaviour of crack path was confirmed by Fernando et al **[94]** and Mutoh and Xu [80]. Prediction and experimental results of Mutoh and Xu **[80]** are shown in Figure 6.36.

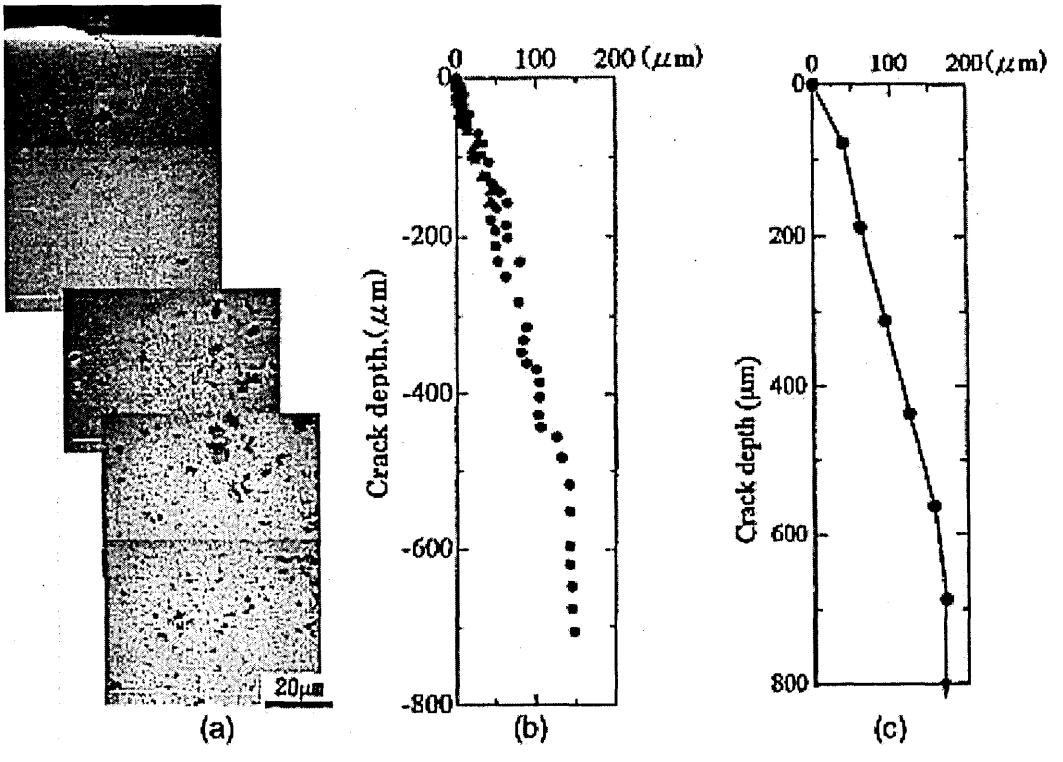

Figure 6.36 - A comparison of predicted and experimental crack path [77]

6.11.2 Crack propagation behaviour with cyclic bulk stress in the sliding direction

The predicted variation of the crack depth with number of cycles for various bulk stress amplitudes at 260 MPa nominal contact pressure is shown in Figure 6.37.

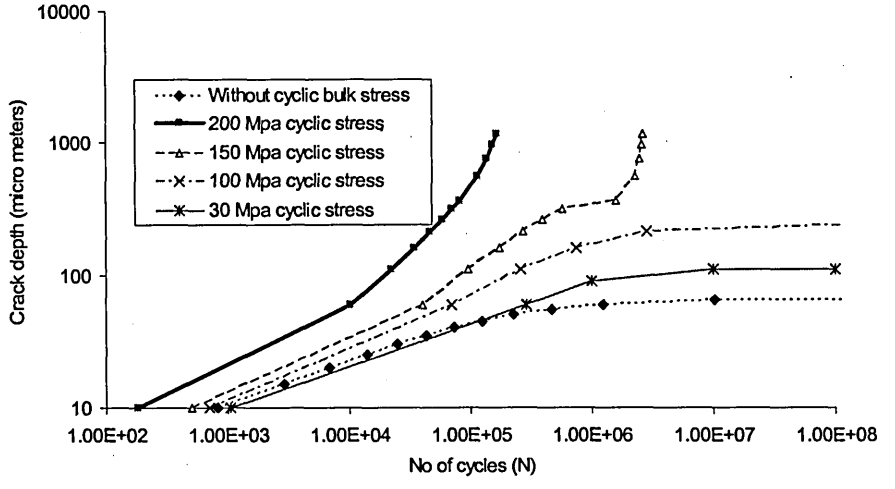

Figure 6.37 – Variation of crack depth with number of cycles for various bulk stress: (260 MPa nominal contact pressure).

According to Figure 6.37, the crack growth rate is highest at 200 MPa bulk cyclic stress amplitude whilst the lowest crack growth rate occurs when the cyclic bulk stress is not applied. The crack growth rate increases with the increase of cyclic bulk stress amplitude. After reaching a certain threshold value of cyclic bulk stress which is specific to a certain nominal contact pressure, the crack grows until catastrophic failure.

Furthermore, this behaviour is confirmed by the analysis shown in Figure 6.38 where, the stress intensity factor range for a range of cyclic bulk stresses from 30 MPa to 200 MPa and the threshold stress intensity factor range is compared with the crack length

. The variation of the stress intensity factor range with crack depth for different bulk stress amplitudes at 260 MPa nominal contact pressure is depicted in Figure 6.39.

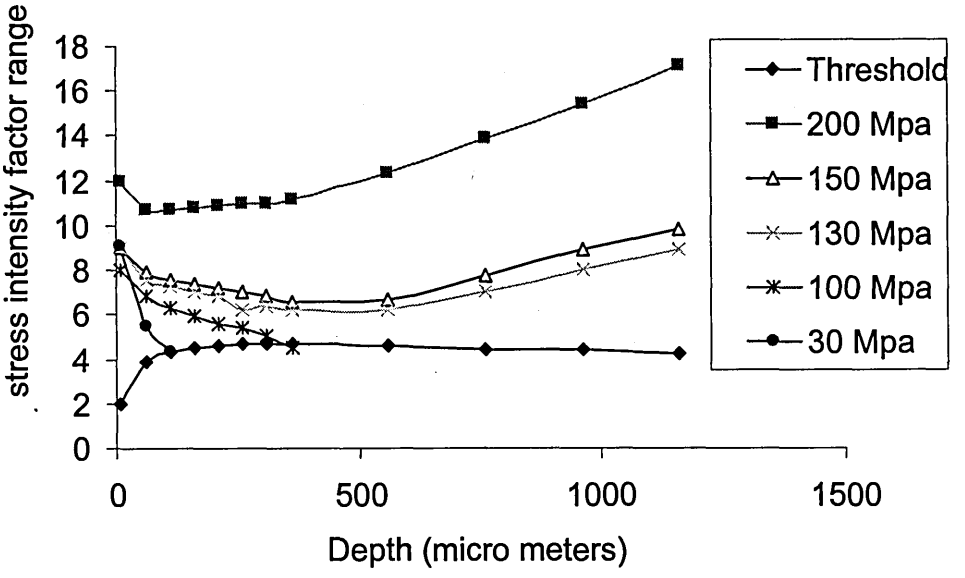

Figure 6.38 - Variation of stress intensity factor range with crack depth for various cyclic bulk stress: (260 MPa nominal contact pressure).

The condition applicable for a crack to propagate under cyclic loading is that the stress intensity factor range of the crack tip should exceed the threshold stress intensity factor range for the same position. The analysis of Figure 6.38 shows that the crack is predicted to arrest at early stages at low cyclic bulk stress amplitude. At 30 MPa cyclic bulk stress, the crack is predicted to arrest at 100 μm depth. At 100 MPa cyclic bulk stress, the crack is predicted to arrest around 270 μm. At cyclic bulk stresses above 130 MPa, the crack is not predicted to self arrest but is predicted to grow until specimen failure.

The variation of crack growth rate with the crack length at 260 MPa nominal contact pressure for various cyclic bulk stress amplitudes is shown in Figure 6.39.

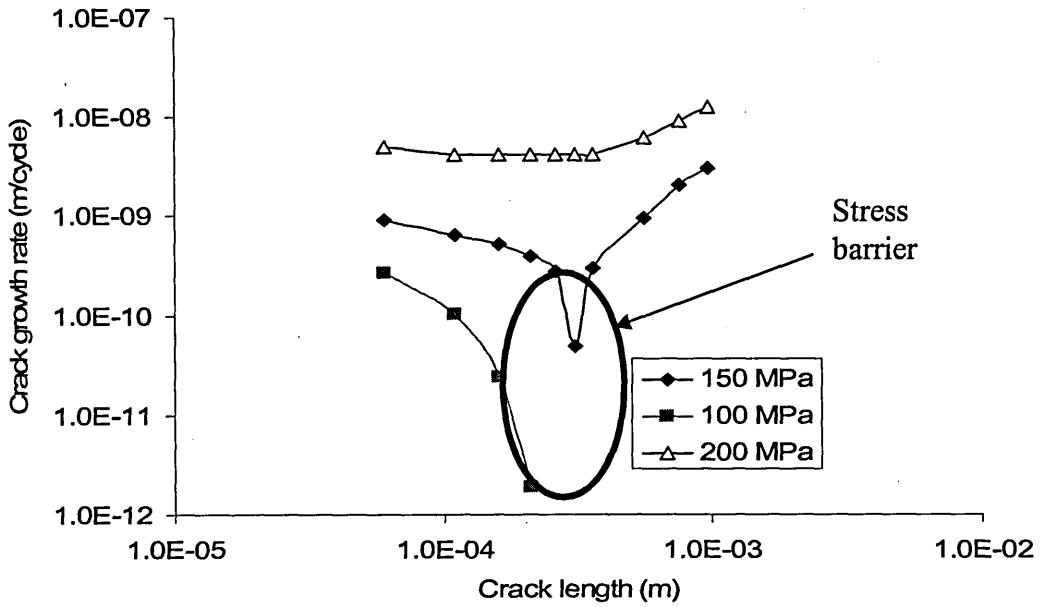

Figure 6.39 Crack growth rate at various cyclic bulk stress at 260 MPa nominal contact pressure.

From the Figure 6.39 three different crack growth behaviours can be identified. The one predicted at 200 MPa cyclic stress amplitude shows a very high crack growth rate. At 100 MPa the crack grows and arrest after propagating few hundred micrometres. At 150 MPa the crack grows and the crack growth rate retards at a particular depth and then again increases.

The analysis of Figure 6.39 suggests that the reason for the crack growth to retard is that the effective stress intensity factor range drops when the crack is around 300 μm long and attains almost the same range($\Delta K_{eff} - \Delta K_{effth} > 0$) as threshold for the corresponding crack length. If the combination of bulk stress and the contact pressure is sufficient to penetrate through this "barrier effect" the crack will grow until failure. If not the crack growth will arrest at a certain depth within the barrier. Such behaviour has been previously obtained experimentally by Kim and Lee [79] and Troshechenko et al [92]. Kim and Lee [79] reported that the crack growth rate is high at the beginning and decreases during the early stage of crack growth and then again increases during the later stages. They attribute crack arrest to the diminishing effect of contact stress field when moving away from the contact surface. This phenomenon is explained in terms of the effective stress intensity factor range and the threshold stress intensity factor range closer to the contact zone in Figure 6.39.

Effect of contact pressure with bulk stress

The variation of crack propagation rate at a 150 MPa constant cyclic bulk stress for different nominal contact pressures is shown in Figure 6.41. The variation of crack growth rate in this case is entirely different to that observed in Figure 6.40 for different cyclic bulk stresses.

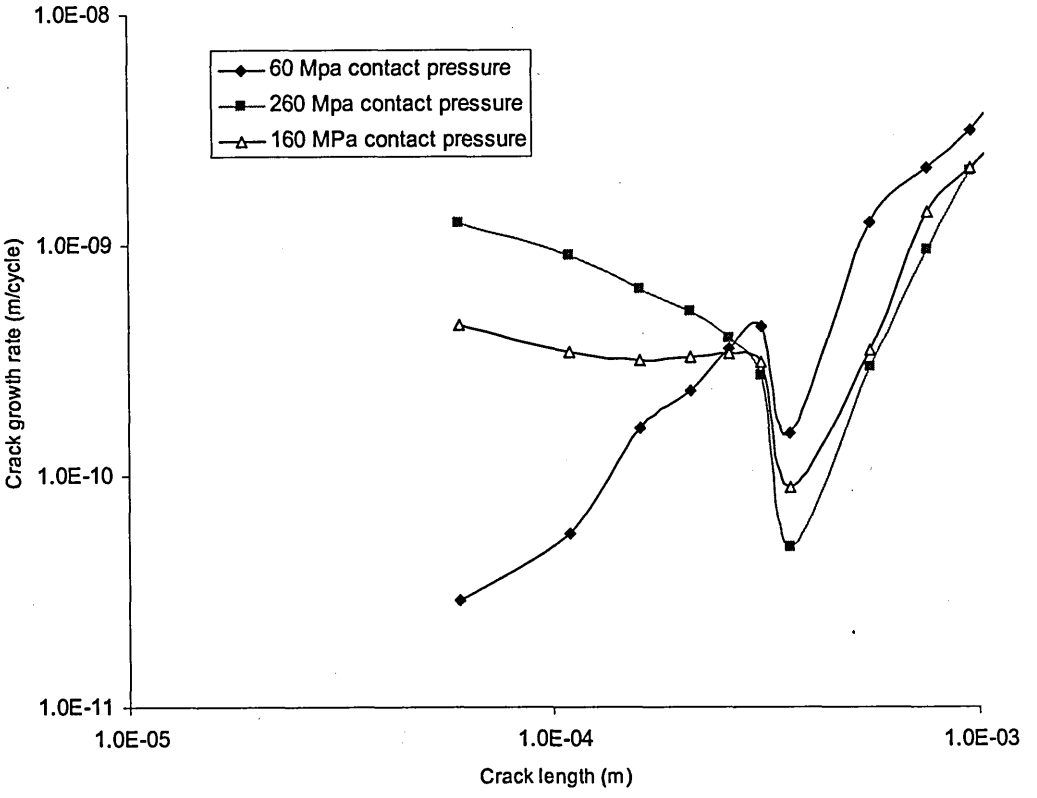

Figure 6.40 – Variation of crack growth rate with crack length for different nominal contact pressure; (150 MPa cyclic bulk stress).

Figure 6.41 depicts that after penetrating through the "barrier effect", the crack growth rate is almost the same for all contact pressure ranges. Before attaining the barrier range, the crack growth rate is greatly influenced by the contact pressure.

Reduction of fatigue strength of the actual wire

The objective of the cyclic test series (test C 101 – C 302 in experimental results) was to determine the failure mode and the reduction of the fatigue strength if a cyclic bulk load is applied in a perpendicular direction to the sliding direction. The stress state for this condition is shown in Figure 6.42

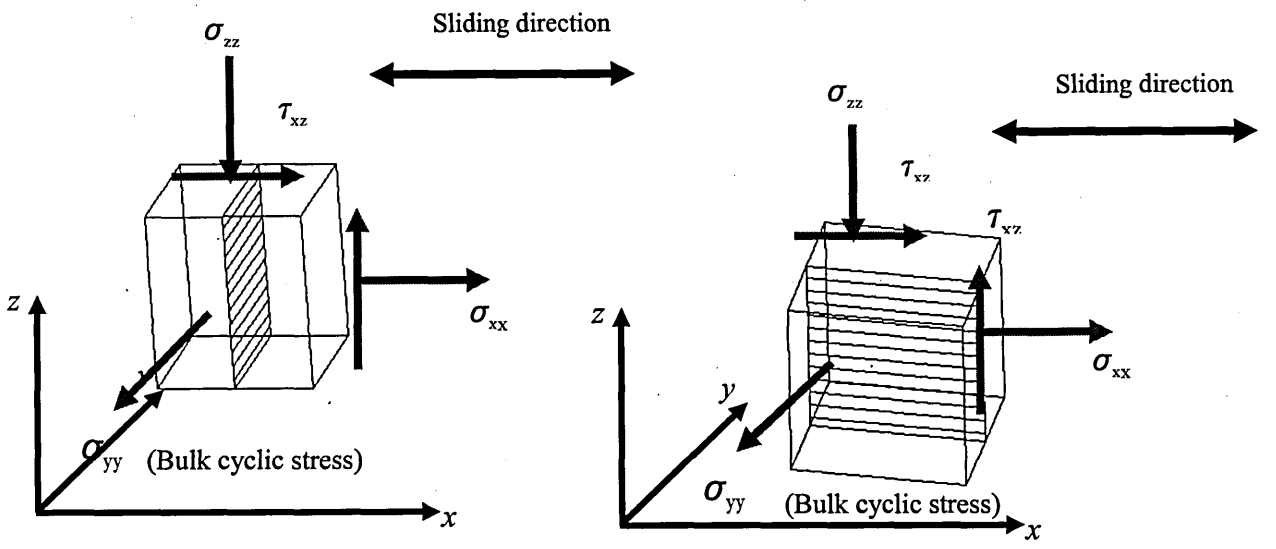

(a) Failure mode 1 (b) Failure mode 2

Figure 6. 41 – stress tensor when the cyclic bulk stress is in perpendicular direction to the sliding.

Here, the cyclic bulk stress is the σ_{yy} component while the stress components σ_{xx} and τ_{xz} are due to friction force. σ_{zz} is due to the normal contact load. In this scenario the fretting cracks are originated on plane shown in Figure 6.41 (a). In the previous analyses it was shown that if the cyclic bulk stress is σ_{xx}, the cyclic bulk stress can super impose on top of the fretting stress close to the surface and drive the fretting crack until material failure.

But in this situation, if the material is failing due to the cyclic bulk stress, the material should fail in the plane shown in Figure 6.41(b). Since the fretting originated crack is in a perpendicular plane to this, we can hypothesise two possible failure models.

Failure mode 1

The first hypothesis suggests that a crack is initiated due to fretting in the plane shown in Figure 6.41 (a) and upon applying a cyclic loading the crack changes by 90^0 through a smooth transition curve to the plane shown in Figure 6.41 (b). In this situation, a significant reduction of fatigue strength should be expected since the fretting originated crack is continuing through the failure.

Failure mode 2

The second hypothesis suggests that a crack is initiated due to fretting in the plane shown in Figure 6.41 (a). Application of a cyclic σ_{yy} bulk stress should not affect this crack and this crack in not changing or growing under the influence of the cyclic bulk stress. In order to cause failure due to the application of a cyclic σ_{yy} bulk stress in the direction, a new crack should initiate and grow under cyclic loading in the plane shown in Figure 6.41 (b). In this situation, a significant reduction of fatigue strength should not be expected since the fretting originated crack is not influenced by the cyclic bulk stress and the failure mode due to the cyclic bulk stress is not influenced by the fretting originated crack.

Prediction of crack growth under cyclic bulk stress

The numerical solution for a case of 260 MPa nominal contact pressure with a cyclic load of 90% of the fatigue strength (360 MPa) applied in a perpendicular direction, is shown in Figure 6.42..

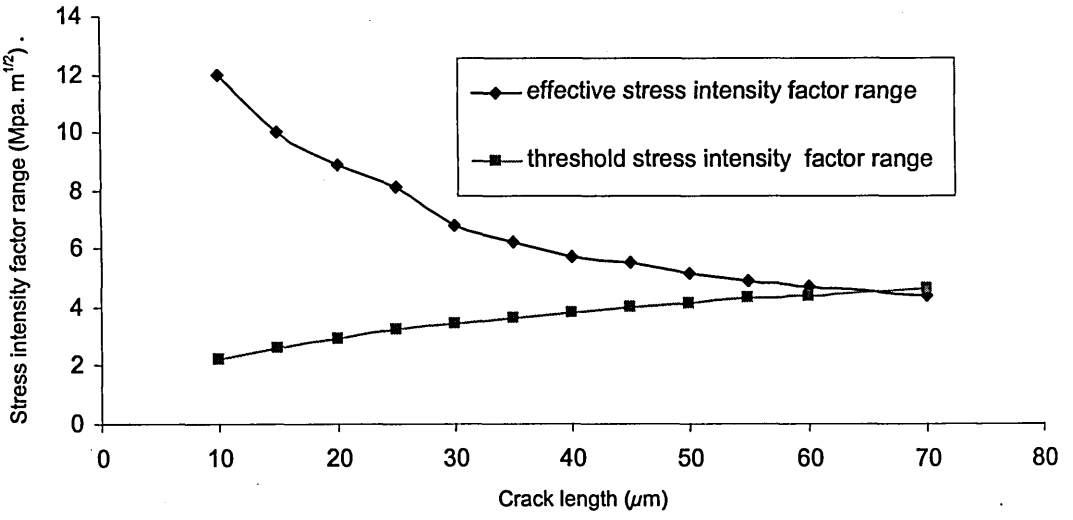

Figure 6. 42 Variation of stress intensity factor range with threshold: (260 MPa nominal contact pressure 360 MPa cyclic bulk stress in normal to sliding direction).

The Figure 6.42 shows the dominant influence of the contact stress field over the bulk cyclic stress in a normal direction to the sliding direction. The crack growth rate shown in Figure 6.42 is almost the same as that obtained for the case without cyclic bulk stress (Figure 6.31). In both cases the crack arrests at around 65 μm crack depth.

Furthermore, the same result occurs when a cyclic bulk stress of 110% of the fatigue strength (440 MPa) is applied in a normal direction to the sliding direction. The critical plane orientation and the effective stress intensity factor range for this situation is compared with the threshold value in Figure 6.43.

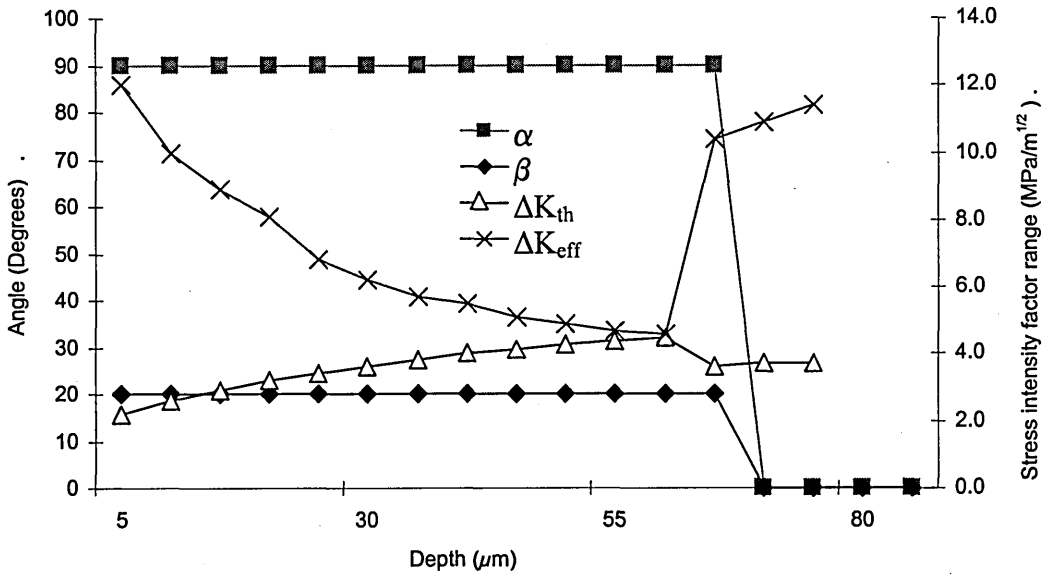

Figure 6. 43 - Variation of the critical plane orientation and stress intensity factor range with threshold (260 MPa nominal contact pressure 440 MPa cyclic bulk stress in normal to sliding direction).

The analysis of Figure 6.43 shows that the effective stress intensity factor range drops down almost to the threshold level at 65 μm depth but increases suddenly after penetrating the stress barrier effect. But this sudden increase of the effective stress intensity factor range is accompanied with the change of the critical plane orientation.

This analysis predicts that there is no smooth transition of the fretting originated crack when the cyclic stress is applied normal to the sliding direction and the reduction of the fatigue strength due to the fretting originated crack is less significant in this case. However the amplitude of the cyclic bulk stress should be very close or exceed the fatigue limit in order for the failure to occur due to fretting originated cracks.

Experimental results of cyclic loading of pre fretted specimens

The cyclic experimental series (tests C 1, test C 2 and test C 3) were carried out to investigate the influence of cyclic loading on pre-fretted specimens. The cyclic load was applied in the normal direction to the pad movement. The specimens were sectioned after the test in order to investigate the effect of cyclic loading on the fretting originated surface cracks. The results of the cyclic test programme were given in section 4.3 and the microscopic images are given in Figures 4.64 to Figure 4.69. The lengths of the surface cracks observed in the cyclic test series correspond to those observed for the corresponding test conditions where the bulk cyclic stress was monotonic (test P2, test P4 and test I 3).

Although all three specimens investigated (C1, C2 and C3) were subjected to high cyclic loading, none of the specimens failed by cyclic loading below the fatigue limit. The maximum load applied to the specimens was 90% of the fatigue limit. The experiments revealed that although the pre fretted specimens were subjected to fretting damage with a sliding direction normal to the direction of the cyclic bulk stress, the fretting originated cracks have insignificant effect on the fatigue life.

CHAPTER 7: CONCLUSIONS

1. The fretting damage behaviour of pressure armour wires of flexible pipes has been investigated. A novel experimental set-up has been designed and developed specifically to investigate the fretting damage process of pressure armour wires of flexible pipes.

2. It was possible to generate fretting damage in pressure armour samples under different combinations of contact pressure and slip amplitude and study phenomena such as slip condition, evolution of friction and wear rate.

3. Examination of the damaged regions showed fretting originated crack initiation at high contact pressures under mixed slip conditions. Significant surface damage due to wear results under gross slip conditions; no cracks were visible in the damage scars of tests in gross slip.

4. The maximum traction coefficient observed in the tests was 1.5 which is much higher than typical coefficients of friction for undamaged surfaces of metals (μ=0.3).

5. The results show that there is a significant influence of the normal pressure on the wear depth under gross slip. Less influence of normal pressure on the wear depth was observed under the mixed-slip condition.

6. A critical plane based crack analysis procedure was carried out. A severity parameter was proposed in order to ascertain whether the crack is growing in the mode I or mode II cracking. The analysis showed that the cracks initiate in mode II and approximately after 20 μm, the cracks deviate to the mode I direction and mode I dominates the crack propagation. The crack path determined by the numerical procedure correlates well with the experimental results.

7. A numerical analysis was carried out for the fretting fatigue condition where the cyclic bulk stress is superimposed with the friction force. The analysis correlates well with short crack growth behaviour (a reduction of the fatigue strength by 75% was predicted by the numerical procedure at the analysed condition).

   The analysis show that under certain bulk and contact loading conditions, fretting originated cracks grow until failure or arrest at a certain depth. The reason for a crack to arrest is that of the combined cyclic stress amplitude is not sufficient to penetrate through the stress barrier effect (Figure 6.40). A component subjected to fretting loading can fail if the combination of cyclic bulk stress and the contact stress amplitude is sufficient to exceed the stress barrier.

Note:

This behaviour was previously explained by Miller [3] with two possibilities. The argument for the first possibility was that " *Although the crack has been able to pass with comparative ease the first micro-structural barrier due to the surface applied biaxial stress system, it is not able to overcome a subsequent grain boundary ahead of the advancing crack*". The argument for the second possibility was formulated as "*The near surface biaxial stress system has rapidly decayed to a level which is insufficient to achieve the micro-structurally short crack driving force to equate to the ΔK value for the long propagation phase*". The current analysis is consistent with second explanation given by Miller [3].

This research investigation confirms that is a significant consideration in design and operation of the pressure armour wires of flexible pipes at high contact pressure when the bulk cyclic load superimposes with the friction force. However, the stress state of the pressure armour wire when in operation is such that the cyclic bulk stress is in a direction normal to the friction force. As predicted by the numerical procedure and verified by experimental investigations results , the surface cracks initiating in this condition are self arresting after propagating to a certain depth.

CHAPTER 8: FUTURE WORK

1. The numerical procedure was carried out in small layers along the crack path with moving into the material. The strength of this approach is the possibility to incorporate any changes of stress condition when moving into the material. Examples may be residual stresses induced by surface treatments such as shot peening. Further experimental and numerical analysis with this procedure is necessary to explore the accurate predictions for these conditions using this procedure.

2. Although a great deal of short crack growth behaviour has been explored and understood the crack growth behaviour near threshold level and very short region (below 100 μm) need understanding. Methodologies and experimental techniques are needed for in-situ observation of such short crack growth behaviour.

3. The numerical procedure was based on elastic stress and strain distributions and further improvements to the numerical procedure can be made by incorporating plasticity.

4. During the experiments it was revealed that the reduction of fatigue strength by application of a cyclic bulk stress in a normal direction to the fretting crack does not significantly reduce the fatigue strength. The possible damage locations are where fretting cracks occur or fretting wear. However further tests at higher cyclic loading are necessary to determine the exact location of the failure. The other possibility is that the specimen fails neither in the fretting crack sites nor the fretting wear, due to the fact that fretting loadings

might increase the surface hardness of the material similar to that in shot peening.

5. Although the proposed numerical procedure is capable of predicting the crack growth behaviour, further developments are needed to incorporate the wear process during fretting damage.

6. The numerical analysis, further confirmed by experimental results show that the contact geometry and corner radius has a greater influence on the fretting damage process. The pressure distribution shows that the peak pressure is less in the corner at higher corner radii. Furthermore, the crack path analysis shows that depending on the corner radius, the crack path is different and the crack arresting depth is also different. This means that there should be an ideal contact geometry that will minimise the fretting damage.

7. It is known that lubricants such as grease reduce wear and friction in tribological systems that are subjected to sliding. Detailed experiments are needed to explore the possibility of reducing the fretting damage process of pressure armour wires of flexible pipes.

REFERENCES

1 Waterhouse R.B. (1992) "Fretting" International Materials Reviews Vol 37 No 2, pp 77-98

2 Miller K.J.(2004) "Fretting Fatigue: A Review and Future Perspectives" Journal of Marine Design and Operations. pp 11-29

3 McColl, I. R, Ding, Leen S. B (2004) "Finite Element Simulation and Experimental Validation of Fretting Wear" Wear Vol 256, Issues 11-12 , June, pp 1114-1127

4 Ciavarellla M. and Demelio G (2001) "A Review of Analytical Aspects of Fretting fatigue, with Extension to Damage Parameters and Application to Dovetail Joints" International Journal of Solids and Structures 38 pp1791-1811.

5 Iyer K (2001) "Peak Contact Pressure, Cyclic Stress Amplitudes, Contact Semi-width and Slip Amplitude: Relative Effects in Fretting Fatigue Life". International Journal of Fatigue Vol. 23 pp193-206

6 Vincent L, Berthier Y, Duborg M C and Godet M (1992) "Mechanics and Materials in Fretting" Wear pp 135-148

7 Eden E M Rose W N and Cunningham F L (1911) "The Endurance of Metals" Proc.Instn Mech Engrs, 875

8 Tomlinson G A (1927) "The Rusting of Steel Surfaces in Contact", Proc Roy. Soc Lond. Ser. A 115 pp 472-483.

9 Waterhouse R.B. (1972) 'Fretting Corrosion'. 139 , Oxford, Pergamon publishers.

10 Hoeppner D. W. (1994) "Mechanisms of Fretting Fatigue" Fretting Fatigue, ESIS 18 (Edited by Waterhouse R B and Lindley TC), Mechanical Engineering Publications – London pp 3 -19.

11 Nix K J and Lindley T C (1985) "The Application of Fracture Mechanics to Fretting Fatigue" Fatigue and Fracture of Engineering Materials and Structures, Vol. 8(2) pp 143-160.

12 Ekberg A (2004) "Fretting Fatigue of Railway Axles – a Review of Predictive Methods and an Outline of a Finite Element Model" Proceedings of Institution of Mechanical Engineers Vol.218 pp 299-316.

13 Juuma T (2000) "Torsional Fretting Fatigue Strenth of a Shrink-Fitted Shaft with a Grooved Hub" Tribology International Vol 33 pp537-543.

14 Szolowinski M P, Farris T N. (1996) "Mechanics of Fretting Fatigue Crack Formation". Wear 198 93-107.

15 Min Liao, Shi G and Xiong Y (2001)"Analytical Methodology for Predicting Fatigue Life Distribution of Fuselage Splices" International Journal of Fatigue, Volume 23, , pp 177-185

16 Fatemi A and Socie D.A (1988) "Critical Plane Approach to Multiaxial Fatigue Damage Including out of Phase Loading" Fatigue Fract Eng Mat. Vol 11 pp 49-65.

17 Ding J, Leen S.B. McColl I.R. (2004) "The Effect of Slip Regime on Fretting Wear-Induced Stress Evolution" International Journal of Fatigue Vol 26 pp 521 – 531.

18 S J Harris, R B Waterhouse, I.R. McColl, (1993) "Fretting Damage in Locked Coil Steel Ropes" Wear Vol. 170 pp 63-70

19 O Wouter and B Patrick (2005) "Failure Analysis of the Deep Groove Ball Bearings of an Electric Motor " Engineering Failure Analysis Volume 12, Issue 5, pp 772-783

20 Miyoshi K, Bradley A.L, Susan L. D (2003) "Fretting Wear of Ti-48Al-2Cr-2Nb" Tribology International Volume 36, Issue 2 pp 145-153

21 Fernando U.S, Farahi G.H, Brown M. W (1994) "Fretting Fatigue Crack Growth Behaviour of BS L65 4 percent Copper Aluminium Alloy under Constant Normal Load" fretting fatigue ESIS 18 (Edited by R.B. Waterhouse and T C Lindley) Mechanical Engineering Publications, London pp 183-195.

22 Rajasekaran R, Nowell D (2006) "Fretting Fatigue in Dovetail Blade Roots: Experiments and Analysis" Tribology International 39 pp1277-1285

23 Ruiz C, Boddington P H B, Chen K C, (1984) "An Investigation of Fatigue and Fretting in a Dovetail Joint" Exp Mech 24 pp 208-217

24 Baker R.F., Oliver A.V. (1997) "Direct Observation of Fretting Wear of Steel" Journal of Wear 203-204 pp 425-433.

25 Varenberg M, Etsion I, Halperin G (2004) "Slip Index: Unified Approach to Fretting" Tribology letters Vol.17 No3.

26 Dobromirski J M, (1992) "Variables of Fretting Process: Are There 50 of Them?" (M. Helmi Attia and R.B. Waterhouse, Editors,) *Standardization of fretting fatigue tests and equipment, ASTM STP 1159*, American Society for Testing and Materials, Philadelphia, pp. 60–66.

27 Jin O and Mall S, (2002) "Effects of Independent Pad Displacement of Fretting Fatigue Behaviour of Ti-6Al-4V" Wear 253 pp 585 -596

28 Smith K. N, Watson P, Topper T.H, (1970) " A Stress Strain Function for the Fatigue of Metals" J Mater, Vol 15 pp768-778

29 Chen G. X and Zhou Z.R. ((2001) "Study on Transition between Fretting and Reciprocating Sliding Wear" Wear pp 665-672.

30 Fouvry S, Kapsa P, Vincent L, (1996) "Quantification of Aretting Damage". Wear, pp 186-205.

31 Vingsbo O and Soderberg S, (1988) "On Fretting Maps" Wear 126 pp 131-147.

32 Ramesh R and Gnanamoorthy R (2006) "Development of a Fretting Wear Test rig and Preliminary Studies for Understanding the Fretting Wear Properties of Steel". Materials and Design Vol.27 pp 141-146.

33 Nakazawa K, Maruyama N, Hanawa T (2003) "Effect of Contact Pressure on Fretting Fatigue of Austenitic Stainless Steel" Tribology International 36 pp79-85.

34 Naidu N K R and Raman S G S (2005) "Effect of Contact Pressure on Fretting Fatigue Behaviour of Al- Mg-Si alloy AA6061" International Journal of Fatigue 27 pp 283-291.

35 Iyre K and Mall S, (2001) "Analysis of Contact Pressure and Stress Amplitude Effects on Fretting Fatigue Life". Journal of Engineering Materials and Technology 123 pp 85-93

36 Muotoh Y and Xu J (2003) "Fracture Mechanics Approach to Fretting Fatigue and Problems to be Solved". Tribology International Vol 36 pp 99-107

37 Iwabuchi A, Kato K, Kayaba T (1986) "Fretting Properties of SUS304 Stainless Steel in a Vacuum Environment". Wear, Vol 110, pp 205 – 216.

38 Ramalho A, Merstallinger A, Cavaleiro A (2006) "Fretting Behaviour of W-Si Soated Steels in Vacuum Environments", Wear, Vol 261 pp 79 – 85.

39 Poon C and Hoeppner D W (1979) "The Effect of Environment on the Mechanism of Fretting Fatigue", Wear 52 pp 175 – 191.

40 Iwabuchi A (1985) "Fretting wear of Inconel 625 at High Temperature and in High Vacuum" Wear Vol 106 pp 163 - 175

41 McColl I R, Waterhouse R.B., Harris S.J. Tsujikawa M (1995). "Lubricated Fretting Wear of a High Strength Eutectoid Steel Rope Wire" Wear 185, pp 203-212.

42 Shima M, Suetake H, McColl I R, Waterhouse R B, Takeuchi M (1997) "On the Behaviour of an Oil Lubricated Fretting Contact" Wear 210 pp 304-310

43 Fouvry S, Nowell D, Kubiak K and Hills D A(2007) "Prediction of Fretting Crack Propagation Based on a Short Crack Methodology" Journal of Engineering Fracture Mechanics (electronic copy)

44 Zhou Z.R and Vincent L (1999) "Lubrication in Fretting – a Review" Wear 225-229 962-976.

45 Johnson K.L (1985) "Contact Mechanics" Cambridge University Press

46 Ciavarella M, Hills D. A., Monno G, (1998) "The Influence of Rounded Edges on Indentation by a Flat Punch" Proc. Institution of Mechanical Engineers Vol.212 C, pp. 319-328.

47 Nishioka K and Hirakawa K, (1969) "Fundamental Investigation of Fretting Fatigue: part 5 The Effect of Relative Slip" Bulletin of Japan Society of Mechanical Engineers, Vol. 12 pp 692-697.

48 Araaujo J A, Nowell D , Vivacqua R C,(2004) "The Use of Multiaxial Fatigue Models to Predict Fretting Fatigue Life of Components Subjected to Different Contact Stress Fields" Fatigue Fract. Eng Mater Struct , pp. 967–978

49 Dang Van K, Griveau B and Message (1982), "On a New Multiaxial Fatigue Limit Criterion: Theory and Application" (Biaxial and Mulitiaxial Fatigue) edited by Brown M W and Miller K J. EGF Publication 3 pp479-496.

50 Dang Van K and M H Maitournam (2000) "On a New Methodology for Quantitative Modelling of Fretting Fatigue" Current Technology and Practices, ASTM STP1367.

51 Giannakopulsos A E , Lindley T C , Suresh S (1998) "Aspects of Equivalence Between Contact Mechanics and Fracture Mechanics: Theoretical Connections and a Life Prediction Methodology for Fretting Fatigue" Acta Mater. Vol 46, No 9 pp2955-2968

52 Faanes, S and Fernando U.S.(1994) "Life Predictions in Fretting Fatigue Using Fracture Mechanics" Fretting Fatigue, ESIS 18 (Edited by Waterhouse R B and Lindley TC) Mechanical Engineering Publications – London pp149-159.

53 Faanes, S and Harkegard G (1994) "Simplified Stress Intensity Factors in Fretting Fatigue" Fretting Fatigue, ESIS 18 (Edited by Waterhouse R B and Lindley TC) Mechanical Engineering Publications – London pp 73-81

54 Rooke D.P(1994) "The Development of Stress Intensity Factors", Fretting Fatigue, ESIS 18 (Edited by Waterhouse R B and Lindley TC) Mechanical Engineering Publications – London pp 23-58.

55 Conner B.P., Lindley T C, Nicholas T, Suresh S, (2004) "Application of a Fracture Mechanics Based Life Prediction Method for Contact Fatigue" International Journal of Fatigue Vol. 26 pp 511-520.

56 Suresh S. (1998) "Fatigue of Materials" Second Edition, Cambridge University Press U.K.

57 Fouvry S, Liskiewicz T, Kapsa P.H, Hannel S, Sauger E (2003) "An Energy Description of Wear Mechanisms and its Applications to Oscillating Sliding Contact" Wear 255 pp 287-298.

58 Szolowinski M P, Farris T N (1998) "Observation, Analysis and Prediction of Fretting Fatigue in 2024-T351 Aluminium Alloy" Wear 221 pp 24-36.

59 Valleano C, Dominguez J, Navarro A, (2003) "On the Estimation of Fatigue under Fretting Conditions using Notch Methodologies" Fatigue fract Engng Mater Struct 26, PP 469-478

60 T C Lindley and K J Nix (1992) "Fretting Fatigue in Power Generation Industry". (Standardisation of Fretting Fatigue Tests Methods and Equipments. Edited by H Attia and R B Waterhouse) ASTM STP 1159, pp 153-169.

61 Araujo J A and Nowell D (2000) " Perdition of Fretting Fatigue Life using Averaged Multiaxial Initiation Parameters" Modern Practice in Stress and Vibration Analysis University of Nottingham UK.

62 Hills D.A, Nowell D, (1994) "A Critical Analysis of Fretting Fatigue Experiments", Fretting Fatigue ESIS 18 (Edited by R.B. Waterhouse and T C Lindley) Mechanical Engineering Publications, London pp 171-182.

63 Hills D A and Nowell D (1994) "Mechanics of Fretting Fatigue" Kluwer Academic Publisher.

64 Fridrici V, Fouvry S, Kapsa P, Perruchaut P (2005) "Prediction of Cracking in Ti-6Al-4V alloy Under Fretting Wear: Use of the SWT Criterion" Wear 259 pp 300-308

65 Lykins C D, Mall S, Jain V (2000) "An Evaluation of Parameters for Predicting Fretting Fatigue Crack Initiation". International Journal of Fatigue, Vol. 22 pp 703-716.

66 Namjoshi S A, Mall S, Jain V K, Jin O (2002) "Effects of Process Variables on Fretting Fatigue Crack Initiation in TI-6Al-4V" Journal of Strain Analysis Vol 37 pp535-547.

67 Proudhon H, Foury S, Fuffiere J Y (2005) "A Fretting Crack Initiation Prediction Taking into Account the Surface Roughness and the Crack Nucleation Process" Volume. Int J of Fatigue ; 27(5): pp569-579

68 Proudhon H, Fouvry S, Yantio G R (2005) "Determination and Prediction of the Fretting Crack Initiation: Introduction of the (P,Q,N) Representation and Definition of a Variable Process" Volume. International Journal of Fatigue Vol.28 pp 1769-1779.

69 S. Munoz, H Proudhon, J Dominguez and S Fouvry (2006) "Prediction of the Crack Extension Under Fretting Wear Loading Conditions" International Journal of Fatigue Vol 28 pp 1769-1779.

70 Sum W S, Williams E J, Leen S B (2005) "Finite Element, Critical-Plane, Fatigue Life Prediction on Simple and Complex Contact Configurations" International Journal of Fatigue 27 pp 403-416

71 Fouvry S, Duó P, Perruchaut P.H, (2004) "A Quantitative Approach of Ti–6Al–4V Fretting Damage: Friction, Wear and Crack Nucleation", Wear Volume 257, pp 916-929

72 Ratsimba C.H.H.,. McColl I.R, Williams E.J, Leen S.B, and. Soh H.P (December 2004) "Measurement, Analysis and Prediction of Fretting Wear Damage in a Representative Aeroengine Spline Coupling" Wear Volume 257, Issue 11 , pp 1193-1206

73 Madge J J, Leen S B, Shipway P H, (2007) "The Critical Role of Fretting Wear in the Analysis of Fretting Fatigue" Wear Vol 263 pp1 - 10

74 Ding J, Sum W S, Sbesan R, Leen S B, McColl, Williams E J.(2006) " Fretting Fatigue Predictions in a Complex Coupling" International Journal of Fatigue Vol 29 pp 1229-1244..

75 Vidner J, Leidich E, Enhanced Ruiz (2007) "Criterion for the Evaluation of Crack Initiation in Contact Subjected to Fretting Fatigue" International Journal of Fatigue (Article in Press)

76 Lindley T.C. (1997) "Fretting Fatigue in Engineering Alloys" Int Journal of Fatigue Vol 19 1 pp 39-41

77 Lindley T.C. and Nix K.J (1994) "An Appraisal of the Factors which Influence the Initiation of Cracking by Fretting Fatigue in Power Plant" Fretting Fatigue ESIS 18 (Edited by R.B. Waterhouse and T C Lindley) Mechanical Engineering Publications, London pp 239 – 256.

78 Golden P.J. Grandt jr. A F(2004) "Fracture Mechanics Based Fretting Fatigue Life Predictions" Engineering Fracture Mechanics 71 pp 2229-2243

79 S. Faanes (1995)"Inclined Cracks in Fretting Fatigue" Engineering Fracture Mechanics Vol. 52, (1) PP 71-82

80 Mutoh Y and Xu J (2003) "Fracture Mechanics Approach to Fretting Fatigue and Problems to be Solved" Tribology International Vol 36 pp 99-107.

81 Antoniou R A and Radtake T C (1997) " Mechanisms of Fretting Fatigue of Titanium Alloys" Materials Science and Engineering pp 229 – 240.

82 Kim H K and Lee S B "Crack Initiation and Growth Behaviour of Al 2024- T4 under Fretting Fatigue" (1997), Int J Fracture Vol 19, No 3 pp 243-251.

83 Green R.J, (2003) "A Study of Fretting Fatigue Incorporating Sharp Corner Contact Geometry" Ph.D. Thesis, Sheffield Hallam University , UK.

84 Johnson K.L (1995) "Contact Mechanics and the Wear of Metals" Wear 190 pp162-170

85 Socie D F and Marquis G B, (2000) "Multiaxial Fatigue" SAE International.

86 Bnnantine J A, Comer J J, Hardrock J L (1990) "Fundamentals of Metal Fatigue Analysis" Prentice Hall.

87 Hern E J. (1997) "Mechanics of Materials 2, An Introduction to the Mechanics of Elastic and Plastic Deformation of Solids and Structural Materials". Third Edition Butterworth-Heinemann Publishers.

88 Walker E K (1970) "Effects of Environment and Complex Loading History on Fatigue Life" ASTM STP 462, Philadelphia.

89 Masounave J and Bailon J P (1975) "Dependance of the Threshold Stress Intensity Factor on the Cyclic Stress Ratio in Fatigue of Ferritic –Pearlitic Steels" Scripta Metallurgica Vol 9 pp 723-730

90 McEvily A.J and Yang Z, (1992) "An Analysis of the Rate of Growth of Short Fatigue Cracks", Short Fatigue Cracks ESIS 13 Mechanical Engineering Publications, London pp 439-448.

91 Nisitani H and Goto M (1992) "A Small Crack Growth Law and its Application to the Evaluation of Fatigue Life", The Behaviour of Short Fatigue Cracks EGF, Mechanical Engineering Publications, London, pp 461-478.

92 Dugdale D S (1960) "Yielding of Steel Sheets Containing Slits" Journal of Mech. Phys. Solids, pp8-100.

93 EL Haddad M H, Smith K N ,Topper T. H (1979)"Fatigue Crack Propagation of Short Cracks" Journal of eng. mat. Tech pp101 42

94 Fernando U.S, Brown M W, Miller K J (2007) "Linear Elastic Fracture Mechanics Interpretation of Crack Growth Behaviour in Fretting Fatigue " a Private Communication.

95 Troshchenko V T, Tsybanev G V , Khotsyanovsky A O (1994) "Two-Parameter Model of Fretting Fatigue Crack Growth" Fatigue Fract. Eng Mater. Struct. Vol.17 pp15-23